



ScuDo

Scuola di Dottorato ~ Doctoral School
WHAT YOU ARE, TAKES YOU FAR



Doctoral Dissertation

Doctoral Program in Electrical, Electronics and Communication Engineering (31th
Cycle)

Development of Monolithic Glass Suspended Microchannel Resonators designed for bead-based bioassays

Roberta Calmo

* * * * *

Supervisor

Prof. Carlo Ricciardi

Doctoral Examination Committee:

Prof. Thomas Burg, Referee, Max Plank Institute for Biophysical Chemistry (Göttingen, Germany)

Prof. Massimo De Vittorio, Referee, Università del Salento (Lecce, Italy)

Prof. Paolo Olivero, Università di Torino (Torino, Italy)

Prof. Sergio Ferrero, Politecnico di Torino (Torino, Italy)

Prof. Fabrizio Giorgis, Politecnico di Torino (Torino, Italy)

Politecnico di Torino

May 12, 2019

This thesis is licensed under a Creative Commons License, Attribution – Noncommercial – NoDerivative Works 4.0 International: see www.creativecommons.org. The text may be reproduced for non-commercial purposes, provided that credit is given to the original author.

I hereby declare that, the contents and organisation of this dissertation constitute my own original work and does not compromise in any way the rights of third parties, including those relating to the security of personal data.

.....

Roberta Calmo
Turin, May 12, 2019

Summary

The here proposed work is aimed to introduce new functionalities on a microgravimetric sensor based on suspended microchannel resonator (SMR). In particular, a novel label-free sensing approach is envisioned, conceiving a high-capturing substrate (porous beads), used as mass-carrier, with 3D laser machined SMR devices. In order to do that, a deep knowledge of their peculiar functionalities as distinctive systems is required.

The SMRs had shown great potential in the biosensing field. In particular, the design proposed by *Manalis et. al* in 2007 has been extensively applied to the study of eukaryotic cells, ranging from the monitoring of single cell growth to the determination of the therapeutic susceptibility. The main drawback of the actual SMR platforms is represented by the fabrication process, which generally requires expensive, time consuming and complex processing techniques. Moreover, only few examples of label-free biomolecular assays based on these sensors have been presented in the literature. These approaches generally exploit the selective functionalization of the inner walls of the suspended channel, in order to promote the immobilization of specific biomolecular capturing probes (i.e. ssDNA, antibody or other macromolecules). Unfortunately, this method shows some limitations mainly due to the inhomogeneity of the functionalization of the channel walls and the control of the fluid dynamic aspects to promote the binding kinetics between probe and target

molecules. Furthermore, this approach suffers of a limited reusability, due to the difficulty to chemically clean the microsystem.

This work shows for the first time an innovative, rapid and monolithic fabrication process to get totally transparent SMRs. The resonators have been developed entirely in glass with a 3D microfabrication approach that simplifies and speeds up the fabrication process. Starting from a microscope glass slide, a femtosecond laser micromachining technique directly defines, within a single step, both the suspended bridge resonator and the embedded microfluidic channel that are subsequently released by a KOH etching. The mechanical characterization of these resonating bridges showed that the mass resolution and sensitivity in air environment are comparable to those reported in the state-of-art SMRs, while they perform better than commercial microcapillary glass resonators.

In order to develop a label free bioassay, a new integrated approach was investigated: the use of a mesoporous bead as high binding capturing vector was proposed. The idea comes from the possibility to exploit the same characterization concept used for the study of the single cell, flushing the beads inside the channel and monitoring the mass variation due to the interaction between probe and target molecules. Using this approach, the limitation due to the functionalization inside the channel is avoided, thanks to the possibility to directly add specific functionalities during the beads synthesis. At the same time, the optimization of the detection assay can be preliminary conducted using well-known biomolecular strategies. In this perspective, the thesis work was mainly devoted to the development of a bioassay compatible with the integration into the SMR platform and in particular it was mainly focused on the optimization of a DNA-DNA hybridization assay using the mesoporous silica beads as capturing substrate.

The work started with the optimization of the strategy of synthesis to obtain micron-size porous beads compatible with the inner channel dimension. A co-condensation method, in acidic environment, was preferred to other synthesis strategies. In fact, using this approach it has been possible to obtain, with high efficiency, mesoporous

beads with different chemical functionalities already embedded into the porous framework. After a careful physical–chemical characterization, the MPTMS (3–mercaptopropyltrimethoxysilane) modified beads were chosen as preferential material for the immobilization of the ssDNA probe. The non–specific signals, deriving from undesired interactions between the molecules involved in the assay, represent a crucial aspect for the future integration of the assay into the SMR platform. In fact, this phenomenon will affect the evaluation of the beads mass variation generating false positive results. For this reason, the optimization of the bioassay was carried out searching the best configuration for the non–specific signal suppression. The optimization of the molecular recognition allows to obtain a relatively high limit of detection (LOD), which ranges between 11 and 3 pM, thus being comparable with well–know biomolecular tests such as the enzyme linked immunosorbent assay (ELISA). The dynamic range and the LOD relative to the bead–based assay could be in principle further improved with the integration of this protocol with the quantification of the target amount directly with the SMR platform, using a label–free approach.

Acknowledgment

I would like to thank my PhD advisor, Professor Carlo Ricciardi, for the possibility to follow this interesting academic experience.

I am also grateful to Dr. Alessandro Chiadò and Dr. Stefano Stassi for their scientific advice, for the insightful discussion and suggestion that have been fundamental for my work. Dr. Alessandro Chiadò was my primary resource for getting my science questions discussed with enthusiasm and great criticism that helped me to look out the problems from a different perspective.

I want to thank the other members of my research group and the PhD fellows (Cecilia Giovinazzo, Davide Scaiola, Niccolò Paccotti, Chiara Novara, Gianluca Palmara, Erik Piatti, Gianluca Milano, Federico Raffone, Filippo Savazzi, Daniele Conti), which were fundamental to turn a bad scientific day into a nice and funny shared dinner or beer! I want to thank in a special way Cecilia, Davide, Jonathan and Gloria for the help in my PhD work, for the discussion about the results of our research and for the perfect double layer Cr/Au deposition made by Cecilia!

Finally, I want to thank my family (Mummy, Daddy and Sister) and the closet friend (Lisa, Andrea, Beatrice, Tommaso, Diana) that are the special peoples of my life. They literally encouraged me each time that I was in doubt!

Special thanks to Alessandro that is my true and greatest supporter. He has unconditionally supported me during my good and bad times, both in the lab and at home!

The work was partially supported by Fondazione Cassa di Risparmio di Cuneo through FRUITSENSOR grant, Regione Piemonte through European Funds for Regional Development (FOOD DIGITAL MONITORING project).

I thank FEMTOprint® and Andrea Lovera for the fabrication support of the SMR platforms.

Contents

1. Introduction.....	1
2. Fundamentals of Micromechanical resonator	7
2.1. Introduction	7
2.2. Resonance Frequency	8
2.2.1. Single clamped beam	8
2.2.2. Double clamped beam	10
2.3. Quality Factor	11
2.4. Frequency response to mass.....	13
2.5. Frequency noise	16
2.5.1. Allan’s deviation	16
3. SMR Design and Fabrication	19
3.1. Introduction	19
3.2. Femtosecond laser micromachining: physical mechanism.....	20
3.3. Femtosecond writing principles	22
3.4. Laser writing Set-up	24
3.5. SMRs design.....	25
3.5.1. Double clamped beam	25
3.6. SMRs fabrication procedures	27
3.7. SMRs morphological analysis.....	31

3.8.	SMRs packaging	33
3.8.1.	PDMS bonding process	35
4.	Mechanical characterization and validation.....	38
4.1.	Introduction	38
4.2.	Measurement Set-up.....	39
4.2.1.	Laser Doppler Vibrometer.....	39
4.2.2.	Lock-in and PLL	40
4.3.	Frequency characterization	41
4.4.	Quality factor characterization.....	43
4.5.	Responsivity	48
4.6.	Allan deviation analysis.....	50
4.7.	Liquid density measurements.....	52
4.8.	Measurement of Bacterial cells.....	54
4.8.1.	Methods: bacterial culture	54
4.8.2.	Microgravimetric analysis.....	55
5.	Beads assay	58
5.1.	Introduction	58
5.2.	Mesoporous silica materials	60
5.3.	Mechanism of mesostructured formation	61
5.4.	The synthesis of mesoporous beads: affecting variables.....	65
5.4.1.	pH of reaction	65
5.4.2.	Surfactants and Swelling agents	66
5.4.3.	Alkoxo roup/H ₂ O ratio (R_w).....	68
5.4.4.	Electrolytes	68
5.4.5.	Reaction temperature	68
5.5.	Template removal.....	69
5.6.	Functionalization.....	70

5.7.	Methods.....	70
5.7.1.	Microbeads synthesis	70
5.7.2.	Measurement protocols.....	72
5.8.	Microporous silica beads characterization.....	76
5.8.1.	Specific surface area and pore size.....	77
5.8.2.	Morphological analysis.....	83
5.8.3.	Functional group analysis	84
5.9.	Optimization of the DNA hybridization assay	91
5.9.1.	Evaluation of the pores availability.....	92
5.9.2.	Optimization of the surface passivation	95
5.9.3.	Evaluation of the non-specific signal influence on probe immobilization and target detection	99
5.9.4.	Optimization of the DNA target detection	101
6.	Conclusion	108
7.	References	112
8.	Appendix A: Single Clamped beam design	127
9.	Appendix B: SMRs characterization.....	131
10.	Appendix C: Electrodes integration.....	137
11.	Appendix D: Reagents	144

List of Tables

Table 4.1 Q factor variation as function of the gap configuration, tested for two beam classes characterized by different width: 50 μm and 75 μm	45
Table 4.2 Dissipation energy contributions to the final quality factor.	48
Table 4.3 Allan's Deviation and mass resolution values. Allan's deviation values for different SMRs design obtained from the 20X-based fabrication method (first section of the table) and from the 50X-based fabrication method (second section of the table). The mass resolution values (obtained from the mass and the Allan's deviation of each SMR) are also listed in the table.	50
Table 5.1 Resume of the reagents ratio used for the synthesis of the bare and modified mesoporous silica beads; for the co-condensation process the silica precursor/organosilane ratio are specified.	80
Table 5.2 Resume of the BET analysis. In the table are reported the BET surface area, BJH adsorption/desorption pore area and DFT pore size for the bare and modified mesoporous silica beads.	82
Table 5.3 Evaluation of the silane molecules embedded as function of the specific area of bare and modified mesoporous silica beads.	88
Table 5.4 Comparison of the SH incorporated during the co-condensation synthesis: comparison of TGA and FITC test based quantification.....	95
Table B.1 Resonance Frequency (air and vacuum) and Responsivity (air), calculated considering the mass of the empty resonator. The table is divided horizontally in two sections: the upper one is related to the SMR fabricated with the	

20X objective and the lower part is referred to the SMR fabricated with the 50X objective. The samples that show the best responsivity are highlighted in red.....132

Table B.2 Comparison of the Q factors calculated using the Lorentz fit or the Exponential decay fit.135

List of Figures

Figure 1.1 Schematic representation of a biosensor working mechanism. The most important elements that compose a biosensor are put in evidence, like the bioreceptor binding site, the transducer module and the output signal analyzer.....	2
Figure 1.2 Suspended microchannel resonator a) SEM images of a SMR characterized by the cantilever shape, the dashed line highlights the channel path (from Manalis et al. 2006); b) particular of the embedded microfluidic channel; d) correlation between the particles position and the amplitude of the resonance peak (from Manalis et al. 2007).	5
Figure 2.1 Graphical representation of a single clamped beam (cantilever).	8
Figure 2.2 Schematics representation of the first four flexural or bending mode of a cantilever. Picture from the “Fundamentals of nanomechanical resonator, Schimit et al. Springer 2016).....	9
Figure 2.3 Graphical representation of a doubly clamped beam.....	10
Figure 2.4 Schematics representation of the first four flexural or bending mode of a doubly clamped beam. Picture from the “Fundamental of nanomechanical resonator, Schimit et al. Springer 2016).....	11
Figure 2.5 Q factor and damping effect, schematic representation of the bandwidth variation (evaluated at -3 dB) due to the damping effect.	12
Figure 2.6 Ring-down response to an initial excitation, the exponential decrement behaviour when the driving signal is switched off is reported.....	12

Figure 2.7 One-dimensional oscillator schematically represented taking into account the damped-element model. Picture from the “Fundamental of nanomechanical resonator, Schimit et al. Springer 2016).	14
Figure 2.8 Time scale of the measurement interval. Picture from the “Time domain oscillator stability measurement, Allan variance”, Application Note Rohde&Schwarz 2015.	17
Figure 2.9 Allan deviation log-log plot, the curve represent the typical behaviour of the Allan deviation as function of the sample averaging time. Picture from the “Fundamental of nanomechanical resonator, Schimit et al. Springer 2016).	18
Figure 3.1 Time scale of the femtosecond laser pulse/transparent material interaction. The green bars show the typical time scale of different fundamental processes involved during the irradiation. Picture from “Femtosecond laser micromachining in transparent materials”, Gattass et al. Nature Photonics, Vol 2 April 2018.	21
Figure 3.2 Schematic diagram of different laser matter interaction, a) continuous wavelength laser unfocused resulting in the transmission of the sub-band gap light, b) long pulsed laser focused in the solid volume produce an uncontrolled modification of the matter, c) ultrashort pulsed laser tightly focused enable the controlled modification of the volume exposed to the laser light.	22
Figure 3.3 Femtosecond laser direct writing system, a) schematic configuration of a general writing system (from He et al. 2014 doi:10.3390/s141019402), b) images of the Femtoprint® writing head.	24
Figure 3.4 Schematic illustration of the glass SMRs design. a) Clamped clamped beam and embedded channel chip, b)-c) detail of the suspended bridge with a big and small buried microchannel respectively.	26
Figure 3.5 Schematic illustration of the femtosecond laser patterning, the writing process is highlight in red and the suspended microchannel resonator release after KOH etching is highlight in blue.	27

Figure 3.6 SEM images of the microchannel inlet, which show different channel shape and dimension. a) A totally spherical channel was obtained working with a 50X objective (medium-high NA), in contrast b) an elliptical channel was obtained working with a 20X objective (low NA), varying the energy/pulse the minimum channel diameter was modify.....29

Figure 3.7 SEM images of the possible fused silica damage that can occur during the laser writing process, a)-b) fused silica re-deposition, c) modification of the channel surrounding and d) high roughness of the inner walls surfaces.....30

Figure 3.8 SEM images of channel inlet obtained with a 20X objective, a)-b)-c) represent the three different channel width, which were designed to evaluate the impact of the channel volume on the mechanical properties of the SMR.31

Figure 3.9 SEM images of the gap under the SMRs. Four different gap configuration has been (20-100-200 μm and free gap) designed to evaluate the viscous damping impact. In particular, 20 – 100 – 200 μm and free gap has been fabricated (a-b-c-d respectively).....31

Figure 3.10 Morphological analysis of the SMRs, a-c) are the interferometric response for an intact and damaged surface, respectively, b-d) optical images of the same samples were the presence of the damage is clearly not appreciable.....32

Figure 3.11 SEM images of the SMRs, a) from the picture is clearly visible the presence of some superficial damage due to the wrong Z-alignment of the femtosecond laser during the writing process, b) detail of the SMR and relative damage along the central part of the beam, c) detail of the channel inlet where a wrong Z-alignment of the laser beam is clearly visible.33

Figure 3.12 PDMS microfluidic interface, a-b) silicon mold design and the detail of the PDMS fluidic (in grey) overlap to the SMR structure (in red), c) SMR chip bonded to the PDMS fluidic interface.34

Figure 3.13 Silicon mold fabrication and PDMS fluidic release: the process flow, for the mold realization consist of five different step that concern the photoresist coating (a), the transferring of the fluidic pattern by laser direct writing (b), the

photoresist development (which removes the non exposed photoresist)(c), the dry etching of the unprotected silicon surfaces (d), which allows to transfer the fluidic pattern on the silico wafer and the final photoresist stripping (e). Once the mold is fabricated the silicon surface have to be passivated by a PFOTS (f) deposition that is essential to ensure the PDMS de-molding after the polymerization (g-h).....34

Figure 3.14 Chamber pressure optimization. The best condition (red dot) was selected evaluating the variation of the water contact angle as function of chamber pressure, keeping constant the RF power and the exposure time.35

Figure 3.15 RF power optimization. The best condition (red dot) was selected evaluating the variation of the water contact angle as function of power applied, keeping constant the chamber pressure and the exposure time.....36

Figure 3.16 Exposure time optimization. The best condition (red dot) was selected evaluating the variation of the water contact angle as function of exposure time, keeping constant the RF power and the chamber pressure.....36

Figure 3.17 Aging test. The PDMS surface, activated with the best exposure parameters (RF power, chamber pressure and exposure time), were aged for different time in order to evaluate the strength of the PDMS-glass bonding even if the contact between the two material takes place after a variable amount of time.....37

Figure 4.1 Laser Doppler Vibrometer: experimental set-up. a) The head of the Laser Doppler Vibrometer and the vacuum chamber used for the mechanical characterization of the SMRs; b) schematic representation of the interferometric system; c) schematic representation of the vacuum chamber and the external actuation system.....39

Figure 4.2 Schematic representation of the Lock-in and Phase-Lock-Loop system, image from the Zurich instrument website (HF2LI/PLL system).....40

Figure 4.3 Example of a mechanical characterization of an SMR. Six different resonance modes for air (red line) and vacuum (grey line) measurement are reported, each of them is associated to relative the mode shape reconstruction.42

Figure 4.4 Q factor variation as function of the SMR length. Q factor values associated to different SMR length, the 20X and 50X-based fabrication are compared. Each SMR was characterized in air and in vacuum environment in order to evaluate the Q factor variation as function of the surrounding media.43

Figure 4.5 Evaluation of the width impact on the Q factor. SMRs with same length and thickness, but with different width, have been characterized in air and in vacuum and compared; a-b) in the graph the Q factor for 75 and 50 μm wide SMRs are reported, respectively; for each device is specified the ratio between the channel and the bulk volume (V_c/V_b).44

Figure 4.6 Glass SMR resonance distribution and responsivity. a) The distribution of the first resonance frequency, associated to three different SMR length configurations (450 – 500 – 750 μm), is reported. b) The responsivity associated to different SMRs is reported as function of their mass.49

Figure 4.7 Allan’s Deviation as a function of the filling fluid. The Allan’s deviation measurement for the same SMR, conducted in three different configurations: vacuum/vacuum (dark blue line), Air/Air (light blue line) and Air/Water (grey line). The first mentioned environment represents the surrounding medium and the second the filling fluid.51

Figure 4.8 Frequency shift as a function of the filling fluid. a) The first mode frequencies measured filling the SMR (fabricated with 50X objective) with five fluids of different density (calibration plot). b) The resonance frequency plotted for different fluid used to fill the SMR. c) The frequencies measurement as function of the filling liquids (calibration plot) has been repeated for the SMR fabricated with 20X objective. In this case, the liquids used for the test are slightly different respect to those reported in the graph (a).53

Figure 4.9 Q factor as function of viscosity and density of the filling fluid. a-b) Q factor variation due to the viscosity and density of the measured fluid. As expected, the variation follows a non-monotonic behavior for both the physical properties of the filling fluid.54

Figure 4.10 *Pseudomonas fluorescens* microgravimetric analysis. a) Mean relative frequency shifts (for the first resonance mode) due to the mass of bacteria contained in solution with different concentration. b) Number of bacteria extrapolated from the microgravimetric analysis and associated to different concentration.55

Figure 4.11 Repeatability of the bacteria-counting test. Mean resonance frequency shift associated to the solution containing different concentration of bacteria: the test was repeated two times with multiple sampling for each concentration, in order to determine the intra and inter-experiment repeatability. The number of bacteria was extrapolated from the average of the test-1 and test-2.56

Figure 5.1 Most common types of mesostructured frameworks obtained by the synthesis of mesoporous silica based materials. Picture from “Mesoporous silica nanoparticles: A comprehensive review on synthesis and recent advances” R. Narayan et al. *Pharmaceutics* 2018, 10, 118, doi:10.3390/pharmaceutics10030118.61

Figure 5.2 Surfactant micelles self-assembly into a rod-shape structure, which is used to direct the condensation and hydrolysis of the silica precursor forming the characteristic mesoporous framework of the silica based materials. Picture from “Mesoporous silica nanoparticles: A comprehensive review on synthesis and recent advances” R. Narayan et al. *Pharmaceutics* 2018, 10, 118, doi:10.3390/pharmaceutics10030118.62

Figure 5.3 Typical reaction pathway of hydrolysis and condensation of the silica precursor during the sol-gel synthesis of the silica based materials. Picture from “The Sol-Gel Handbook: Synthesis, Characterization, and Application”, First Edition 2015 Wiley-VCH.63

Figure 5.4 Nucleophilic attack pathway of the silicon atoms (alkoxysilane precursor) involved in the synthesis of the mesoporous silica materials under acidic conditions, where, X and Y are respectively R and H for the hydrolysis reaction or

R/H and $\text{Si}\equiv$ for the condensation reaction. Picture from “The Sol–Gel Handbook: Synthesis, Characterization, and Application”, First Edition 2015 Wiley–VCH. ...64

Figure 5.5 The silicon atoms involved during the hydrolysis and condensation of the akoxysilane; a) in acidic condition the central silicon is preferentially affected and represent the elongation point of the condensed network (chain-like); b) in basic condition the terminal silicon represent the main involved atom during the condensation giving rise to a branch-like network.65

Figure 5.6 pH of reaction affection the condensation/hydrolysis reaction. a) Kinetics of the silicon condensation rates as function of the pH and relative ratio neutral/charged species in solution; b) Possible pathway of interaction between the surfactant micelles and the silica precursors as function of relative charge of the species in solution. Pictures partially modified from “Synthesis of mesoporous silica nanoparticles” Wu et al. Chem Soc Rev 2013, DOI: 10.1039/c3cs35405a and form “A Review: Fundamental aspects of silicate mesoporous materials” Z.A. Alothman, Materials 2012 doi:10.3390/ma5122874.66

Figure 5.7 Synthesis protocol of mesoporous silica beads characterized by ultra large pores. a) Schematic representation of the mesoporous bare silica framework formation in acidic conditions; b) Schematic representation of the one-pot synthesis used for the formation of a functional mesoporous framework.72

Figure 5.8 Schematic representation of the final steps relative to the ELISA-like test. The beads previously incubated, with specific molecules of interest, were separated from the washing buffer and re-suspended in 500 μL of water (a–b). Subsequently, 15 μL of this solution were sampled and putted in a new Eppendorf (c). Finally, 200 μL of TMB and 200 μL of H_2SO_4 were added (with a waiting time of 45 sec) (d–e). The colorimetric reaction was quantified sampling 200 μL of the final solution (after the beads separation) (f).75

Figure 5.9 BET adsorption/desorption curves characteristic of different mesoporous silica beads: a–b–c) respectively synthetized at 22–14–12 $^\circ\text{C}$ using toluene as swelling agent; d) synthetized at 14 $^\circ\text{C}$ using TMB as swelling agent. In

the inset of each graph are displayed the SEM images of the mesoporous silica beads.78

Figure 5.10 BET pore volumes as function of the width distribution, characteristic of different mesoporous silica beads; a–b–c) respectively synthesized at 22–14–12 °C using toluene as swelling agent; d) synthesized at 14 °C using TMB as swelling agent. In the inset of each graph are reported the SEM images of the mesoporous framework obtained from the different synthesis methods.79

Figure 5.11 BET analysis of different modified mesoporous silica beads; a) comparison of the adsorption/desorption behaviour between the bare and the modified mSiO₂ with two different ratio of APTES (50NH₂ and 25NH₂) and APTES+SA (50COOH and 25COOH). b) comparison of the adsorption/desorption behaviour between the bare and the modified mSiO₂ with two different ratio of MPTMS (50SH and 25SH).81

Figure 5.12 BET analysis of different modified mesoporous silica beads; a) comparison of the pore width distribution between the bare and the modified mSiO₂ with two different ratio of APTES (50NH₂ and 25NH₂) and APTES+SA (50COOH and 25COOH). b) Comparison of the pore width distribution between the bare and the modified mSiO₂ with two different ratio of MPTMS (50SH and 25SH).82

Figure 5.13 SEM images of different modified mSiO₂ beads; a–b–c) are respectively the images relative to bare, APTES modified and MPTMS modified mSiO₂ beads; The series 1–2–3 represent the 5, 50 and 250 kX magnifications.83

Figure 5.14 Particles size analysis. a) Mesoporous silica beads diameter distribution obtained from the granulometry analysis at 1.3 mbar, b) SEM images (1kX) of the beads population.84

Figure 5.15 TGA of the unmodified mesoporous silica beads; a–b) are the thermograms obtained from two different synthesis batches of pristine mSiO₂ beads, respectively.....85

Figure 5.16 TGA of the unmodified mesoporous silica beads; a–b) are respectively the thermograms obtained from two different APTES content (1:50 and

1:25 ratio); c-d) are respectively the thermograms obtained after the modification of the APTES mSiO ₂ (1:50 and 1:25 ratio) with succinic anhydride post-synthesis treatment.	86
Figure 5.17 TGA of the unmodified mesoporous silica beads; a-b) are respectively the thermograms obtained from two different MPTMS content (1:50 and 1:25 ratio).....	87
Figure 5.18 FTIR spectra a) of bare and APTES or APTES/SA modified mSiO ₂ beads; b-c) magnification of the FTIR peaks related to the amine and carboxyl functionalities and to the siloxane framework, respectively.	89
Figure 5.19 Ellman's test a) Cysteine standard calibration curve used for the quantification of the unknown amount of SH functionalities; b) molecules density of SH functionalities for the MPTMS modified mSiO ₂ beads, the time of incubation with the DTNB reagent was varied in the 5 – 60 min range.....	91
Figure 5.20 FITC uptake test, a-b-c) the reduction of the FITC fluorescence intensity as function of the substrate used (bare and SH modified mSiO ₂ beads); the test was performed three times; d) FITC standard calibration curves related to the inter-experiment triplicates.	93
Figure 5.21 Figure 5.19 FITC molecules density a) grafted by the SH functionalities of the modified mSiO ₂ beads; b) microscope images of the FITC fluorescence intensity.....	94
Figure 5.22 Passivation using cysteine as blocking agent: in the graph, the different condition of pH and buffer used for the cysteine incubation are reported.	96
Figure 5.23 Cysteine passivation. Comparison of the effectiveness and reproducibility (a-b) of the passivation test for the bare and SH modified mSiO ₂ beads. The value are the average of three repetitions, and the error bars are their standard deviation.	97

Figure 5.24 Cysteine-BSA coupled passivation. a) Comparison of the effect of the passivation on the 50SH and 25SH modified mSiO ₂ beads and relative magnification (b-c).	98
Figure 5.25 BSA passivation. Evaluation of the effectiveness of the BSA used as pre-treatment and/or during the Str-HRP incubation. The OD scale was settled up to 2.25 in order to simplify the comparison with the graph reported in figure 5.23.	99
Figure 5.26 Passivation test using two different strategies, the test was conducted with the ssDNA probe immobilized on the beads surface. a) samples of bare and SH modified mSiO ₂ beads passivated with cysteine; b) second test conducted by coupling the passivating effect of cysteine with a post-treatment with BSA.	100
Figure 5.27 Evaluation of the passivation effectiveness if applied to the hybridization test, the strategies applied was the treatment with cysteine and subsequently with BSA during the Str-HRP incubation.	101
Figure 5.28 Evaluation of the ssDNA immobilization kinetic, the SH modified mSiO ₂ beads were incubated with the ssDNA and the kinetic of internalisation was evaluated by means of the UV-spectroscopy at different time of incubation.	102
Figure 5.29 ssDNA incubation volume, evaluation of the effect of the incubation volume and final suspension over the immobilized DNA molecules.	103
Figure 5.30 Evaluation of the DNA probe concentration, the ability to detect the DNA target was evaluated varying the probe concentration. The test was repeated in order to evaluate the reproducibility.	104
Figure 5.31 Evaluation of the time of incubation for the DNA target detection, considering two different concentration of DNA probe a-b) 1 μM and 1 nM. Two different TMB-HRP reaction time has been tested: 45 seconds and 5 minutes.	105
Figure 5.32 Minimum concentration of DNA target detectable, the concentration of incubation was varied in the 0-1000 nM (a) and 0-1 nM (b) ranges.	105

Figure 5.33 Evaluation of the effect of the TMB reaction time, different concentration of DNA target were detected at two reaction: a) 2 min and 20 sec, b) 5 min.....	106
Figure 5.34 Variation of the final suspension volume and evaluation of the related LOD, different volume of the final suspension were tested in order to detect the DNA target incubated in the 0–100 nM range. The limit of detection for each final suspension volume is reported in the graphs.....	107
Figure A.1 Schematic representation of the single clamped beam. In red is highlighted the embedded-channel path along the suspended structure and the connection with the inlets.	128
Figure A.2 First mode resonance frequencies. In the graph are represented the resonance peak and the Q factor for three clamped beam, two of them show a partial presence of the embedded fluidic channel near the clamping region.	129
Figure A.3 Allan’s deviation analysis. a) In the graph are reported the Allan’s deviation values as function of the time, comparing the behavior for a cantilever and a bridge suspended structure. b–d) Optical microscope images of the bridge and cantilever SMR.....	130
Figure B.1 First mode of resonance, for different micromechanical resonators characterized by variable length, width and thickness (a–b–c).	133
Figure B.2 Example of exponential decay fit used for the computation of the Q factor from the ring down analysis.	134
Figure B.3 Allan’s deviation analysis. The Allan’s deviation curves are reported in the graph and the close (blu line) and the open (red line) loop response was compared for different SMRs length, a–b) 450µm, b–c)500 µm and d–e) 750 µm.	136
Figure C.1 Optical microscope images relative to the ITO resistance test. In the images are reported the morphological aspect of the ITO(O ₂) and ITO samples before and after the KOH etching.	140

Figure C.2 Transmittance spectra for the ITO and ITO-(O₂) samples. In the graph are reported the transmittance curves before and after the KOH treatment. As reference is reported (red curve), the transmittance associated to the pristine fused silica. 141

Figure C.3 Optical microscope images relative to the Cr-Au/Cr-Au and Ti/Pt resistance test. In the images are reported the morphological aspect of the Cr-Au/Cr-Au and Ti/Pt samples before and after the KOH etching. 142

Figure C.4 Schematic representation of the process flow for the electrodes integration. The electrodes deposition and patterning were obtained following the depicted step by step process, which involves the metal deposition followed by the photoresist coating. The electrodes geometries were patterned by the means of a laser direct writing followed by the removal of the un-exposed resist. The geometry was finally obtained using an ion beam etching followed by the photoresist removal and the SMR release by KOH etching. 143

Figure C.5 SEM images of the electrodes deposited on the SMR structures. a) Top-view of the electrodes, the alignment was successfully obtained and the gap between the electrodes was perfectly centered along the SMR structure. b) detail of an adhesion defect of the Cr-Au/Cr-Au layer, probably due to the fused silica redeposition, along the SMR edges, during the femtosecond laser writing. 143

Chapter 1

Introduction

Biosensors are integrated platforms able to exploit particular sensing interface to detect biological phenomena [1], i.e. the antigen-antibody interaction, the DNA-DNA hybridization or even more complex mechanisms. One of the main advantages in the usage of the biosensors is the possibility to directly monitor a specific biological mechanism in complex matrix maintaining high sensitivity, selectivity and time stability [2]. This is mainly due to the particular sensing interface, which characterizes this type of sensors. The sensing interface is generally constituted of specific bioreceptors (i.e. enzyme, antibody, microorganism...) able to interact with the biological sample to be analyzed (Figure 1.1). The bioreceptor is generally immobilized or connected to the sensing system using different strategies, including physical adsorption, chemical cross-linking, or selective confinement inside dedicated trapping structures [3]. Then, the interaction between the receptor and the analyte must be converted in a measurable signal. For this reason, a second fundamental component of the biosensing system is the transduction module, which allows the conversion of the biological phenomena in a quantitative or qualitative information. Many different strategies, based on electrochemical, optical, piezoelectric, acoustic, microgravimetric and many other methods, can be exploited to actuate this conversion. Among the microgravimetric approaches, the micromechanical biosensors assume a great importance in the development of label-free sensing platforms with high mass sensitivity. The majority of mechanical biosensors can be classified, according to the operation mechanism, into Micro or

Nanoresonators, Suspended Microchannel Resonators and Quartz Crystal Microbalance.

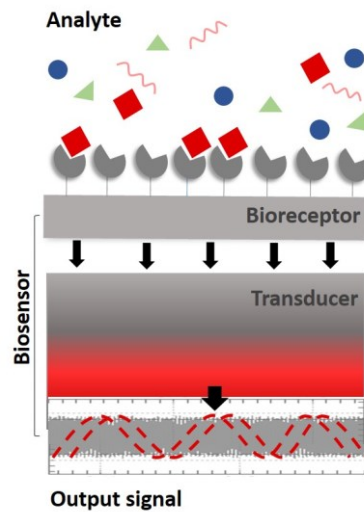


Figure 1.1 Schematic representation of a biosensor working mechanism. The most important elements that compose a biosensor are put in evidence, like the bioreceptor binding site, the transducer module and the output signal analyzer.

New approaches of micro and nanofabrication are increasing the use of the mechanical resonator as powerful sensing tool [4–9]. In particular, the ability to apply the standard wafer scale semiconductor processing techniques to the mechanical device fabrication has enlarged the field of application of these platforms [8]. The first typology of micrometer-sized resonator became popular with the atomic force microscope (AFM) invention in 1986 [10]. This approach takes into account the possibility to obtain topographic information, of micron-sized features, by raster scanning with a miniaturized phonograph. A sharp tip mounted on a cantilever beam was used to probe the sample surface [11,12], which bends according to the interaction forces between the tip and the sample. The small dimensions of the cantilever (micro or submicron) ensured a high resonance frequency, which makes the system less sensitive to the external vibrations and guarantees a low spring constant. With the pioneering works by Barnes *et al.* and Thundat *et al.* in 1994, these mechanical platforms were modified removing the sensing tip and the beam resonator started to be used in a wide range of applications, ranging from health science to physical-chemical research. In their work, the bimorph effect, due to a one side gold coating on a cantilever, which normally causes severe drift problems to the AFM set-up, was exploited to realize a very sensitive micron-size thermometer [13].

Moreover, following studies demonstrated that keeping a metal-coated cantilever at constant temperature, small changes of humidity or the presence of vapors could be easily detected analyzing the surface stress [14,15]. Exploiting the same concept, the cantilever sensors have been used to online measure the formation of self-assembled monolayer (SAM) [16], opening a new field of applications related to the monitoring of molecular binding phenomena [17–19], thus making the cantilevers more and more attractive as label-free sensing platforms [20,21]. One of the first innovative work on this field was the study of the specific binding between two complementary DNA strands [22]. The widespread use of these platforms in the biosensing field is mainly due to the remarkable ability to detect small variations of mass or surface stress that reveal the presence of specific biomolecular recognition events that are usually difficult to detect. Furthermore, these intrinsic characteristics scale advantageously with the reduction of the physical size of the resonant platform. For this reason, considering the miniaturized dimensions (micro or nanoscale), the cantilevers hold promises as portable and highly parallelized sensors [23]. These characteristics coupled with the possibility to operate in different modes [24] allow to simultaneously obtain different information linked to the variation of the cantilever mechanical properties.

The two main operational methodology are the static and dynamic mode [25]. In the former, the static deflection of the cantilever is measured and exploited to directly measure the surface or bulk stress induced respectively by molecules or other material deposition and by humidity or temperature changes [13,26–29]. The second operational mode is based on the possibility to directly and quantitatively link the resonance frequency of the resonator with its mass. Thus, if the mass changes, due for example to a molecules layer deposition or other immobilization/absorption phenomena [19,30], the change can be estimated by monitoring the cantilever resonance frequency shift. This method allows to reach impressive mass sensitivity since the minimum detectable mass variation is related to the total mass of the device. Further improving the operating condition, like working in vacuum environment, the dynamic mode allows to estimate mass changes in the atto to zeptogram scale (e.g. by using nanoelectromechanical systems [31,32]).

Unfortunately, when the aim of the sensing application is the detection and the study of biological species in their native environment, comes out one of the predominant problem of these devices: the viscous drag damping, which drastically

affects the quality factor (Q) and the effective mass [33,34]. Consequently, the minimum detectable frequency and the sensitivity of the device are drastically reduced [35]. Different possible solutions have been proposed, such as microplates [36], micropillars [37] and plate wave sensors [38] that are able to reduce this limitation even if their sensitivity result to be inferior if compared to the beam based resonators. To overcome these problems different strategies have been employed, including the “dip and dry” approach that consists in the measurement of the resonance frequency, in air or in vacuum, immediately after the exposure of the resonator to the desire incubation solution followed by the drying of the cantilever surface [39]. Unfortunately, this approach has numerous drawbacks like poor reliability, increase of possible contaminations, unfeasibility of real-time measurements and time consuming sample preparation. The most attractive alternative was presented by Burg and Manalis in 2003 [40]. In their work, a new approach to minimize the viscous drag and the damping problems associated with the vibration of a cantilever in fluids was shown for the first time. They proposed to overcome these phenomena confining the fluid directly inside the cantilever, leaving the beam exterior in vacuum or in a gaseous environment. In order to do that, an innovative design was proposed. The standard suspended resonator shape was transformed into a suspended microchannel resonator (SMR) by empty the inner volume of the suspended beam (Figure 1.2). Furthermore, thanks to the possibility of vacuum packaging the whole suspended structure, the characteristic high sensitivity was preserved [33].

Confining the liquid inside the beams means to be able to get mass and density information and to carry out real time biomolecular detections [24]. Furthermore, this new design enabled not only to avoid the common problems related to the in-fluid measurement, but also to directly track both position, velocity and growth of new target analytes like bacteria, cells and particles. However, the fabrication process still represents the main drawback in the implementation of these platforms for the development of new point-of-care devices and for the large-scale integration with μ HPLC, PCR and flow cytometers [41,42]. In fact, the SMRs are currently fabricated with challenging, time-consuming and expensive micromachining techniques [33]-[43] that require complex multi-step microfabrication procedure for the creation of the embedded microfluidic channel [33,44,45]. An alternative

solution would be needed to guarantee a widespread diffusion of this sensing technology for biological and chemical detection.

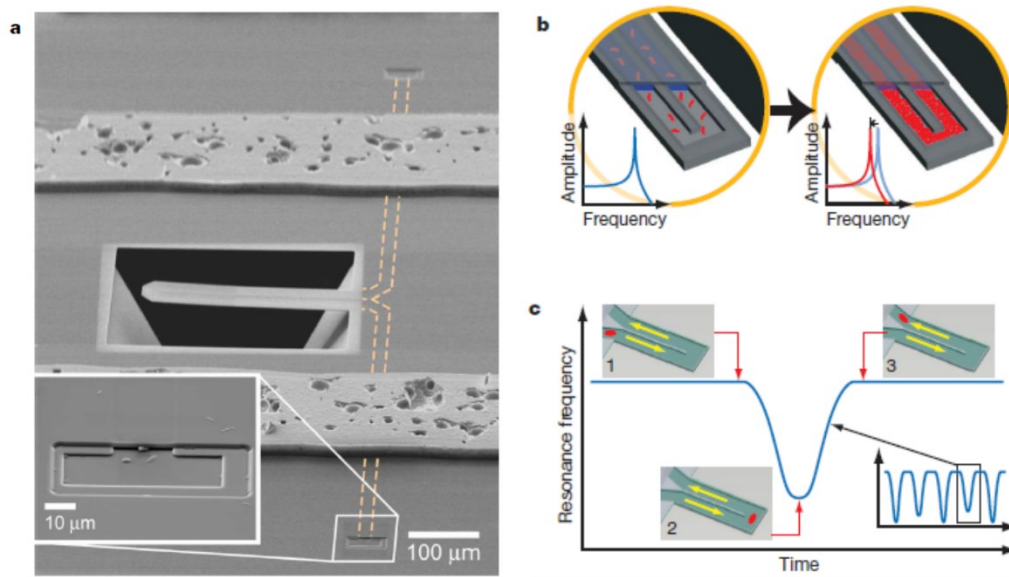


Figure 1.2 Suspended microchannel resonator a) SEM images of a SMR characterized by the cantilever shape, the dashed line highlights the channel path (from Manalis et al. 2006); b) particular of the embedded microfluidic channel; c) correlation between the particles position and the amplitude of the resonance peak (from Manalis et al. 2007).

Even if the SMRs have found a wide range of application in the biosensing field, especially in the single cell and single particle studies, the exploitation of these platforms, as potential transduction system for the improvement of existent bioassay (i.e. biomarkers quantification, binding kinetics...) has shown limited diffusion [46,47]. The main problem is the poor specific area of the embedded channel that should be used as capturing surface for target molecules detection. Furthermore, to guarantee the specific binding of the capturing molecules on the channel surface, a functionalization process must be taken into account [46]. This approach requires to set-up a dedicated system of functionalization steps able to guarantee a high coating homogeneity. In order to avoid these problems, an alternative is represented by the integration of high adsorbent surfaces into the SMR, for example by using high porous beads as carriers. The beads can be flushed back and forth in the SMR monitoring the mass variation. In this way, both the capturing molecules loading and the target binding can be real-time monitored.

Moving from the 2D-based system of the channel wall [8,9] to the 3D-based system of the beads offers the possibility to overcome the main problems linked to

the channel functionalization. In fact, the functionalization of the beads can be done in batches, reducing the statistical difference of the process, and can be directly integrated during the beads synthesis [20–22]. Furthermore, the usage of porous beads increases the surface area available for the immobilization of the capturing molecules [10–12], fundamental in the analysis of low volume samples containing low concentrations target analyte [16].

Materials like mesoporous silica has been deeply studied as ideal substrate for the synthesis of micro or nanoparticles with high surface area and high modification degree that involve both the morphology (beads and pores dimensions) and the surface chemistry, which can be modulated depending on the final application [22–24]. In the field of medical microdevices, the possibility to fully integrate a substrate with high capturing capability, high-throughput properties and scalability, can be considered as one of the most important requirement. The use of porous beads can supply these needs and can be used as versatile substrate for high throughput and label-free detection approaches.

Considering the two main constrains, which limits the SMR diffusion as effective bioassay platform, this thesis work was first focused on the development of a new fabrication approach based on the femtosecond laser direct writing. In this context, the as fabricated glass SMRs were deeply characterized from the mechanical point of view. Furthermore, the capability of the SMR to distinguish liquids with different concentration was tested and as proof of concept, the resonators were used as microgravimetric platform for *P. fluorescens* counting. In the second part of the work, the possibility to develop a new biosensing approach, based on the integration of mesoporous beads into the SMR, was investigated. In particular, the mesoporous silica was studied as suitable substrate for the synthesis of functionalized microbeads. Afterwards, a protocol that takes into account the reduction of non-specific contaminants was optimized and a bioassay based on a DNA–DNA interaction was developed. The future integration of the two components optimized during this thesis work, the bead-based assay and the innovative glass SMR, would increase the potential application of these resonant platforms in the field of the biosensing technology.

Chapter 2

Fundamentals of Micromechanical resonator

2.1. Introduction

A mechanical resonator is a sensitive suspended structure characterized by a specific frequency of vibration. According to the equipartition theorem, for an ideal (lossless) vibrating mechanical structure, the kinetic energy and the potential energy are endlessly converted at the *eigenfrequency* with a constant vibrational amplitude. This phenomenon occurs at discrete vibrational modes, defined *eigenmodes* [48]. However, for a real mechanical structure the commutation between kinetic and potential energy is affected by small losses at every cycle, due for example to the medium interaction, clamping system and other intrinsic losses. Therefore, in a real mechanical structure the *eigenfrequency* is more appropriately defined *resonance frequency* and it is associated to a well define *resonance mode* [49].

Each resonator is characterized by a singular natural resonance frequency (f_0) that could change as function of the mass, force or stress variations applied to suspended structure, making these platforms particular attractive in the sensors field. Depending on the final purpose, the mechanical resonators could be shaped following different geometries [50] like beams [51–54], strings [55], diaphragms, plates [56] or membrane [57,58].

2.2. Resonance Frequency

Focusing the attention on the beam resonators, for a thin structure ($L \gg w \gg h$) the behaviour of the system can be easily described by the “Euler Bernoulli Beam Equation” [59]:

$$EI \frac{\delta^4 z}{dx^4} + \rho A \frac{\delta^2 z}{dt^2} = 0 \quad (2.1)$$

Where E is the Young’s modulus, I is the geometric moment of inertia, ρ is the mass density and A is the cross sectional area.

The modelling of the bending behaviour can be derived under three fundamentals kinematic assumption:

- The cross-section is infinitely rigid (own plane)
- The cross-section return plane after deformation
- The cross-section should be normal respect to the deformed axis

2.2.1. Single clamped beam

The Euler Bernoulli equation is a fourth order differential equation, therefore four boundary conditions are needed to solve it and derive the resonance frequency (f_n) of the system. If we consider a single clamped beam, as show in Figure 2.1., these boundary conditions can be obtained bearing in mind the following assumptions: no displacement or rotation should be shown at the fixed end of the beam, and the bending moment or shear force should not interest the free end of the beam



Figure 2.1 Graphical representation of a single clamped beam (cantilever).

The resonance frequency can be obtain implementing the related boundary conditions and can be defined as,

$$f_n = \frac{(k_n L)^2 t}{2\pi L^2} \sqrt{\frac{E}{12\rho}} \quad (2.2)$$

Where $k_n L$ is the wave number, n is the operation mode, E is the Young's modulus, ρ is the density and, t is the thickness of the beam.

The wave number change in function of the mode of operation and is given by,

$$k_n L = 1.875, 4.694, 7.855 \quad (2.3)$$

when $n = 1, 2, 3$

$$k_n L = \frac{(2n - 1)\pi}{2} \quad \text{when } n > 3 \quad (2.4)$$

The first four flexural modes are clearly visible in Figure 2.2.; increasing the number of modes, new nodes are added: these points of non-vibration limit the oscillation of the structure and decrease the amplitude of the associated vibrational mode. At each n -mode is associated $n-1$ nodes.

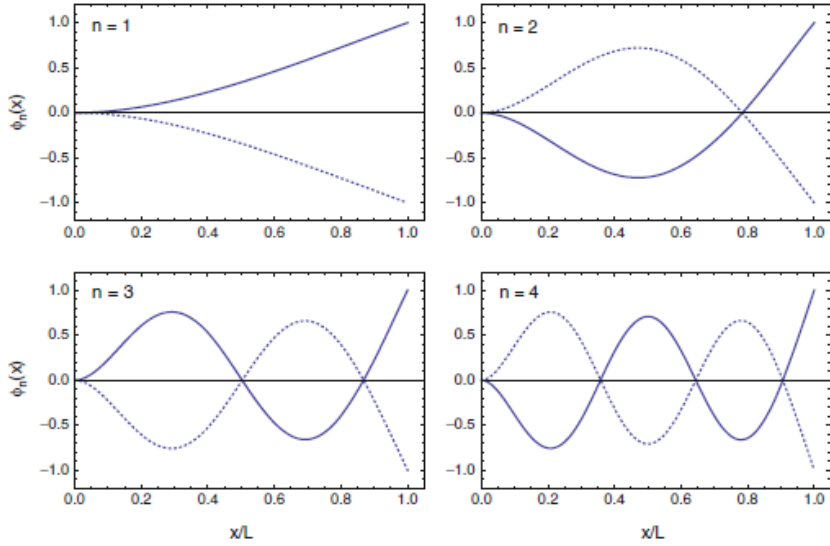


Figure 2.2 Schematics representation of the first four flexural or bending mode of a cantilever. Picture from the “Fundamentals of nanomechanical resonator, Schimit et al. Springer 2016).

2.2.2. Double clamped beam

In the case of a doubly clamped beam (Figure 2.3) the suspended structure is fixed at both ends, therefore the boundary condition derive from a single assumption: no slope or displacement due to the clamp at the fixed ends

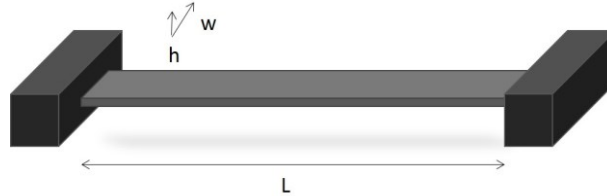


Figure 2.3 Graphical representation of a doubly clamped beam.

As said before for the single clamped beam, implementing the boundary conditions it is possible to define the characteristic resonance frequency of the structure as,

$$f_n = \frac{(k_n L)^2 t}{2\pi L^2} \sqrt{\frac{E}{12\rho(1-\nu^2)}} \quad (2.5)$$

where $k_n L$ is the wave number, n is the operating mode, E is the Young's modulus, ρ is the density, ν is the Poisson ratio and L is the length of the beam.

The wave numbers associated to the first four flexural modes, visible in Figure 2.4, are given by,

$$k_n L = 4.7300, 7.8532, 10.9956 \quad (2.6)$$

when $n = 1, 2, 3$

$$k_n L = (2n + 1) \frac{\pi}{2} \quad \text{when } n > 3 \quad (2.7)$$

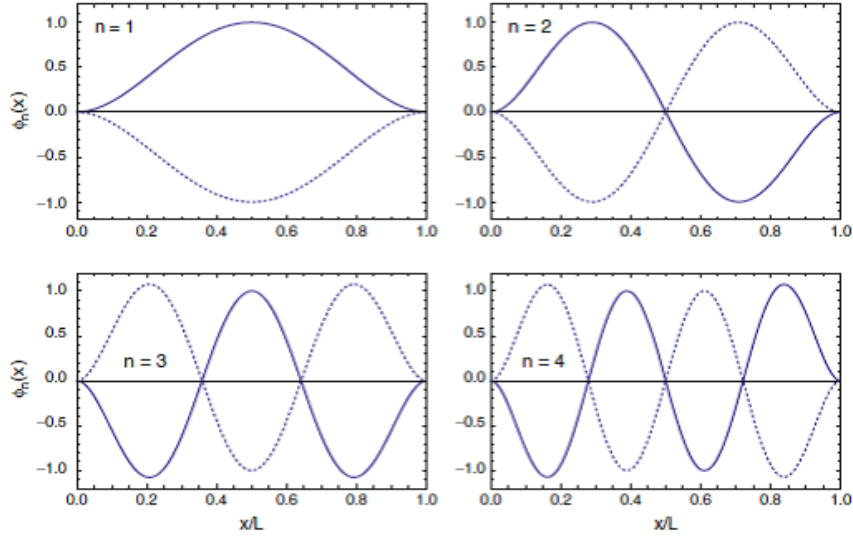


Figure 2.4 Schematics representation of the first four flexural or bending mode of a doubly clamped beam. Picture from the “Fundamental of nanomechanical resonator, Schimit et al. Springer 2016).

2.3. Quality Factor

The quality factor (Q) is the parameter that defines the sharpness of the resonance peak. From the physical point of view, the Q factor is the ratio between the amount of energy stored and the energy lost at the resonance,

$$Q = 2\pi \frac{W}{\Delta W} \quad (2.8)$$

where W and ΔW are respectively, the totally energy stored and lost during one cycle of oscillation.

In other words, the Q factor describes the damping effect at which the resonator undergoes: low damping result in high Q factor and vice versa. This parameter can be calculated as the ratio between the resonance frequency and the frequency bandwidth at -3 dB of the maximum amplitude (Figure 2.5),

$$Q = \frac{f_r}{(\Delta f)_{-3 \text{ dB}}} \quad (2.9)$$

A good approximation of the Q factor can be calculated taking into account the ratio between the resonance frequency and the full width at half maximum (FWHM), derived from the Lorentian pick of the curve.

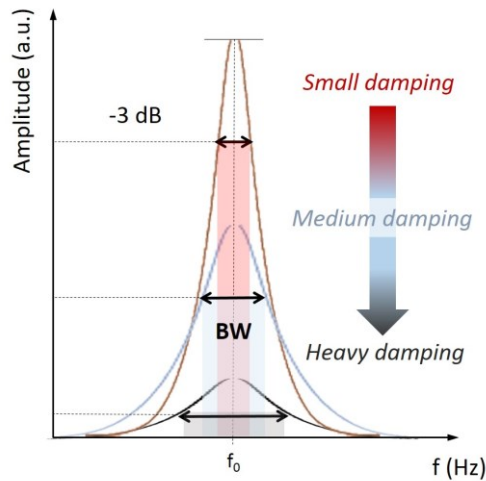


Figure 2.5 Q factor and damping effect, schematic representation of the bandwidth variation (evaluated at -3 dB) due to the damping effect.

A second method to define the Q factor of a resonator is represented by the ring down analysis. In this case the resonator is put under vibration at his natural resonance frequency, then switching off the drive signal the amplitude of the oscillation is recorded while it decreases as function of time (Figure 2.6). The ring-down response to initial excitation is therefore used to evaluate the Q factor taking into account the logarithmic decrement method.

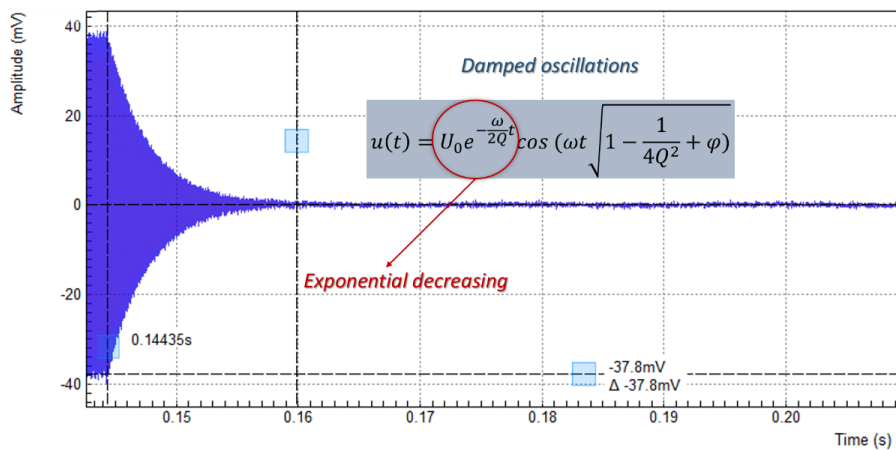


Figure 2.6 Ring-down response to an initial excitation, the exponential decrement behaviour when the driving signal is switched off is reported.

The decay of the resonance amplitude follows an exponential law that can be expressed as:

$$u(t) = U_0 e^{-\frac{\pi f}{Q}t} = U_0 e^{-\frac{t}{T}} \quad (2.10)$$

where, f is the resonance frequency, Q is the quality factor, t is the time and T is the time constant and can be used to determine the quality factor as:

$$Q = \pi f T \quad (2.11)$$

Generally, high Q factor means high vibrational amplitude and sharp peak at the resonance and both are related to precision with which it is possible to determine the resonance frequency of a mechanical resonator. For this reason, a high Q factor is desired for applications that require high sensitivity to distinguish small mass variations. Many different dissipation mechanisms are involved in the definition of the quality factor.

$$\frac{1}{Q} = \frac{1}{Q_{\text{medium}}} + \frac{1}{Q_{\text{clamping}}} + \frac{1}{Q_{\text{intrinsic}}} + \frac{1}{Q_{\text{other}}} \quad (2.12)$$

where, Q_{medium} represent all the losses due to the interaction of the mechanical resonator with both fluidic and ballistic medium (i.e. liquid damping and gas damping due to the fluid presence inside and outside the mechanical structure). Q_{clamping} stands for all the losses generated from the physical clamping sites of the structure, and $Q_{\text{intrinsic}}$ is a sum of all the dissipation mechanisms that can happen within the bulk or at the surface of the resonator. Q_{other} describe different dissipation mechanisms that can derive from other sources, like the *electrical charge damping*, due to the presence of charges tapped on the mechanical structure, or the *magnetomotive damping*, which derives from electrical dissipation in resistive element, often used for the transduction techniques.

2.4. Frequency response to mass

The mechanical resonators are very sensitive to change of mass, temperature, and applied force: these phenomena cause a response of the device, such as a change in frequency or amplitude of vibration [60]. The response to mass changes can be easily described considering the frequency of the first order of vibration, deriving from the equation of the simple harmonic oscillator derived from the lumped-element model,

where the resonant system is described by the mass, spring and dashpot approximation (Figure 2.7),

$$f_n = \frac{1}{2\pi} \sqrt{\frac{k}{m}} = \frac{\sqrt{k}}{2\pi} m^{-\frac{1}{2}} \quad (2.13)$$

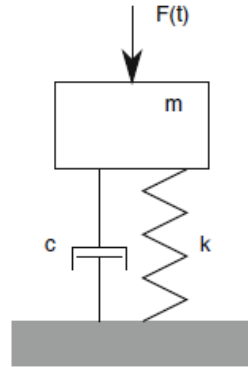


Figure 2.7 One-dimensional oscillator schematically represented taking into account the damped-element model. Picture from the “Fundamental of nanomechanical resonator, Schimit et al. Springer 2016).

Therefore, for small variations, the mass change and the frequency shifts are linked by the following relationship:

$$\Delta m \approx -2 \frac{f_{n+1} - f_n}{f_n} m = -2 \frac{\Delta f}{f_n} m \quad (2.14)$$

where f_{n+1} is the frequency after the mass added and Δf is amount of the shift.

This approximation is valid only in linear oscillator regime; indeed, in non-linear condition the resonator is not able to instantaneously dissipate the energy accumulated and the beam stiffness increase, affecting the resonance frequency.

This model shows some limitations: in this case the beam is described by a spring with punctiform mass and dissipation. Nevertheless, introducing the effective parameters the individual resonance of a continuous mechanical structure can be simplified using this model,

$$f_n = \frac{1}{2\pi} \sqrt{\frac{k_{eff,n}}{m_{eff,n}}} \quad (2.15)$$

where k_{eff} and m_{eff} are the effective spring constant and mass of a specific normal mode. After a mass change, due for example to the deposition of a molecule with mass equal to m^* , the new resonance frequency is given by,

$$f_{n+1} = \frac{1}{2\pi} \sqrt{\frac{k}{(m + m^*)_{eff}}} \quad (2.16)$$

Now it is clear that applying a change in mass, force or other physical parameters, the frequency is simultaneously shifted to a new value. The ability to detect the change that causes a detectable frequency shift is defined responsivity and is given by,

$$\mathfrak{R} \approx \frac{\Delta f_{(meff)}}{\Delta m_{eff}} \quad (2.17)$$

If the change of the input parameter is small (Δm_{eff}) the response can be linearized. Thus, the responsivity can be described as the linear slope of the response to the related stimulus. If we consider the sensor output (f) as function of the input parameter (m_{eff}), the responsivity is given by,

$$\mathfrak{R} = \frac{\partial f_{(meff)}}{\partial m_{eff}} = -\frac{f_{(meff)}}{2m_{eff}} \quad (2.18)$$

Furthermore, it is important to minimize the responsivity to other inputs in order to avoid cross-response.

Considering that one of the wide applications of the resonant sensor is the detection of small masses, it is important to establish the minimum amount of mass (Δm_{min}) that causes a detectable frequency shift (Δf_{min}). This parameter is called sensitivity and can be approximated as follow,

$$\Delta m_{min} \approx \mathfrak{R}^{-1} \Delta f_{min} \quad (2.19)$$

As we can see from the relation above, the minimum amount of detectable mass is dependent on the minimum detectable frequency shift. This value is directly affected by the frequency resolution,

$$\delta f_{min} = \frac{\Delta f_{min}}{f_0} \quad (2.20)$$

and it is linked to the noise deriving from the read-out system and the resonator itself. Using this expression of frequency noise, it is possible to reformulate the minimum detectable mass as

$$\Delta m_{min} = \delta \mathfrak{R}^{-1} \delta f_{min} \quad (2.21)$$

$$\delta \mathfrak{R} = -\frac{1}{2m_{eff}} \quad (2.22)$$

From the above relations, it is clear that the minimum detectable mass is principally affected by two intrinsic characteristics of the resonator: the mass itself and the Quality factor.

2.5. Frequency noise

The frequency stability is described by the phase noise measurement of the oscillator and it is generally defined for a set of measured values. There are numerous methods to measure the frequency or phase noise, specifically they can be grouped in two big characterization methods: spectral domain based or time domain based. Focusing the attention on this last strategy, one of the approach that is typically used is represented by the Allan deviation.

2.5.1. Allan's deviation

The resolution and accuracy of a measurement done with a mechanical resonator, can be limited by random fluctuation (noise) and by variation of the instrumentation parameters (drift) [61]. In order to characterize how these parameters can affect the system performance, it is necessary to find the best way to distinguish the different types of noise and drift. Unfortunately, the usage of the standard deviation does not allow this distinction [62]. In fact, this method is based on the variation of each

individual measurement from the mean measured value and taking into account the magnitudes of these phenomena, it results difficult to evaluate the overlap in time or in spectral power density.

The Allan deviation analysis provides an effective way to analyse the noise and drift components. In contrast to the standard deviation, this method is based on the measurement to measurement variation, and the data, represented in the form of log-log plot (magnitude versus time), provides the way to identify different types of noise and drift [48]. In our application, the Allan deviation provides a measure of the frequency variability averaged over a time period [63] (Figure 2.8).

The Allan deviation can be described as the square root of the variance, and it is the difference of two successive fractional frequency, $y(i)$ and $y(i+1)$, measured respectively at time $t_{0+i}\tau$ and $t_{0+(i+1)}\tau$ and it is generally defined as:

$$\sigma(\tau_0) = \sqrt{\frac{1}{2} \langle (\Delta y)^2 \rangle} = \sqrt{\frac{1}{2(N+1)} \sum_{i=1}^N (y_{i+1,\tau} - y_{i,\tau})^2} \quad (2.23)$$

where τ is the averaged time.

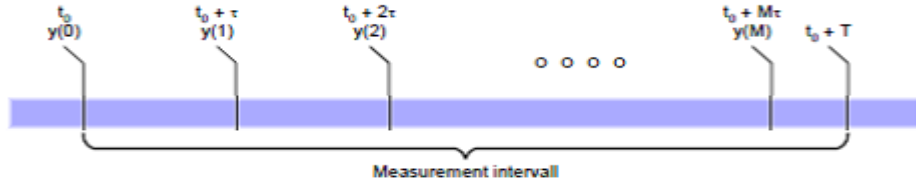


Figure 2.8 Time scale of the measurement interval. Picture from the “Time domain oscillator stability measurement, Allan variance”, Application Note Rohde&Schwarz 2015.

Using the Allan variance for a given integration time, it is possible to directly estimate the frequency noise starting from the phase fluctuation.

The main time dependent variations are three:

- White noise and thermomechanical noise, which are directly proportional to $\tau^{-1/2}$ and generally affect the resonator behaviour during the initial time frames;
- Flicker noise that gives a flat contribution (τ^0) through the integration time;

- Random walk and thermal drift, which are associated with the $\tau^{1/2}$ behaviour and generally affect the measurement at long time frames.

Taking into account the log-log plot of the Allan deviation as a function of the sample averaging time (Figure 2.9), the mentioned signal variations can be easily distinguished and analysed.

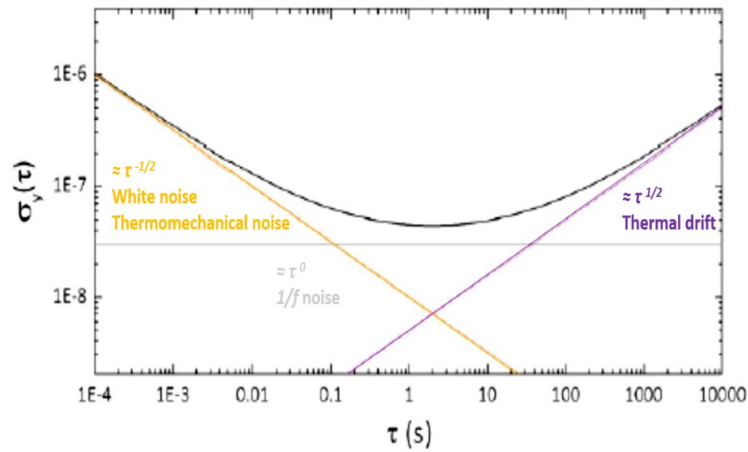


Figure 2.9 Allan deviation log-log plot, the curve represent the typical behaviour of the Allan deviation as function of the sample averaging time. Picture from the “Fundamental of nanomechanical resonator, Schimit et al. Springer 2016).

Chapter 3

SMR Design and Fabrication

3.1. Introduction

In the last decade, thanks to the pioneer works of Manalis and coworkers [64,65], the usage of SMRs is giving a large contribution in bioanalytes characterization and development of a new biosensing concept. Indeed, the SMRs can reach impressive mass resolution (up to 10^{-15} g) coupled with high throughput [66]. These characteristics are quite suitable for the study of small variation in the mass and density of single particle and cell [23,67]. Nevertheless, the fabrication process is generally quite complex and based on traditional micromachining approaches [33]. Furthermore, in order to reach such high mass resolution the resonator need to be packaged in a vacuum environment that reduces the viscous damping produced during the vibration of the beam in air [34].

In this work, it is proposed the use of the femtosecond laser writing process that is widely applied in the production of microfluidic lab-on-chip [68–71].

This fabrication process brings interesting advantages if applied to the SMRs fabrication. First, the femtosecond laser writing can be exploited to highly simplify the standard SMR fabrication, which normally needs numerous steps of bulk and surface micromachining [33]. With this approach it is has been possible to define the resonator geometry and the embedded channel in a single step, using a transparent material that in principle can be amorphous or crystalline [72,73]. Using a well-known material like fused silica [74–76], it is possible to couple this fabrication with

other post-processing modifications via standard micromachining, for the integration of other component necessary for example for the transduction of the device or to connect a microfluidic system.

The femtosecond laser patterning can be considered a “cold” process able to reduce the generation of bulk stress related to the local heating due to the fabrication. Furthermore, this approach enables to define the SMR geometry and the consequent beam release working with a single material.

3.2. Femtosecond laser micromachining: physical mechanism

The usage of femtosecond laser processing is currently attracting great interest from the scientific community [77]. In order to understand this interest, it is important to explain how transparent dielectric materials interact with the light, and in particular which is the absorption processes that governs the interaction between intense laser pulses and matter [78–80].

Commonly, if a transparent dielectric material is exposed to a continuous low intensity illumination, the light will be transmitted, indeed these materials show an energy gap (E_g) greater than the single photon energy ($h\nu$) [81]. Using a laser pulsed illumination, the interband transition, between valence and conduction band, is equally forbidden, if we consider the possibility that linear absorptions takes place. However, the transition can be promoted, at high intensity, by non-linear absorption phenomena [82] and three different processes can be involved: multiphoton (MPA), tunneling and avalanche ionization [83,84]. For multiphoton ionization, n photons are simultaneously absorbed such that the total energy ($n h\nu$) is enough to pass through the energy gap. The tunneling ionization can take place only if the electric field of the laser pulse is sufficiently high to reduce the Coulomb potential energy barrier, enabling the tunneling of an electron from the valence band to the conduction band. Finally, the avalanche ionization occurs thanks to the presence of an electron in the conduction band, due for example to one of the phenomena explained above or to thermally excited impurity or defect states. When this electron absorbs energy from multiples photons the energy increase and become greater than the band gap energy, causing the excitation of electron from the valence to the conduction band.

The probability that one of these non-linear absorptions occur depends on the duration of the pulse [79]. For long pulse (pico to nanoseconds) the local peak intensity result too low and multiphoton or tunneling ionization are forbidden even for rather high pulse energy. In this case, the interband transition can be only promoted by avalanche ionization if an initial “free electron” is present in the conduction band due to impurities or dislocation. Unfortunately, their presence in the material is subjected to large fluctuation and this mechanism results poorly reproducible and erratic. On the other hands, using a short laser pulse (sub-pico to femtoseconds) the peak intensity results high enough to promote multiphoton and tunneling ionization.

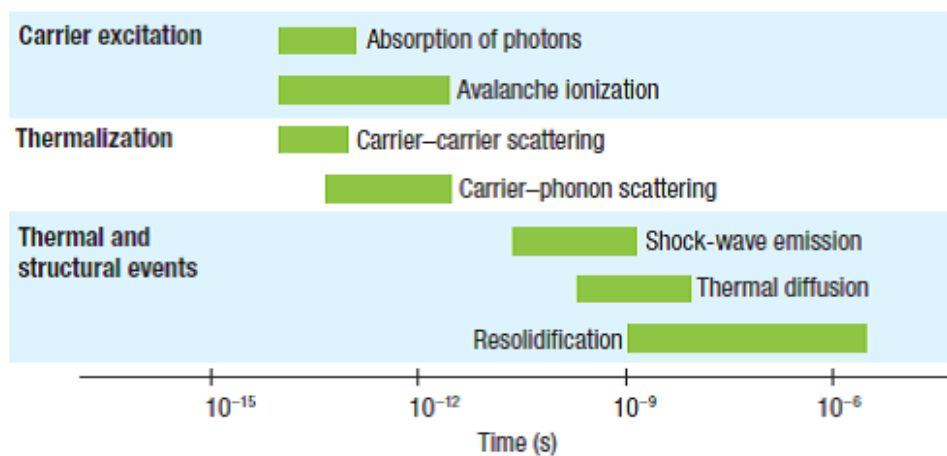


Figure 3.1 Time scale of the femtosecond laser pulse/transparent material interaction. The green bars show the typical time scale of different fundamental processes involved during the irradiation. Picture from “Femtosecond laser micromachining in transparent materials”, Gattass et al. Nature Photonics, Vol 2 April 2018.

If the intensity exceed a certain threshold, some free electrons in the focal volume act as “seeds” for the avalanche ionization, starting a ripple effect that increases the number of free electrons and turns the material into strongly absorbing [81]. Furthermore, for short pulses the free electron plasma formations occur on a shorter timescale and the energy transfer to the lattice is avoided (Figure 3.1). Indeed, this process requires typically few picoseconds. It is therefore clear that using the same light but exposing the material to ultrashort pulses the interaction between the light and the matter causes a permanent change of the material properties in a controlled and reproducible fashion [85]. Moreover, only a small volume inside the bulk is affected and typical problems due to long pulses [71], like microcracks, shockwave and thermal diffusion [86,87] are avoided (Figure 3.2).

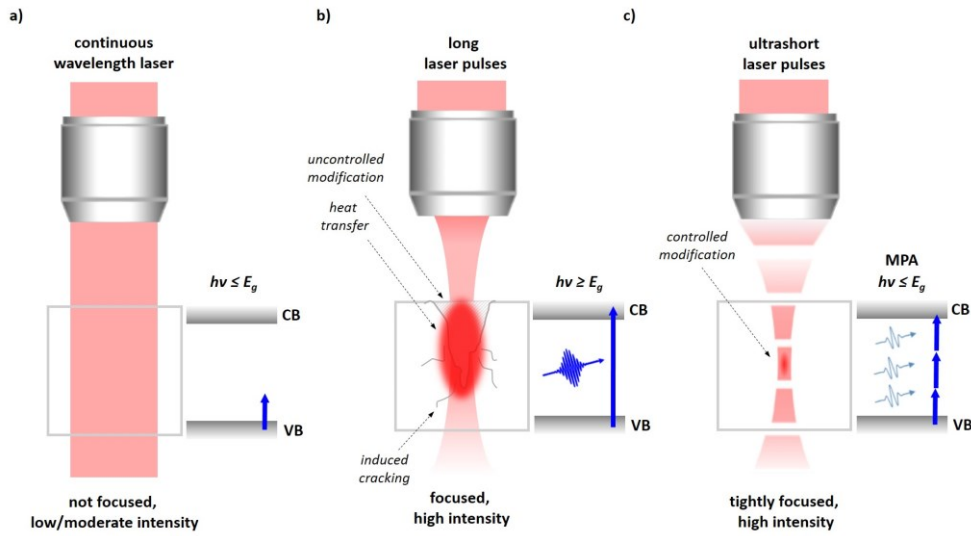


Figure 3.2 Schematic diagram of different laser matter interaction, a) continuous wavelength laser unfocused resulting in the transmission of the sub-band gap light, b) long pulsed laser focused in the solid volume produce an uncontrolled modification of the matter, c) ultrashort pulsed laser tightly focused enable the controlled modification of the volume exposed to the laser light.

The resulting physical and chemical changes are depended on the material properties and on the exposure parameters, like energy and pulse duration, wavelength of the incident light and repetition rate. For example, in glass the non-linear absorption and relative material modifications take place for intensities around $1\text{--}5 \times 10^{13} \text{ W/cm}^2$, corresponding to a fluency of $1\text{--}5 \text{ J/cm}^2$ for 100 fs pulse duration. The relative pulse energy needed to reach the desired fluency depends on the focusing conditions and can range from μJ s to nJ s [70].

3.3. Femtosecond writing principles

Using an ultrafast laser, the modifications can be induced not only at the surface of the transparent material, but also in the volume. With other techniques (nanosecond UV laser) the modification start at the first contact point between the laser and the material [71], instead for femtosecond laser the matter modification occurs only in the beam focal volume that can be easily moved inside the transparent materials. The modifications induced by a femtosecond laser can involve physical or chemical properties of the material, like refractive index, optical susceptibility, chemical susceptibility [88], crystal structure, morphology and absorption coefficient, just to cite the most important [78,80]. Thanks to such properties, coupled with the cost

effective process and the possibility to manipulate different substrate, the femtosecond laser writing is becoming one of the most interesting techniques for a variety of new applications. The possibility to simplify the micromachining of transparent materials like glass [78], crystals [73] and polymer [72], using one step procedure is becoming more and more attractive for lab-on-chip [71] and driving source for particles accelerators.

The fabrication of 3D structures by ultrashort pulsed laser can be achieved by two different methods. The first is commonly named “femtosecond laser-assisted etching” [71,88]. In this case, the laser is used to induce a local modification of the chemical resistance against specific etching reagents. After the exposure, the material undergoes to a selective wet etching that allows to remove the exposed part. The second method consists in the direct ablation of the glass and is commonly named “water-assisted laser drilling” [71].

The most common procedure used for the fabrication of embedded structure in glass is the femtosecond laser-assisted etching. The possibility to write directly inside the glass and to remove selectively the laser-modified region is particularly suitable for the creation of buried microfluidics [71,89], and suspended structures. After the laser exposure, the change of chemical resistance against specific etchant reagents is probably due to the variation of Si-O-Si bond angle under hydrostatic pressure or compressive stress induced by the laser irradiation [70]. A second mechanism that could explain the rising chemical susceptibility, takes into account the formation of self-ordered nanocracks [90] with perpendicular orientation to the laser polarization direction. In fact, the presence of these nanocracks can explain the acceleration of the wet-etchant diffusion inside the modified region, with the resulting etching rate increase. Both the hypothesis are still under debate.

Even if the mechanism that regulates the behavior of the material after the laser exposure is not yet clear, two different wet etchants can be used to remove the modified material [88]. A solution of Hydrofluoric Acid (HF) [91] or a safer alternative represented by the use of Potassium Hydroxide solution (KOH) [92]. Even if the etching rate, for this second etchant, is lower compared to HF solution, it seems quite suitable for the fabrication of microchannel with aspect ratio of about 200:1 [93,94].

The main problem due to this fabrication approach is the surface roughness after the wet etching [70]. Compared to standard micromachining procedures, the roughness is higher and ranges from tens of nanometers to hundreds nanometer. This decreases drastically the usability for microfluidic application. Nevertheless, different post-processing approaches have been tested to avoid this problem. Promising results have been obtained with heat treatments, CO₂ laser reflow and oven annealing, which allow to reduce the roughness down to few nanometers [71].

3.4. Laser writing Set-up

The femtosecond laser writing process of the glass suspended microchannel resonators (SMRs) was accomplish with the fully integrated 3D printer f100 Head system. The laser used for the processing of the devices was a 1030 nm Ytterbium laser fiber, focused with a 50X objective (NA 0.65). The writing system (Figure 3.3) is regulated thanks to CAD-CAM software, which allows to transform the device design, opportunely drawn in DXF or STL format, into the physical prototype.

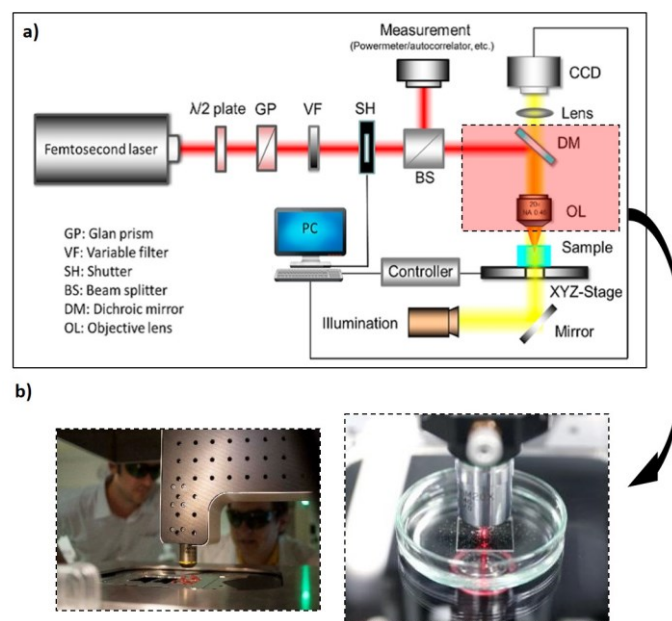


Figure 3.3 Femtosecond laser direct writing system, a) schematic configuration of a general writing system (from He et al. 2014 doi:10.3390/s141019402), b) images of the Femtoprint® writing head.

The femtosecond laser set-up is generally composed by a combination of a $\lambda/2$ plate and a Glan prism that are used to adjust the laser power. A more precise tuning of this parameter can be accomplished by variable neutral density filter. Another

important parameter that has to be controlled during the process is the exposure time: generally controlled by the means of a mechanical shutter. The stability of the input laser power is monitored splitting the input beam into two. One is the reference beam and the second split beam is send through a microscope objective and focused in a small working area.

During the fabrication process, the laser pattern is written inside the glass moving the sample holder thanks to high-precision XYZ stage. In order to monitor the writing procedure a dichroic mirror and a charge-coupled device camera are used, the writing patter results clearly visible due to the change of the refractive index.

3.5. SMRs design

3.5.1. Double clamped beam

The SMRs here presented is a double clamped beam with a microchannel embedded in the bulk material. The fluidic connections are one inlet and one outlet directly in contact with the buried microchannel, as shown in Figure 3.4. The total length of the channel ranges between 1.8 and 2 mm, with a total volume between 565 and 628 pL, the suspended segment of the microchannel has a variable length and volume. In fact, the bridge was design with different dimensions (length and width), keeping constant the beam high equal to 30 μm . The dimensions have been chosen following one important constraint: the minimum diameter of interaction (d_{min}) at the laser focal point. Working with a 50X objective this value is 8 μm and imposes the minimum channel dimension. The diameter of interaction was defined experimentally as the sum of the modified glass spot diameter (d_{wr}), observable immediately after the writing process and the broadening (Δ_{KOH}) due to the KOH etching (2 μm)

$$d_{min} = d_{wr} + \Delta_{KOH} \quad (3.1)$$

The broadening is mainly caused by a border effect due to the isotropic diffusion of the heat out of the focal volume. Considering an high-repetition rate process the

heat does not spread out the substrate but is confined in the proximal area, which subsequently can undergo to KOH etching.

In principles the volume of interaction can be further optimized tuning the energy per pulse, however this parameter influence also the efficiency of the KOH etching after the laser exposure. It was observed that lowering the energy value below a certain value can ensure a smaller volume of interaction but the glass modification results inefficient in terms of KOH susceptibility. Considering this constrains and working in the optimal condition of magnification, numerical aperture (NA) and energy/pulse, the beam thickness limit was set at 30 μm (as minimum achievable) and the minimum channel diameter was set at 10 μm .

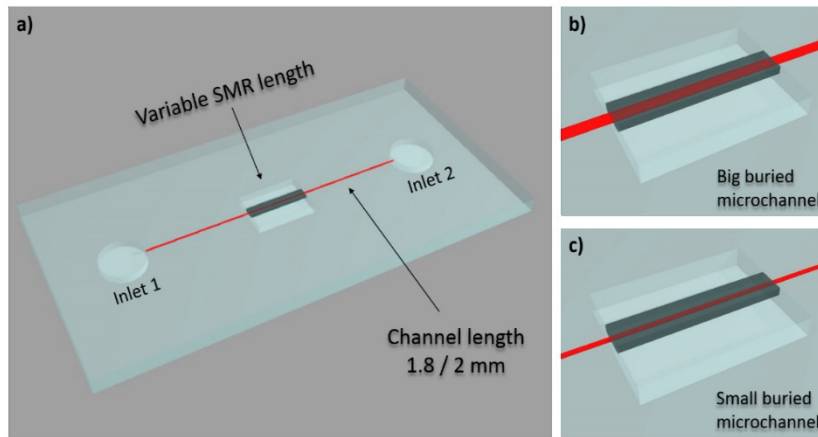


Figure 3.4 Schematic illustration of the glass SMRs design. a) Clamped clamped beam and embedded channel chip, b)-c) detail of the suspended bridge with a big and small-buried microchannel respectively.

The ratio between thickness, width and length has been chosen to avoid mixed in-plane and out-of-plane modes. Five different lengths (250 – 450 – 500 – 700 – 750 – 1000 μm) and different beam width (50 – 70 – 75 – 90 μm) have been tested. In order to investigate the effect of the viscous damping due to the squeezing of air under the beam, four different gap conditions have been tested. For 450 μm long beam, the gap was design 20, 100, 200 μm high, and compared to gap free beam.

The liquid to solid ratio is an important parameter to increase the resonator performance. Unfortunately, the beam height has to be keep constant but in order to increase the liquid to solid ratio we varied the ratio between the width of the buried channel and the beam. In particular, for 50 μm width beam the microchannel was design with a round (10x10 μm) and rectangular (10x30 μm) geometry. The same designs were tested for 75 μm width beam, with a small variation of the dimensions

of the rectangular geometry ($10 \times 55 \mu\text{m}$). The micrometric dimensions of the buried channel are compatible with the flow through of micrometer-sized analytes, such as particles, mammalian cells, yeasts or bacteria.

The clamping corners of the beam have been design with a rounded shape in order to avoid residual stress after the release of the suspended structure.

3.6. SMRs fabrication procedures

The different SMR designs were fabricated using fused silica as substrate. This glass was preferred to other type of glasses because of the high grade of purity that ensure superior optical and thermal properties. In fact, compared to other transparent materials, fused silica shows several advantages, first it is able to maintain a high optical transparency for a broad band of wavelengths, down to the UV range, and it is characterized by a very low fluorescence background. Furthermore, fused silica glass is commonly used in standard microfabrication processes, like photolithography and etching, thus enabling to couple the femtosecond writing with other processes for the integration of electronic components or other post-process modifications. The choice of fused silica is particularly suitable for many applications in the biosensing field, in particular it is chemically inert (biocompatible), hydrophilic, “nonporous”, stable in time, optically clear and it is compatible with electro-osmotic flow. From the chemical point of view, it can be easily modified in order to increase the bio-affinity to certain molecules or biological agents.

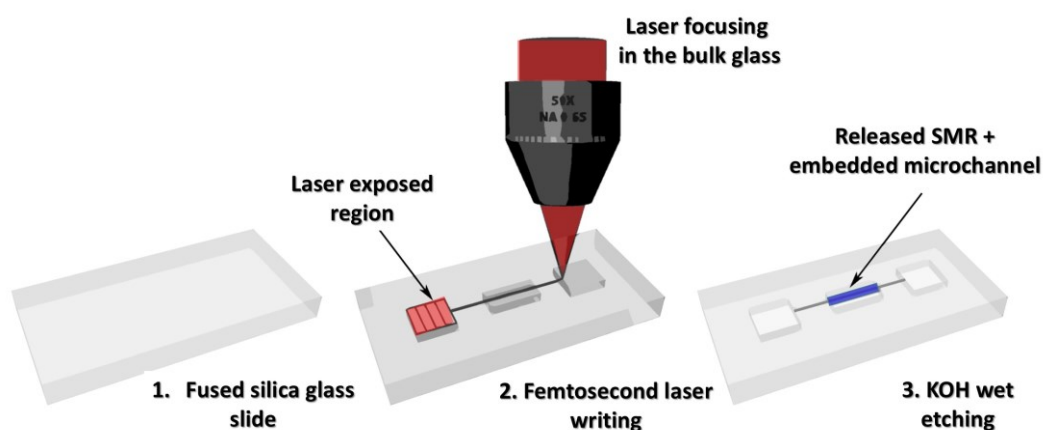


Figure 3.5 Schematic illustration of the femtosecond laser patterning, the writing process is highlight in red and the suspended microchannel resonator release after KOH etching is highlight in blue.

The glass suspended microchannel resonators were realized with the collaboration of Femtoprint®, which followed the optimization of the fabrication parameters. The fabrication process [95] (Figure 3.5) consists on the modification of a 0.5 mm thick fused silica substrate using a 1030 nm femtosecond pulsed laser (Ytterbium fiber). The SMR structure and the buried channel were patterned by moving the glass slide with respect to the focal spot of the laser, working with a single-path transverse write method. The focal volume exposed each time to the laser was around $523 \mu\text{m}^3$, the minimum achievable using a 50X objective with 0.65 NA. During the fabrication process, the usage of 50X and 20X objectives were compared in order to understand how this can affect the final beam structure. In particular, the use of different objective magnification was useful to investigate the minimum beam thickness, the channel dimensions achievable and the stress induced with this fabrication process. The 50X and 20X objective show distinct volumes of interaction with the fused silica substrate (Figure 3.6). In particular, working with 50X objective means higher numerical aperture and lower field of view, which can improve the axial resolution of the laser spot defining a spherical volume of interaction. In contrast, the 20X shows a lower numerical aperture that means higher asymmetry of the laser spot with lower energy density and higher spatial distribution of the volume of interaction. These conditions, promote the formation of an elliptical spot (Figure 3.6b-c), which can show different dimensions as function of the energy/pulse used. In fact, decreasing the energy it has been possible to obtain a narrow channel, but with an extremely elongated shape (Figure 3.6b). For the 20X objective a process with higher energy was preferred in order to limit this phenomenon and to promote the fabrication of beam with thickness within $35 \mu\text{m}$. Independently to the objective used, at the focal point, the energy absorbed by non-linear mechanism changes the local density of the fused silica, modifying the chemical susceptibility to wet etching reagents. So that, after the exposure the patterned silica substrates were immersed in highly concentrated KOH solution (for 8 hours): the exposed regions are dissolved with an etching rate 200 times higher in comparison to the pristine glass. The use of KOH brings significant advantages, compared to HF etching. In fact, this process is less affected by three main limitations: maximum length achievable, shape and aspect ratio of the buried channel. Indeed, KOH shows higher etching selectivity of laser exposed glass with respect to HF etching, this results useful in order to maintain the

channel dimensions constant along the beam length and to maintain the channel diameter as near as possible to that of the focal point of the laser. Actually, after the KOH etching the central part of the channel shows dimensions approximately equal to those of the laser illumination. In fact, even if the center is the last portion reached by the etching solution, and the openings are the parts of the channel that remain in contact for the entire duration of the etching bath, the difference in diameter is less than $2\ \mu\text{m}$. Exploiting the removal of the laser exposed material by KOH, it has been possible to realize the microchannel patterning with a single laser scanning line, avoiding the typical conical shape characteristic of HF etching procedures that required more complex fabrication process to obtain the same result. Furthermore, the typical length saturation, that causes the reduction of the permeability along the beam length, was not observed for KOH etching. The etching selectivity results independent from the etching time, making possible prolonged etching essential to obtain long channel (2 mm) with an aspect ratio of almost 200 (between length and width).

The microchannel inside the suspended beam have to be as small as possible, in fact this influences the thickness of the beam itself, which is crucial for the device performance. Considering that the laser spot size define the minimum diameter achievable ($10\ \mu\text{m}$), the higher selectivity shown by KOH enabled to maintain a good tolerance between the pattern and the channel dimensions even after the wet etching process, allowing to keep the beam walls as thinner as possible.

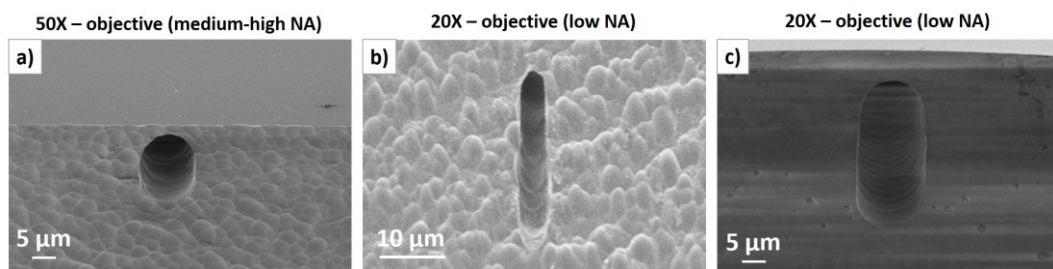


Figure 3.6 SEM images of the microchannel inlet, which show different channel shape and dimension. a) A totally spherical channel was obtained working with a 50X objective (medium-high NA), in contrast b) an elliptical channel was obtained working with a 20X objective (low NA), varying the energy/pulse the minimum channel diameter was modify.

Since the non-linear absorption takes place only at the focal point, the laser can penetrate the bulk material, enabling to center the patterning of the buried channel in the middle of the suspended structure, with a good Z-tolerance. The top surface

of the suspended beam correspond to top surface of the fused silica wafer, this strategy was preferred in order to conserve a “good” reflectance of the surface. This characteristic is fundamental for the mechanical characterization that we will see in the following chapters, was performed with an interferometric system.

The Femtroprint® fabrication process allowed to reach a resolution $< 1\ \mu\text{m}$, a XY tolerance of $\pm 1\ \mu\text{m}$, a Z tolerance of $\pm 2\ \mu\text{m}$ during the alignment and a position accuracy of $0.5\ \mu\text{m}$. After the laser writing the treated surfaces shown a roughness $< 100\ \text{nm}$ (Figure 3.6.). Eventually, the roughness can be further diminish, below $10\ \text{nm}$, using a specific polishing process.

The laser condition plays a key role during the femtosecond laser processing, in particular the spatiotemporal beam profile, polarization, repetition and scanning rate can affect the final shape of the exposed region. Tuning these parameters, it has been possible to obtain an almost round channel (Figure 3.7d) without re-deposition of fused silica or not correctly exposed materials (Figure 3.7a–b–c.).

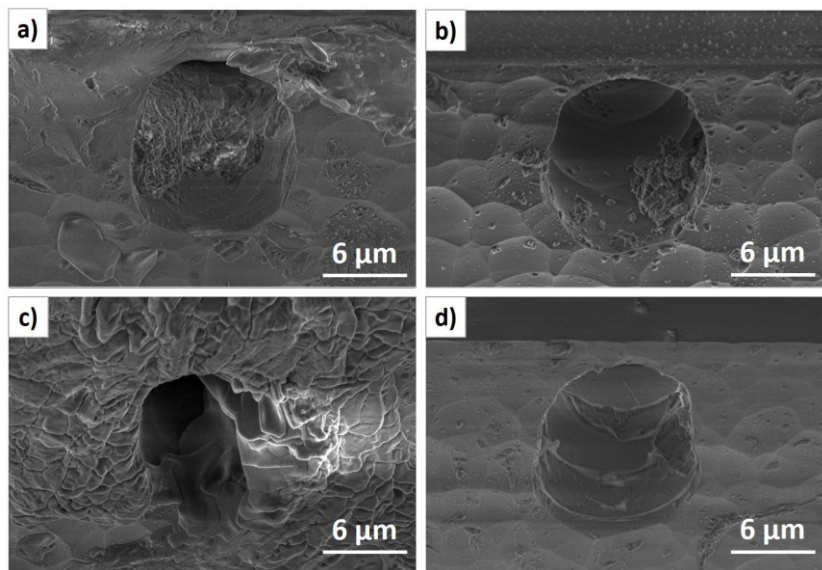


Figure 3.7 SEM images of the possible fused silica damage that can occur during the laser writing process, a)–b) fused silica re-deposition, c) modification of the channel surrounding and d) high roughness of the inner walls surfaces.

Furthermore, from the SEM characterization of the SMRs, it is possible to appreciate also the different channel dimensions. In Figure 3.8 are reported the channels obtained after the laser patterning. In this case, the laser was focalized with a 20X objective. Working in these conditions the minimum channel dimensions are $30\ \mu\text{m}$ (height) and $14\ \mu\text{m}$ (width) and the channel shows an almost elliptical shape.

The laser spot dimensions defines the minimum high of the channel, but the width can be further tuned, obtaining channel with square or rectangular shapes.

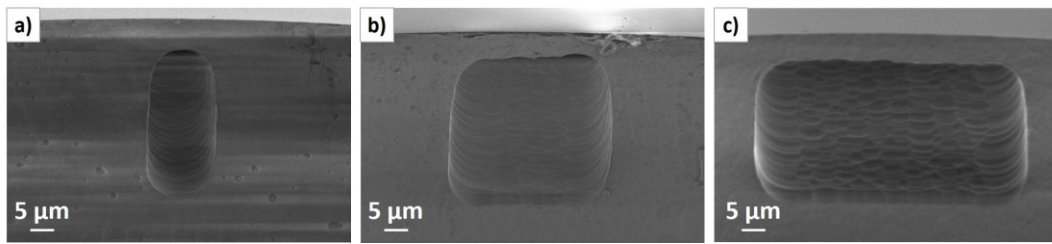


Figure 3.8 SEM images of channel inlet obtained with a 20X objective, a)–b)–c) represent the three different channel width, which were designed to evaluate the impact of the channel volume on the mechanical properties of the SMR.

The different depth of the gap under the suspended bridge can be observed from the SEM images below (Figure 3.9). In the following chapter, it will be deeply describe the influence of the different beam and channel dimensions on the mechanical properties and it will be analyze how the channel gap could influence the vibrational motion of the suspended structure.

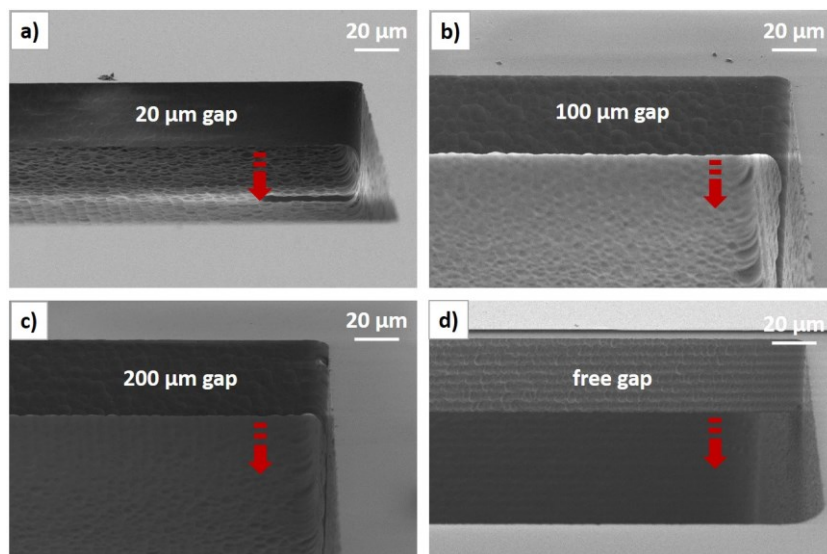


Figure 3.9 SEM images of the gap under the SMRs. Four different gap configuration has been (20–100–200 μm and free gap) designed to evaluate the viscous damping impact. In particular, 20 – 100 – 200 μm and free gap has been fabricated (a–b–c–d respectively).

3.7. SMRs morphological analysis

In order to evaluate the effectiveness of the fabrication process and to verify that the embedded channel was properly buried, an interferometric reconstruction of the

glass surface was performed. Exploiting the differential interference between the flat and defected surfaces has been possible to detect easily the presence of holes. Indeed, due to a non-homogeneous alignment of the laser along the Z-axis, some of the samples could present only partial buried channel. As can be observed from the Figure 3.10, comparing the interferometric response of flat and damaged surface, the holes present along the channel pattern show a different contrast (Figure 3.10c). This difference is not appreciable by the images captured by the optical microscope (Figure 3.10b-d), in fact in this case the completely and partial buried channel show the same optical features.

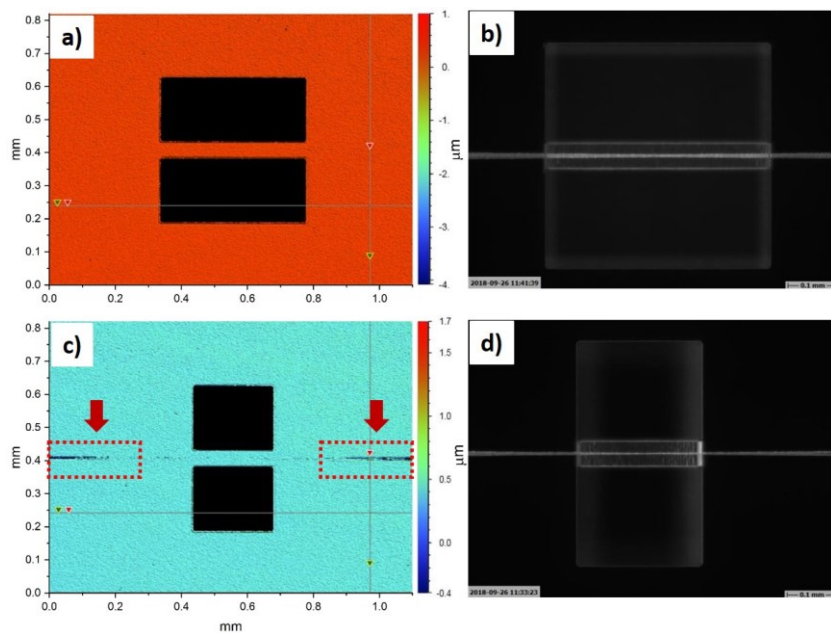


Figure 3.10 Morphological analysis of the SMRs, a-c) are the interferometric response for an intact and damaged surface, respectively, b-d) optical images of the same samples where the presence of the damage is clearly not appreciable.

A second method that has been used to evaluate these defects is the scanning electron microscopy. From Figure 3.11 the defects are easily detectable, and the hypothesis of a miss-alignment along the Z-axis during the fabrication process is confirmed. Both the characterizations were performed for all the new samples fabricated in order to understand the correlation between the fabrication parameters and the presence of defect along the channel pattern.

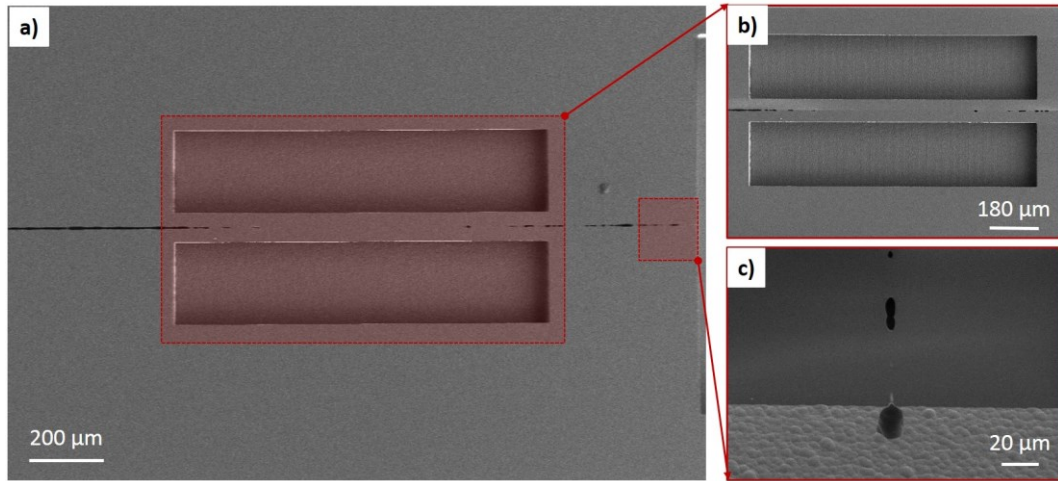


Figure 3.11 SEM images of the SMRs, a) from the picture is clearly visible the presence of some superficial damage due to the wrong Z-alignment of the femtosecond laser during the writing process, b) detail of the SMR and relative damage along the central part of the beam, c) detail of the channel inlet where a wrong Z-alignment of the laser beam is clearly visible.

During the optimization of the fabrication process, this problem was almost totally solved introducing a surface mapping. This step allowed to define a homogeneous distribution of alignment coordinates along the wafer surface, overcoming the non-ideal flattens of the substrate.

3.8. SMRs packaging

In order to perform flow through liquid measurements, the SMR chips were integrated with a microfluidic system. A PDMS microfluidic cover, bonded to the fused silica chip via plasma oxygen, was used as standard process for the microfluidic integration.

The PDMS microfluidic system was designed to contain two bypass channels (50 x 50 μm) that precisely overlap to the inlets of the channel embedded in the SMR (Figure 3.12.). The design contains also four cross-mark to simplify the alignment process. The PDMS system was realized by means of a silicon mold fabricated with standard fabrication techniques based on silicon etching (Figure 3.12a.). A Silicon wafer (500 μm thick) was coated with 2 μm of AZ1512 photoresist with the ACS 200 coater (Figure 3.13a.). The photoresist was than patterned and developed respectively with the MLA 150 laser writer and ACS 200 coating and developer system (Figure 3.13b). The designed was scaled by 1.5% in order to compensate the PDMS shrinkage after the polymerization.

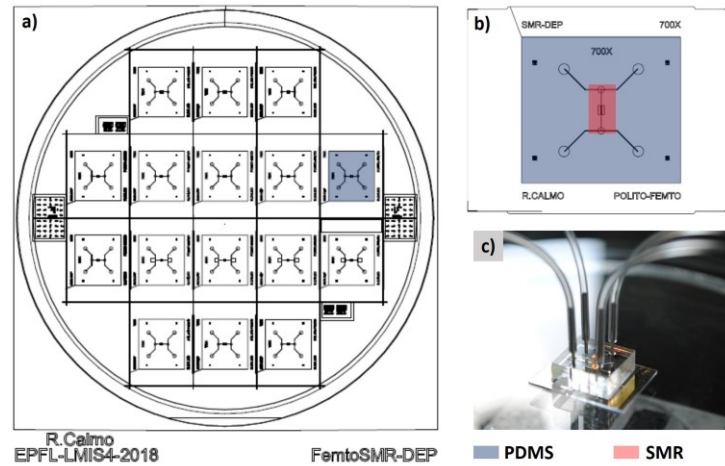


Figure 3.12 PDMS microfluidic interface, a–b) silicon mold design and the detail of the PDMS fluidic (in grey) overlap to the SMR structure (in red), c) SMR chip bonded to the PDMS fluidic interface.

The top silicon not protected by the photoresist was etched with the Adixen AMS200 Deep Reactive Ion Etching (DRIE) etcher from Alcatel Micro Machining Systems, obtaining the reverse fluidic channels (50 μm high) (Figure 3.13d). The resist was then stripped from the wafer, and the silicon surface was silanized with Trichloro(1H,1H,2H,2H-perfluorooctyl)silane (PFOTS) (Figure 3.13f). The as obtained Silicon mold was then utilized to prepare the PDMS microfluidic cover (10:1 polymer/ cross-linker ratio) with a thickness of 0.5 mm.

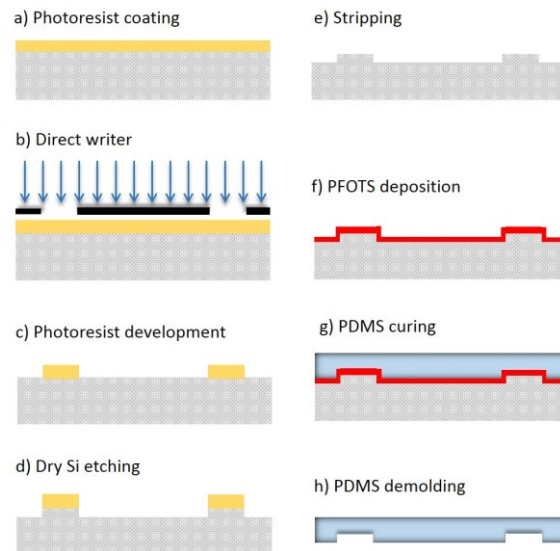


Figure 3.13 Silicon mold fabrication and PDMS fluidic release: the process flow, for the mold realization consist of five different step that concern the photoresist coating (a), the transferring of the fluidic pattern by laser direct writing (b), the photoresist development (which removes the non-exposed photoresist) (c), the dry etching of the unprotected silicon surfaces (d), which allows to transfer the fluidic pattern on the silicon wafer and the final photoresist stripping (e). Once the mold is fabricated, the silicon surface have to be passivated by a PFOTS (f) deposition that is essential to ensure the PDMS de-molding after the polymerization (g–h).

3.8.1. PDMS bonding process

The PDMS–fused silica bonding was performed using the Oxygen Plasma activation. The chamber pressure, RF power, and exposure time were optimized in order to obtain the maximum strength of the bonding. The pressure in the chamber has been varied setting the oxygen flow in the range 20–70 SCCM, with the injection valve opened at 100% or 50%. In order to evaluate the variation of these parameters on the bonding effectiveness, PDMS and fused silica were exposed to the same plasma condition and a peeling test was performed. Furthermore, the PDMS surface activation was evaluated by means of contact angle (CA) measurements as function of the changed parameter. The drop images acquired to evaluate the CA were post-processed with the function Drop–Snake of the software ImageJ.

The first test for the bonding optimization concerned the tuning of the chamber pressure, ranging from 171 mTorr to 528 mTorr. The RF power and the time of exposure were respectively fixed at 20 W and 30 sec. The average contact angles as function of the chamber pressure are reported in Figure 3.14. Considering the values and the associated standard deviations (each measurement was repeated six times) there is no remarkable variation due to the pressure change, nevertheless 364 mTorr was selected as the optimal condition for the next optimization test.

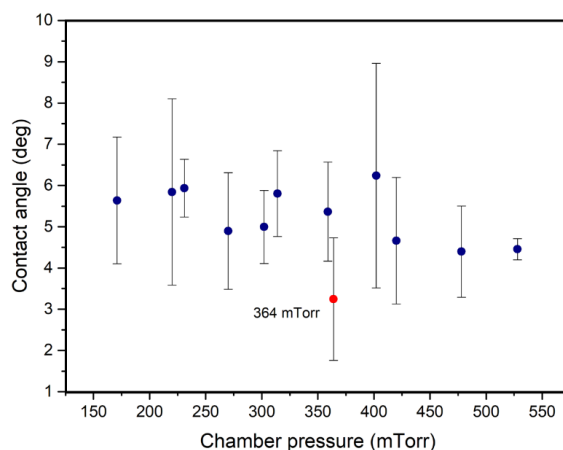


Figure 3.14 Chamber pressure optimization. The best condition (red dot) was selected evaluating the variation of the water contact angle as function of chamber pressure, keeping constant the RF power and the exposure time.

In the second set of measurements was analyzed the influence of the RF power variation in the range of 20–60 W. The chamber pressure and exposure time were kept constant (364 mTorr and 30 sec). In Figure 3.15 is reported the contact angle

distribution as function of the RF power, as expected for high power level the contact angle increase. For RF power superior than 20 W the ion bombardment is slightly reducing the surface activation. However, the values remain below 10° that is the threshold to evaluate the effectiveness of the process.

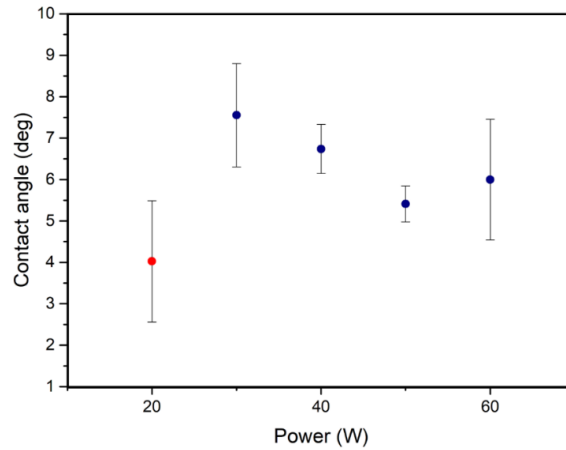


Figure 3.15 RF power optimization. The best condition (red dot) was selected evaluating the variation of the water contact angle as function of power applied, keeping constant the chamber pressure and the exposure time.

The last set of optimization concerned the exposure time (from 10 to 60 sec), the best result for RF power and chamber pressure deriving from the previous sets of optimization were used as fixed parameters. From the Figure 3.16 it is possible to notice that for exposure time higher than 10 sec the contact angle decrease under 10° , with an apparent minimum at 40 sec. Afterwards, a peeling test was performed, the bond strength for the different exposure time was considered effective, except for 10 sec exposure.

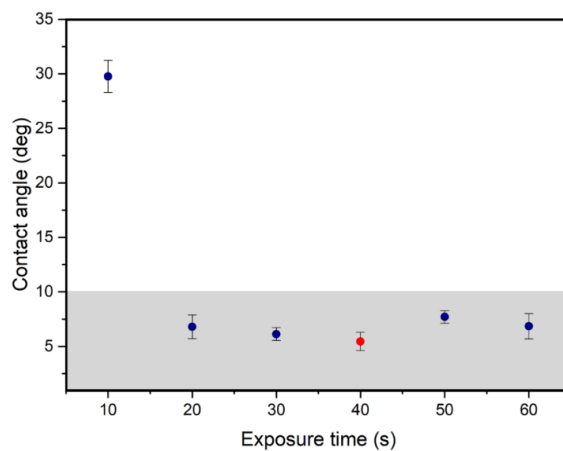


Figure 3.16 Exposure time optimization. The best condition (red dot) was selected evaluating the variation of the water contact angle as function of exposure time, keeping constant the RF power and the chamber pressure.

The optimized values of chamber pressure, RF power and exposure time were used to perform an aging test (Figure 3.17). The contact angle as function of time shows a logarithmic growth that gradually stabilizes to the value of 55°. For times above 5 minutes, the contact angle increases over 10° and the surface activation effectiveness start to decrease. Nevertheless, 5 minutes is a duration time long enough to perform correctly the alignment procedure between the PDMS cover and the fused silica resonator chip.

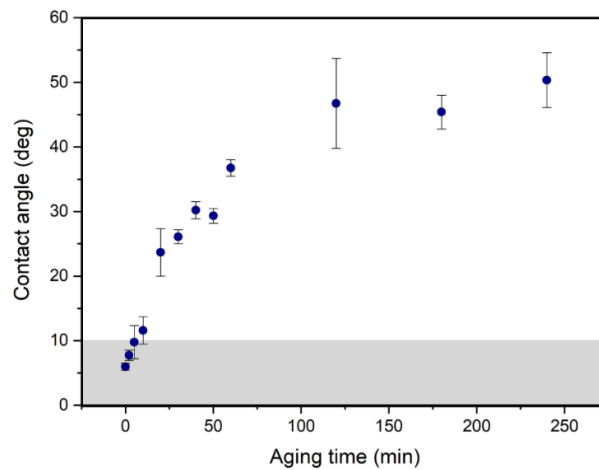


Figure 3.17 Aging test. The PDMS surface, activated with the best exposure parameters (RF power, chamber pressure and exposure time), were aged for different time in order to evaluate the strength of the PDMS–glass bonding even if the contact between the two material takes place after a variable amount of time.

Chapter 4

Mechanical characterization and validation

4.1. Introduction

In order to deeply characterize the mechanical properties and the operating conditions of the glass SMRs, two different systems were used: a Laser Doppler Vibrometer and a lock-in/Phase-Locked Loop (PLL) analyser. The first system was used to measure the resonance frequency spectrum of each SMR and to analyse the frequency response due to the filling of the channel with different liquids. The Lock-in/PLL amplifier was used to analyse the output signal, thanks to the possibility to perform a sweep and the direct monitoring of the frequency oscillation over time. In this case, the optical system and the output signal are managed by the Laser Doppler Vibrometer. Furthermore, the two systems were used to analyse in two different way the Q factor of the different SMRs. In particular, the Lock-in/PLL analyser was used for the ring-down measurements.

4.2. Measurement Set-up

4.2.1. Laser Doppler Vibrometer

The Vibrometer system was used to control both the actuation and detection system for the SMR analysis. The laser Doppler Vibrometer used in this work was a Micro-System-Analyser MSA500 from Polytec (Figure 4.1a). The working principle of the integrated detection system is based on optical interference: the laser beam emitted from a source is split in two coherent beams with respective intensity I_2 and I_1 (Figure 4.1b). The first is used as probe of the sample vibration and the second as reference beam. The total intensity of the beams is modulated taking into account the “interference” term:

$$I_{tot} = I_1 + I_2 + 2\sqrt{I_1 I_2} \cos[2\pi(r_1 - r_2)/\lambda] \quad (4.1)$$

where r_2 and r_1 are respectively the optical path of the reference and working beam. When the sample vibrates, the frequency of reflected beam shifts depending on the moving velocity of the sample, according to the Doppler effect. The frequency variation can be described according to the formula:

$$\Delta f_D = 2 \cdot v/\lambda \quad (4.2)$$

where v is the object’s velocity and λ is the wave length of the incident beam.

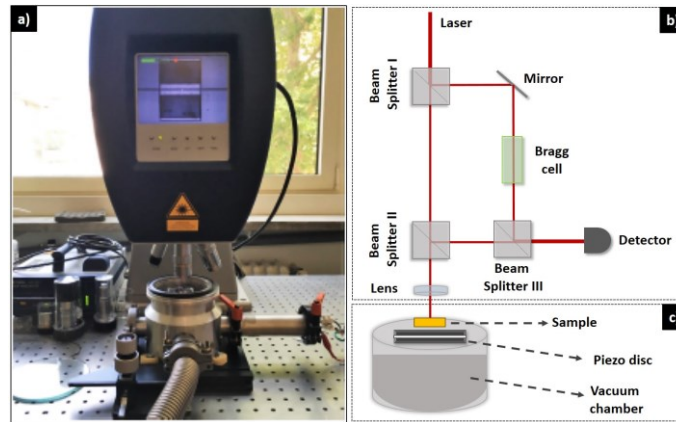


Figure 4.1 Laser Doppler Vibrometer: experimental set-up. a) The head of the Laser Doppler Vibrometer and the vacuum chamber used for the mechanical characterization of the SMRs; b) schematic representation of the interferometric system; c) schematic representation of the vacuum chamber and the external actuation system.

The reference beam follows an optical path constant over time ($r_2 = \text{constant}$), eventual thermal effects are negligible. On the contrary the vibration of the sample makes the path of the probe beam variable as function of time, $r_1=r(t)$. The interference between the two beams generate a light/dark pattern varying in time that reach the detector. The generated interferometer pattern is then converted by the detector in a voltage signal proportional to the velocity of the sample.

The Micro-System-Analyser integrates a signal generator for the actuation of the piezo disc, used to put in vibration the samples fixed on top of it by means of a conductive tape. The piezo disc is inserted in a vacuum chamber, which can be evacuated by a membrane and a turbomolecular pumps (MINI-Task System, Varian Inc. Vacuum Technologies) up to a vacuum level of $2 \cdot 10^{-7}$ mbar. (Figure 4.1c).

4.2.2. Lock-in and PLL

The measurement of the frequency stability and ring-down analysis were performed using a HF2LI/PLL system (Figure 4.2), purchased from Zurich Instrument. The lock-in analyser was used to directly actuate the piezo disc and to collect the output signal from the Vibrometer system.

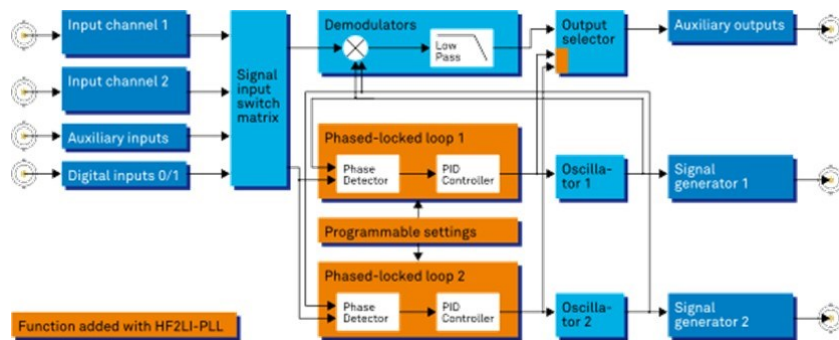


Figure 4.2 Schematic representation of the Lock-in and Phase-Lock-Loop system, image from the Zurich instrument website (HF2LI/PLL system).

The lock-in allowed to perform a frequency sweep and to measure the amplitude and phase of the vibration of the sample as function of the frequency. The resonance frequency can be easily isolated thanks to the amplification respect other frequency components. This amplification is possible through a dual-phase demodulation. The Phase-locked loop component results particular important to perform the frequency tracking in a very short period of time. The PLL uses the phase difference between two signals to control the frequency of the loop. The typical PLL configuration is

characterized by a frequency generator from which an output signal is generated and subsequently splitted in two arms. The measurement arm is used to analyse the mechanical platform under study and depending on the device solicitation (change of strain, mass, etc..) can undergo a phase shift. The reference arm is used to set the phase to a specific set point and when compared with the measurement arm allows to estimate the difference between the signals. This difference is than used as input to the loop gain element and to calculate the shift from the frequency output.

4.3. Frequency characterization

The mechanical properties of the different SMRs were characterized by means of the Laser Doppler Vibrometer. In order to understand the behaviour of the glass SMRs, a vibrational spectrum was recorded up to 5 MHz comparing the observable resonance modes in air and in vacuum. The limit of 5 MHz was chosen as measurement range, but can be in principle extended in order to investigate higher resonance modes. Nevertheless, the high frequency resonance modes show a limited signal amplitude, which results hardly discernible form the background noise for in air measurement. In Figure 4.3 are reported the vibration spectra for the 500 L x 75 W x 30 H μm SMR with an embedded channel of approximately 10 x 10 μm , fabricated using a 50X objective. As expected, the resonance peaks are sharper and the noise floor is reduced when the mechanical characterization was performed in vacuum compared to those in air. The resonance frequency and the quality factors, associated to the different vibrational modes, are reported for each of the investigated modes. In Figure 4.3 the variation of the Q factor between air and vacuum measurements is also clearly visible. The Q factor was calculated taking in to account the ratio between the resonance frequency and the frequency bandwidth at -3dB, both computed by a Lorentz fit that is reported for each frequency peak (blue fitting curve). The frequency characterization (up to 5 MHz) enabled the visualization of four flexural and two torsional modes. For each of them the graphical reconstruction of the vibrational mode is reported (Figure 4.3), which was obtained from the direct analysis of a scan-grid measurement. In fact, this approach allowed to obtain the frequency spectrum from different scan-points along the resonant structure, creating a map of the vibrational behaviour of the whole SMR. This measurement allows to easily associate each resonance peak with the correspondent vibrational mode.

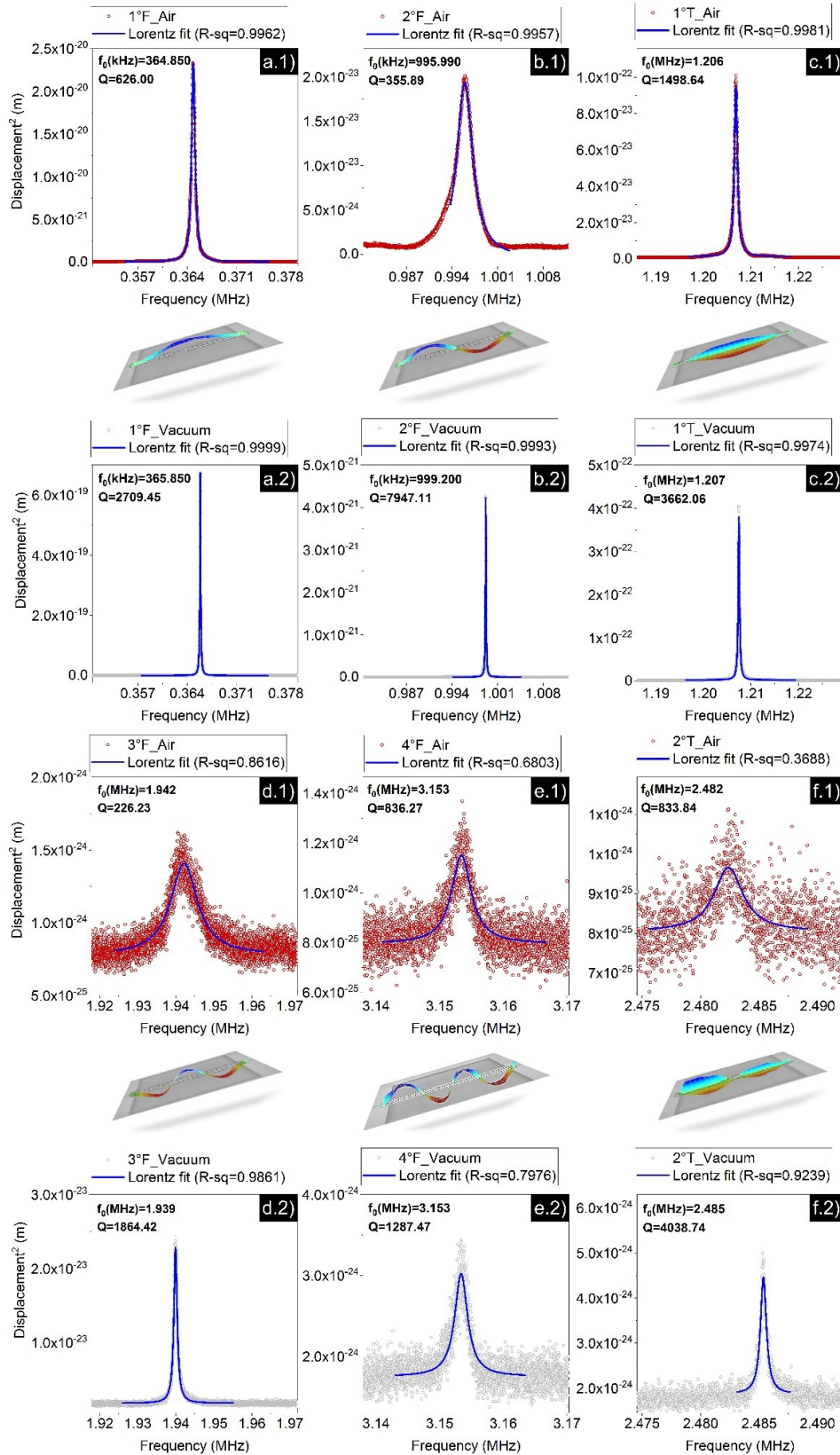


Figure 4.3 Example of a mechanical characterization of an SMR. Six different resonance modes for air (red line) and vacuum (grey line) measurement are reported, each of them is associated to relative the mode shape reconstruction.

For all the fabricated SMRs (showing different dimensions) at least the first vibrational mode has been recorded and analysed. The corresponding resonance values, dimensions and mass are reported in Appendix B.

4.4. Quality factor characterization

In order to better understand the influence of the dimensions of the SMR, the Q factors of the different samples were analysed and compared. In particular, it is important to remember that the change in the magnification of the objective, used for the SMR fabrication, can affect the minimum thickness of the beam and the minimum dimension of the channel. For this reason, the distribution of the Q factor was analysed as function of both the beam dimension and the empty volume ratio (V_c/V_b = volume channel/volume beam).

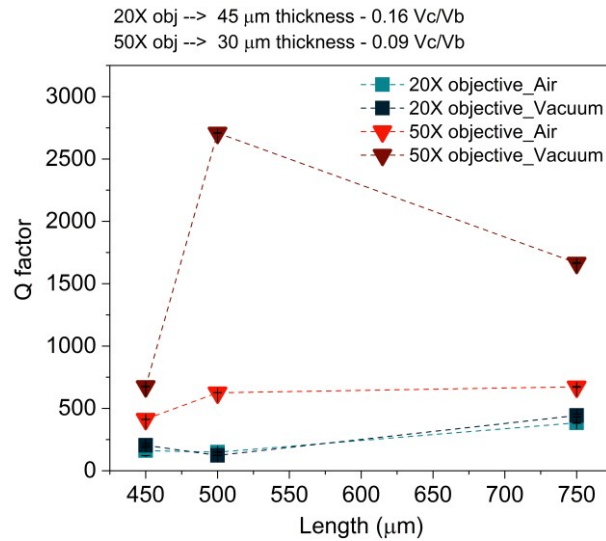


Figure 4.4 Q factor variation as function of the SMR length. Q factor values associated to different SMR length, the 20X and 50X-based fabrication are compared. Each SMR was characterized in air and in vacuum environment in order to evaluate the Q factor variation as function of the surrounding media.

In Figure 4.4 it is possible to observe the Q factors distribution as a function of the length of the beams fabricated with the two different objectives. From a first analysis, it seems that for the SMRs fabricated with the 20X objective, the Q factor is smaller than the one fabricated with the 50X objective. In fact, two different phenomena occur using high magnification objective: the reduction of the minimum beam thickness achievable and a different induced strain contribution. These can partially

contribute to the enhancement of the Q factor for the samples fabricated with the 50X objective respect the ones fabricated with the 20X objective.

Considering the possibility to obtain different embedded channel dimensions a second analysis of the Q factor variation was taken into account. From the graphs in Figure 4.5 it is possible to observe the Q factor variations as function of the beam length, with a variable V_c/V_b ratio. Comparing beams with the same dimensions, but with different V_c/V_b ratio, the channel dimension seems to affect the Q factor, especially for the 450 μm long SMRs (Figure 4.5a). In this case, the SMRs that exhibit a higher V_c/V_b ratio show also the highest Q factor. The relative variation of this parameter, between air and vacuum characterization, seems to be higher for the 450 μm long and 75 μm wide SMRs (Figure 4.5a). This trend results completely inverted observing the Q factor for the 45 μm wide beam (Figure 4.5b), where the highest increment was shown from the 750 μm long beam. The overall Q factors variation (air to vacuum) seem to be less marked if compared to the variation observed for the SMRs fabricated by the 50X objective (Figure 4.4).

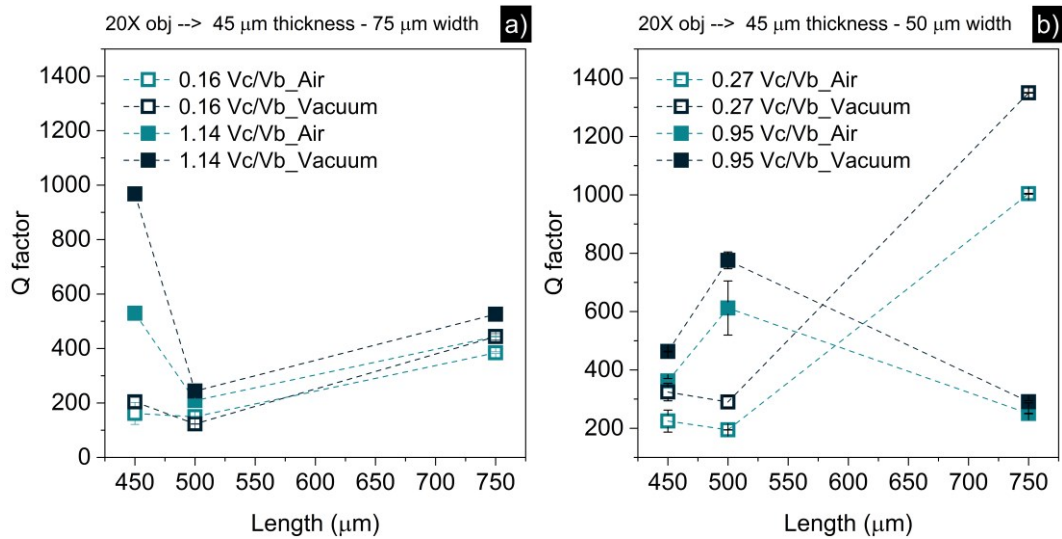


Figure 4.5 Evaluation of the width impact on the Q factor. SMRs with same length and thickness, but with different width, have been characterized in air and in vacuum and compared; a-b) in the graph the Q factor for 75 and 50 μm wide SMRs are reported, respectively; for each device is specified the ratio between the channel and the bulk volume (V_c/V_b).

From a general point of view, the major influence over the Q factor variation seems to be directly linked to the objective used for the fabrication and thus to the V_c/V_b ratio and thickness of the beam that can be obtained. Furthermore, the thickness

seems to affect in a minor way the variation of this parameter, even if the V_c/V_b trend as a function of the beam length results to be not completely clear.

A second element that could influence the performance of the SMR is the dimension of the gap under the beam, which can be a source of squeeze damping. Four different gap were designed, 20 μm – 100 μm – 200 μm and free gap (hole-through). The influence of the gap height was analysed evaluating the Q factor and trying to understand if a small gap can contribute negatively, increasing the squeeze damping and thus reducing the Q value.

As it is possible to observe from the Table 4.1, for each gap condition the Q factor values were analysed. In order to better understand the influence of this parameter, the Q factor was computed for both in air and in vacuum measurements and for two different SMR designs (450L x 50W x 45H and 450L x 75W x 45H). The Q factors vary between 200 and 350, but no clear correlation between the gap depth was found.

<i>Sample (beam width – gap config.)</i>	<i>Q factor (Air)</i>	<i>Q factor (Vacuum)</i>
<i>50–20 (μm)</i>	285.34 ± 17.60	403.62 ± 30.21
<i>50–100 (μm)</i>	329.64 ± 19.25	322.39 ± 14.44
<i>50–200 (μm)</i>	254.23 ± 45.88	293.52 ± 32.15
<i>50–free gap</i>	224.68 ± 37.67	324.22 ± 1.49
<i>75–20 (μm)</i>	199.13 ± 18.75	272.32 ± 7.06
<i>75–100 (μm)</i>	373.98 ± 13.07	360.68 ± 7.93
<i>75–200 (μm)</i>	298.69 ± 5.88	270.08 ± 1.00
<i>75–free gap</i>	161.75 ± 40.35	203.91 ± 16.42

Table 4.1 Q factor variation as function of the gap configuration, tested for two beam classes characterized by different width: 50 μm and 75 μm .

The variation of the SMR width (50 and 75 μm) seems to affect partially the overall behaviour of the Q factor. In both cases, the Q factor fluctuations are not completely proportional to the gap height. Observing the experimental data it has been hypothesized that the main contribution to the Q value is probably due to some fabrication defects (i.e. induced stress) or to the clamping losses phenomenon (also considering the results obtained from the vacuum characterization). As stated in Chapter 2, the Q factor is the sum of different energy dissipation contributions that can derive from the interaction with the surrounding medium (liquid or gas), from the clamping of the beam to the substrate or from the intrinsic mechanisms of dissipation (i.e. material friction, thermoelastic losses or phonon–phonon interaction losses).

For the analysed SMRs, the medium–interaction losses can be approximated taking into account the gas environment contribution, where the dominant damping mechanisms can be describe by the pure fluidic regime. This assumption it has been confirmed by the evaluation Knudsen number (K_n)

$$K_n = \frac{\lambda_f}{L_r} \quad (4.1)$$

where λ_f is the mean free path length of the gas and L_r represents the significant length scale of the mechanical structure. Two of the most common damping sources have been considered: the *squeezed–film damping* and the *drag–force damping*. The first contribution describe how the proximity of the suspended beam to the underlying substrate can affect its vibration and the quality factor (Q_s). In particular, the gas molecules trapped in this physical space can act as damping source, reducing the final Q of the resonator. On the contrary, when the beam is sufficiently far away from the substrate, the source of damping is represented by the collisions of the surroundings gas molecules with the beam surfaces, *drag–force damping* (Q_d). The length scale (L_r) is set equal to the gap depth (20–200 μm) for the *squeezed–film damping*, and equal to the beam width for the *drag–force damping*. Considering the air at atmospheric pressure, the $\lambda_f \approx 70 \text{ nm}$ and subsequently $K_n < 1$, confirming as dominant bending mechanism the fluidic regime. In this perspective, the two bending contribution can be describe as follow

$$Q_s = \frac{\rho h d_g^3}{\mu w^2} \omega \quad (4.2)$$

$$Q_d = \frac{\rho w h}{8\mu} \omega \quad (4.3)$$

where Q_s and Q_d are respectively the approximation of the quality factor due to the *squeezed–film* and *drag–force damping*, which have a dependency on the density (ρ), viscosity (μ), beam thickness (h), beam width (w), gap depth (d) and to the angular frequency (ω). As it is possible to observe from Table 4.2, these damping forces produce a small impact on the final Q. For the SMR with a gap of 20 μm (independently from the beam width) the *squeezed–film damping* shows a higher

contribution respect to the *drag-force damping*. In this case, it is evident how a gap height of 20 μm is probably the limit above which the gas damping is mainly governed by the drag-force contribution instead of the squeezed-film. In order to define the damping components with higher impact on the Q, the contribution of the clamping was evaluate. The attachment loss is mainly caused by dissipation of vibrational energy through the anchor point between the resonator and the substrate. The vibration of the beam, at frequency f , produces a shear wave with wavelength

$$\lambda_b = \frac{c_s}{f} \quad (4.4)$$

where c_s is the speed of the shear waves propagating through the solids (dependent on the Young's modulus and on the density of the substrate). If the substrate thickness (h_s) is small compared to the shear wavelength, but still greater than the thickness of the beam (h), the clamping-loss factor can be describe as

$$Q_{c-l}^{-1} = A \frac{w h^2}{L h_s^2} \quad (4.5)$$

where A is a weak function of Poisson's ratio and is equal to 3.40 if a double clamped beam geometry is considered. Observing the results obtained for the different beam dimensions analyzed (Table 4.2), the clamping factor seems to drastically affect the final Q value. The last contributions that needs to be evaluated are the intrinsic losses, focusing the attention on material friction ($Q_{friction}$) and thermoelastic losses (Q_{TED}). For the first contribution, the dissipation factor (η) can be parametrized in terms of loss tangent ($\tan \delta$) as function of the Young's modulus

$$\eta = \tan \delta = Q_{friction}^{-1} \quad (4.6)$$

For the fused silica the dissipation factor is comprise between 0.9 and $1 \cdot 10^{-5}$ and the contribution of the material friction to the final Q results comparable to that of the gas damping for the 20 μm gap. The second contribution due to the intrinsic losses is represented by the thermoelastic effect. In this case, the dissipation is due to the thermal relaxation phenomena and in particular to the presence of spatial area

with different strain-induced temperature. The contribution of this mechanism to the final Q can be modelled following the Zener's approach as Debye peaks

$$Q_{TED}^{-1} = \Delta \frac{\omega\tau}{1 + (\omega\tau)^2} \quad (4.7)$$

$$\Delta = \frac{E\alpha^2 T_0}{\rho c_p} \quad (4.8)$$

$$\tau = \frac{h^2 \rho c_p}{\pi^2 k} \quad (4.9)$$

where Δ and τ are respectively the relaxation strength and the relaxation time. As it possible to observe from the equation above, the fundamental loss contribution (Q_f) is strongly dependent on Young's modulus (E), coefficient of thermal expansion (α), temperature (T_0), density of the beam material (ρ), thermal conductivity (k) and specific heat (c_p). The Q_{TED} represents for the reported resonators (Table 4.2) the less affecting contribution in terms of final Q, which seems strongly dominated by the clamping losses. Furthermore, the 20 μm gap samples show an higher impact of the *squeezed-film damping* compared to the *drag-force damping*. In fact, these are the only SMRs, which show a gap with lower depth compared to the width of the beam. This seems to partially contribute (0.50 – 0.85 %) to the lowering of the final Q factor.

SMR ($w-d_g$)	Q_s	Q_d	Q_s/Q_d	Q_{c-l}	Q_{TED}	Q_{final}
50-20 (μm)	$1.03 \cdot 10^5$	$2.02 \cdot 10^5$	0.51	540.22	$3.18 \cdot 10^8$	533.12
50-100 (μm)	$1.32 \cdot 10^7$	$2.06 \cdot 10^5$	64.00	540.22	$3.24 \cdot 10^8$	535.89
50-200 (μm)	$1.09 \cdot 10^8$	$2.13 \cdot 10^5$	512.00	540.22	$3.36 \cdot 10^8$	535.96
75-20 (μm)	$4.17 \cdot 10^4$	$2.75 \cdot 10^5$	0.15	360.14	$2.89 \cdot 10^8$	355.33
75-100 (μm)	$5.88 \cdot 10^6$	$3.10 \cdot 10^5$	18.94	360.15	$3.25 \cdot 10^8$	358.41
75-200 (μm)	$4.66 \cdot 10^7$	$3.07 \cdot 10^5$	151.70	360.14	$3.22 \cdot 10^8$	358.43

Table 4.2 Dissipation energy contributions to the final quality factor.

4.5. Responsivity

A preliminary frequency characterization has been used for the determination of the responsivity for each resonant structure. The first mode resonance frequency distribution has been analysed and it is displayed in Figure 4.7a. Taking into account

SMRs with same nominal dimensions (length, width, thickness and channel configuration), the first mode resonance frequency results to be distributed in a relatively narrow range (5.30 and 6.55 %) of values for the beams with length equal to 450 μm and 500 μm . Increasing the length of the SMR, the resonance frequency range seems to be slightly enlarged. This phenomenon can be due to a higher variability of the channel dimensions. Increasing the length of the SMR, the KOH diffusion inside the embedded channel is slowed down, and in some cases it results in a not homogeneous diameter of the central part of the channel and thus in an overall variation of the resonator mass.

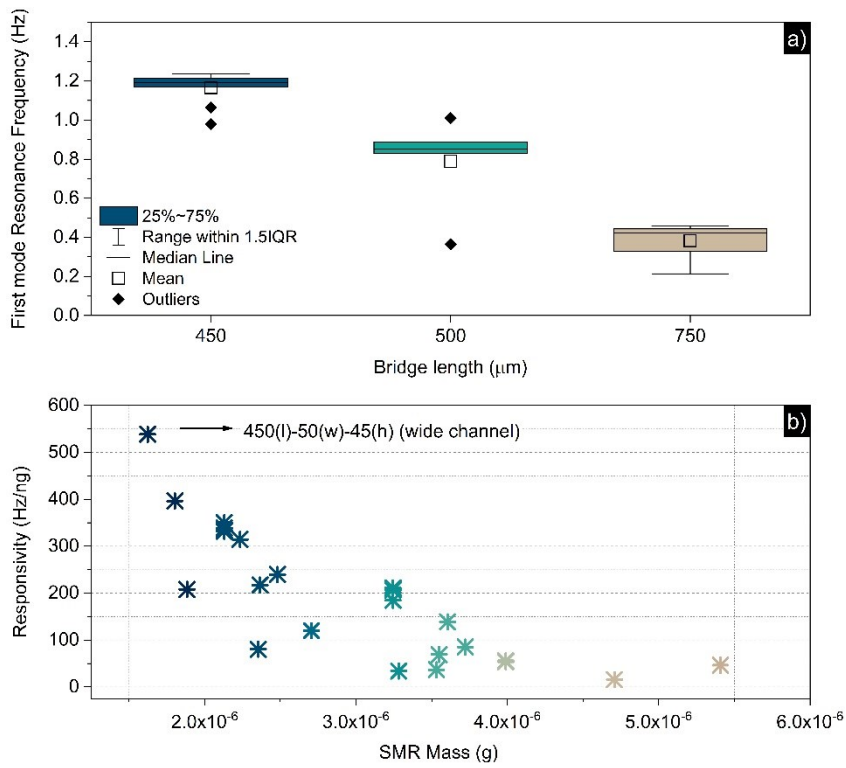


Figure 4.6 Glass SMR resonance distribution and responsivity. a) The distribution of the first resonance frequency, associated to three different SMR length configurations (450 – 500 – 750 μm), is reported. b) The responsivity associated to different SMRs is reported as function of their mass.

Thanks to the accurate characterization of the first resonance mode (f_0) and to the estimation of the resonator mass, the responsivity (\mathcal{R}) of each SMR was computed. Considering the results displayed in the Figure 4.6b the responsivity distribution, the resonator with the best performance was selected. It is possible to observe that the responsivity varies between 15 to 539 Hz/ng for the SMR, the best result is associated

with the smaller beam length and the bigger channel volume. A detailed list of the SMRs responsivity is reported in Appendix B.

4.6. Allan deviation analysis

In order to evaluate the noise and the frequency stability affecting the resolution and the accuracy of the measurement done with this new class of mechanical resonator, an Allan's deviation analysis was performed. The behaviour of each SMR was recorded in air and the results for different designs obtained from 50X and 20X objective-based fabrication were compared. In Table 4.2 it is possible to observe the Allan's deviation values (σ_τ) for each SMR and the relative mass resolution that can be obtained as product of the $1/\mathfrak{R}$ and frequency resolution ($f_0\sigma_\tau$). The data for each resonator are reported in the Appendix B.

<i>length</i> (μm)	<i>channel (h)</i> (μm)	<i>channel (w)</i> (μm)	<i>mass</i> (μg)	f_0 (MHz)	<i>Allan's</i> <i>Dev. (σ_τ-</i> <i>ppm)</i>	<i>mass resolution</i> (pg)
450x50x45	32.17	14.69	1.76	1.18	0.33	1.16
450x50x45	31.28	34.96	1.15	1.23	0.32	0.74
450x75x45	32.17	14.69	2.88	1.22	0.43	2.48
450x75x45	30.55	59.04	1.56	0.98	0.19	0.59
500x50x45	32.17	14.69	1.96	0.85	1.17	4.59
500x50x45	32.17	14.69	1.96	0.41	1.12	4.39
500x50x45	31.28	34.96	1.27	1.01	1.64	4.17
500x75x45	32.17	14.69	3.20	0.89	1.21	7.74
750x50x45	32.17	14.69	2.94	1.23	0.19	1.12
750x50x45	32.17	14.69	2.94	1.01	0.42	2.47
750x50x45	31.28	34.96	1.91	0.89	0.30	1.15
750x75x45	30.55	59.04	2.60	1.19	1.22	6.34
750x75x45	32.17	14.69	4.80	0.83	0.58	5.57
750x70x30	8	7.5	3.16	0.21	0.02	0.13
500x75x30	8	7.5	2.27	0.37	0.03	0.14
700x75x30	8	7.5	3.41	0.25	0.02	0.14
700x80x30	8	7.5	3.87	0.43	0.01	0.08
700x80x30	8	7.5	3.87	0.42	0.02	0.15

Table 4.3 Allan's Deviation and mass resolution values. Allan's deviation values for different SMRs design obtained from the 20X-based fabrication method (first section of the table) and from the 50X-based fabrication method (second section of the table). The mass resolution values (obtained from the mass and the Allan's deviation of each SMR) are also listed in the table.

The SMRs fabricated using the 50X objective show the smallest frequency fluctuations and consequently the highest mass resolutions, around few hundreds of femtograms. For the SMRs fabricated with the 20X objective, the mass resolution varies between 7.74 and 0.59 pg. The lowest values are associated to the SMRs characterized by a small channel (34.96 / 14.69 μm), width and length equal to 75 and 500 μm respectively. However, the overall Allan's deviation values distribution, obtained for the glass SMRs, is comparable to other mechanical resonator that show similar device mass [96,97]. The Allan's deviation values have been also analysed as a function of the environment at which the SMR is exposed (Figure 4.8). In particular, three conditions have been tested: vacuum and air inside and outside the SMR, and water inside the SMR (in air environment). As expected, the minimum frequency fluctuation corresponds to the vacuum condition, which allows to obtain the smallest value of Allan's deviation ($\sigma_\tau = 3.98 \cdot 10^{-8}$). In this case, the SMR has been actuated in vacuum, reducing the source of damping due to the movement of the fluid molecules in the surrounding medium.

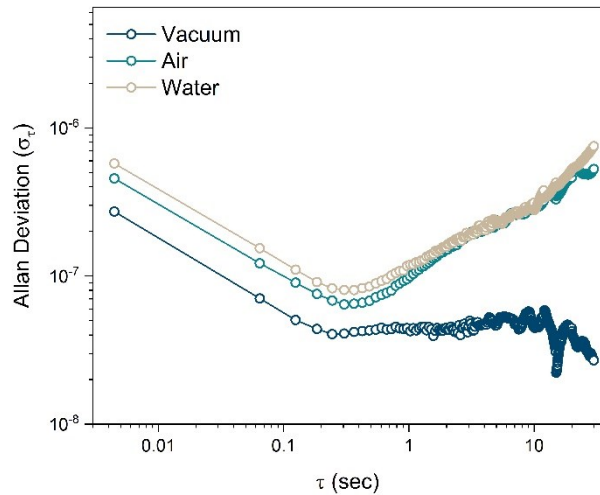


Figure 4.7 Allan's Deviation as a function of the filling fluid, conducted in three different configurations: vacuum/vacuum (dark blue line), Air/Air (light blue line) and Air/Water (grey line). The first mentioned environment represents the surrounding medium and the second the filling fluid.

The results obtained from the channel filled with air or water, in air environment, show the same behaviour and the minimum fluctuation is recorded almost at the same σ_τ and time values for both the experimental conditions (Air: $\sigma_\tau = 6.34 \cdot 10^{-8}$ and $\tau = 0.33$ sec, Water: $\sigma_\tau = 7.89 \cdot 10^{-8}$ and $\tau = 0.33$ sec). Indeed, for the water filled channel, the minimum of the Allan curves is only slightly shifted compared to the air filled channel. This shows how the SMR can be used for fluid measurements without

affecting the overall stability of the frequency, which result to be an important aspect for high-resolved measurements. The frequency stability results almost independent on the filling liquid (see the Allan's curve for air and water). In fact, the surrounding fluid gives the main impact on the frequency stability. As it is possible to observe from the Figure 4.7 the Allan's curve obtained for in vacuum measurement showed the higher stability.

4.7. Liquid density measurements

After the mechanical characterization of the SMRs, the ability in distinguishing liquids with different mass density was verified analysing various standard solutions. The SMRs fabricated with the 50X and 20X objective were compared to define an experimental responsivity for each of them (Figures 4.9a and 4.10).

The microchannel resonator was filled exploiting the PDMS microfluidic system described in Chapter 3, while the SMR was kept in vibration in air (surrounding media). The resonance frequencies for the empty SMR (f_0) and filled with liquid are reported in Figure 4.9a and 4.9c; the measurements were conducted at room temperature (22 °C). All data points were obtained averaging a minimum of three repeated measurements for each liquid, in single point modality. In order to minimize possible contaminations between the different liquids, after each characterization the channel was cleaned and the value of fundamental resonance restored. As expected, for both SMR types, the resonance frequency changes linearly with the fluid density (Figure 4.9a and 4.9c), so that the SMR density responsivity can be defined as the slope of the calibration curve. In Figure 4.9b are reported the frequencies curves relative to the first resonance mode of the SMR fabricated with the 50X objective. Changing the filling liquid, the resonance frequency is shifted to lower values as a function of the density increase.

For the 50X SMR, the density responsivity is 8.9 Hz/kg·m³, which is one order of magnitude smaller than the density responsivity estimated for the 20X SMR (46.8 Hz/Kg·m³). However, considering the volume normalization the experimental mass responsivity resulted the same for both the SMRs, as reported in Table 4.3. Through the frequency resolution ($f_0 \cdot \sigma_\tau$), obtained from the Allan's deviation (Appendix B), and the previously calculated density responsivity, it has been possible to estimate the mass density resolution, which resulted 1.04·10⁻³ kg/m³ for the 50X SMR and

$8.01 \cdot 10^{-3} \text{ kg/m}^3$ for the 20X SMR, i.e. the highest value among previously cited sensors. The inverted trend between the two types of SMR is due to the strong effect of the Allan's deviation values, which describe the 50X SMR as the device with the major frequency stability. However, the density responsivity, for both the SMRs, is comparable or better respect to the resonant microcapillaries used for the same purpose [25,26].

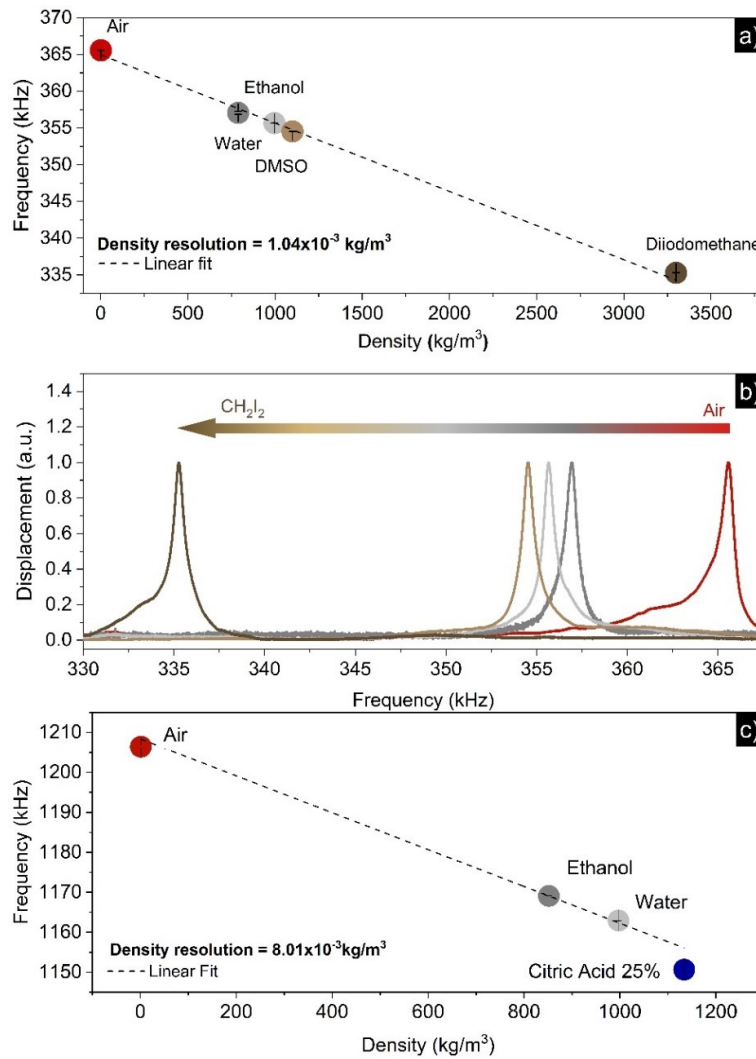


Figure 4.8 Frequency shift as a function of the filling fluid. a) The first mode frequencies measured filling the SMR (fabricated with 50X objective) with five fluids of different density (calibration plot). b) The resonance frequency plotted for different fluid used to fill the SMR. c) The frequencies measurement as function of the filling liquids (calibration plot) has been repeated for the SMR fabricated with 20X objective. In this case, the liquids used for the test are slightly different respect to those reported in the graph (a).

Analysing the behaviour of the quality factor as a function of the fluid viscosity (Figure 4.10a), the SMR in vacuum environment showed the highest Q factor value, as easily expectable. On the other hand, small variations of the Q factor (between

1.35% and 13.75%) are experienced when the SMR is filled with different fluids in comparison to the same air-filled microchannel, confirming that the damping is mainly dominated by the interaction with the surrounding air and by the clamping losses, rather than the fluid inside the channel. The general trend shows a non-monotonic dependence of Q-factor on fluidic viscosity and density (Figure 4.10b), as stated by theory and experiments concerning energy dissipation in SMRs [31,4].

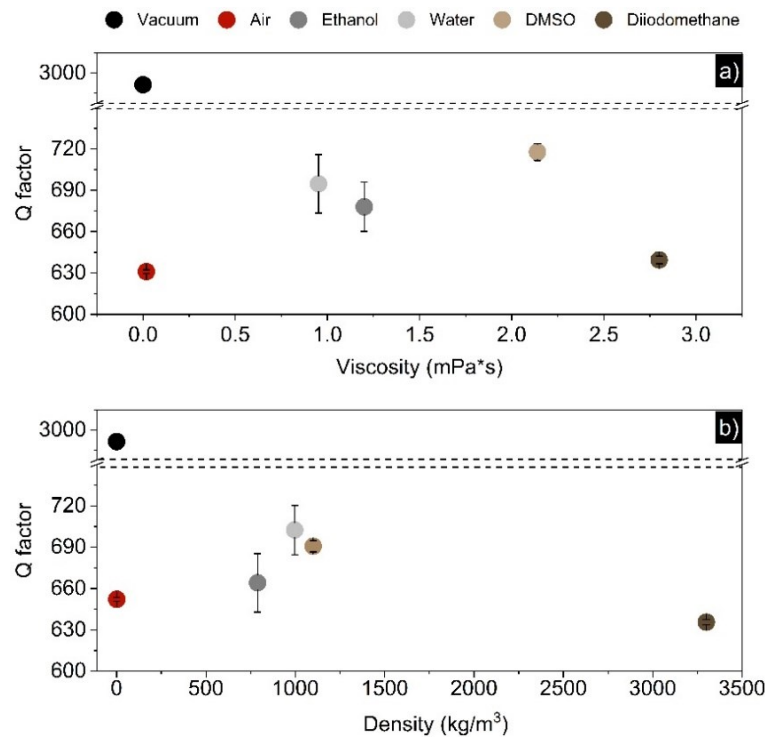


Figure 4.9 Q factor as function of viscosity and density of the filling fluid. a–b) Q factor variation due to the viscosity and density of the measured fluid. As expected, the variation follows a non-monotonic behavior for both the physical properties of the filling fluid.

4.8. Measurement of Bacterial cells

4.8.1. Methods: bacterial culture

Considering the great impact of the SMRs implementation in the field of biomedical diagnostics, as demonstrated by Manalis et al. [32,33], the here presented glass SMRs were validated also for this kind of application. The measurement approach was based on the microgravimetric analysis of *P. fluorescens* bacteria (0.3 x 1.3 μm , rod shape), suspended in aqueous solution at different concentrations. This non-pathogenic microorganism was selected as representative strain of the pathogenic *P. aeruginosa*, responsible of multi-drug resistance in nosocomial

infections [34,35]. *P. fluorescens* DSMZ 50090 (ATCC 13525) was streaked and grown overnight on a DSM1 agar plate (composition per liter: 5 gr peptone, 3 gr meat extract, 15 gr agar, pH 7.0) at 20 °C [28]. Then, the plate was resuspended with 5 mL of fresh DSM1 broth. The optical density at 620 nm (OD_{620}) of the tenfold diluted suspension was adjusted to 1.6 and finally serially diluted for the microgravimetric test. Considering the small sampling volume (157 picoliter) inside the SMR, the starting stock concentration was adjusted at $2 \cdot 10^9$ CFU/mL. This concentration allowed to have a relevant number of bacteria present at the same time in the microchannel.

4.8.2. Microgravimetric analysis

The number of bacteria, for each dilution, was evaluated taking into account the mean relative frequency shift ($\Delta f/f_0$), caused by the bacterial mass present in the microchannel, and the mean *P. fluorescens* density (1.13 g/cm^{-3}) [98]. The $\Delta f/f_0$ represent the relative frequency variation with respect to the blank solution, in which the *P. fluorescens* cells are dispersed (ratio of dilution 0.00): in this way the frequency variation can be directly linked to the mass of bacteria. The $\Delta f/f_0$ are expressed as negative values, in agreement with the well known mass–frequency relationship described by equation 2.14.

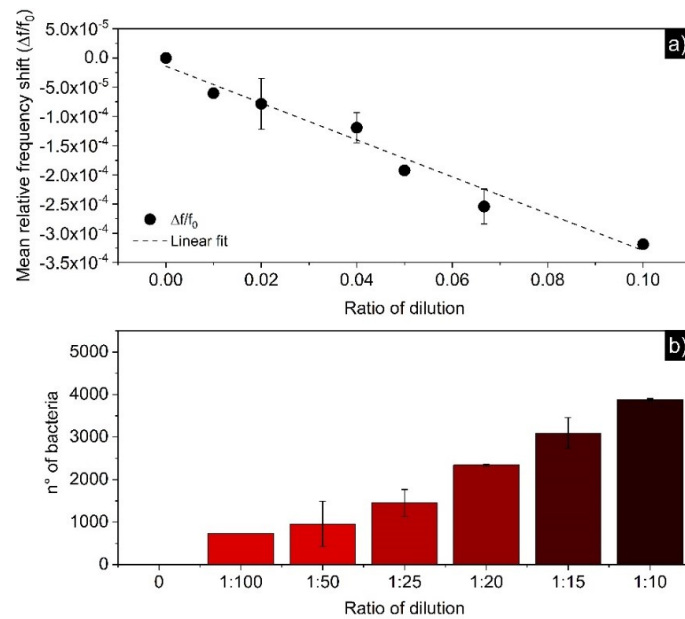


Figure 4.10 *Pseudomonas fluorescens* microgravimetric analysis. a) Mean relative frequency shifts (for the first resonance mode) due to the mass of bacteria contained in solution with different concentration. b) Number of bacteria extrapolated from the microgravimetric analysis and associated to different concentration.

The results of the microgravimetric analysis reported in Figure 4.10a shows an almost linear $\Delta f/f_0$ variation decreasing the dilution ratio. To evaluate the effectiveness of the measurement protocol, each dilution was measured at least three times. In order to minimize any possible contamination between the measurements, after each characterization the channel was cleaned and the fundamental resonance restored.

Considering the mean density of *P. fluorescens*, it has been also possible to evaluate the number of bacteria that caused the frequency shift (Figure 4.10b).

In order to evaluate the intra and inter-experiment variability, the microgravimetric test was repeated a second time, following the same culture conditions and testing some of the dilution condition displayed in Figure 4.11. In the new analysis, the blank and only the three most representative dilutions were tested: 0.01, 0.05 and 0.10 (Figure 4.11). The SMR was able to distinguish the different samples with a good confidence, confirming the SMR performance obtained in the previous test. The intra and inter experiment tests show an extremely high repeatability, with a small increase of the variability for the lower dilution ratio, which can be easily explained by the intrinsic variation of the bacterial growth rate in the two batches.

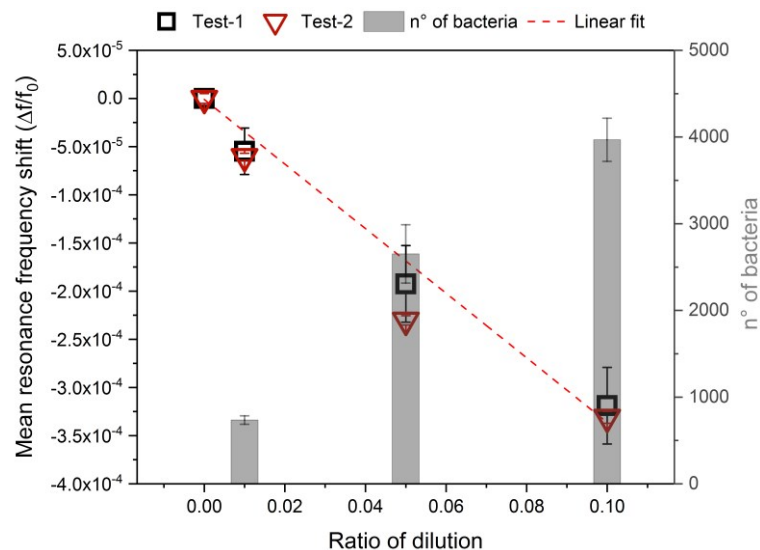


Figure 4.11 Repeatability of the bacteria-counting test. Mean resonance frequency shift associated to the solution containing different concentration of bacteria: the test was repeated two times with multiple sampling for each concentration, in order to determine the intra and inter-experiment repeatability. The number of bacteria was extrapolated from the average of the test-1 and test-2.

Considering the linear behaviour observed from the variation of the resonance frequency as function of the dilution ratio, the limit of detection (LOD) and limit of

quantification (LOQ) can be easily determined as 150 and 481 bacteria, respectively. These figures of merit were calculated as three and ten times the standard deviation of the blank, considering the linear fit in Figure 4.12. Finally, this proof of concept experiment shows that the here presented SMRs can be exploited for real time monitoring of bacterial growth with enhanced performances, if integrated into a recirculating system.

Chapter 5

Beads assay

5.1. Introduction

The modern approaches for the bioanalyte detection are mainly based on the immobilization of the capturing molecules on flat surfaces [99–103], which show two important constraints: the low intrinsic possibility to enhance the capturing ability and the diffusion-limited transport characteristics deriving from 2D systems. In most cases, these issues are connected to the optimization of time-consuming amplification strategies [104,105]. Compared to the 2D systems [106,107], the usage of 3D substrates offers the possibilities to overcome these problems thanks to the high surface area available for the immobilization of the biorecognition elements [73,108,109], increasing the sensitivity and lowering the limit of detection [110,111]. In this context, one of the most interesting 3D substrate is represented by porous micro or nanoparticles. In fact, the kinetics that is involved in the binding of the analytes to the capturing molecules, immobilized on these porous media, is similar to the kinetics that governs the binding of two free molecules in solution [112]. Furthermore, the high binding capability of porous media results fundamental in the analysis of low volume samples with low target analyte concentration [113].

Independently from the system type (2D or 3D), the chemical properties of the immobilization substrate play a key role in the selectivity of the biomolecular assay. Generally, the functionalization of a planar microarray requests a serialized and time-consuming process [114–116]. In contrast, the functionalization of the beads can be

done in batches, reducing the statistical difference of the process, and can be directly integrated during the beads synthesis [117–119].

Materials like mesoporous silica have been deeply studied as ideal substrate for the synthesis of micro or nanoparticles with high surface area [120]. Furthermore, the mesoporous silica shows high modification degree that involves both the morphology (beads and pores dimensions) and the surface chemistry, which can be modulated depending on the final application [119,121,122]. In the medical microdevices field, the possibility to fully integrate a substrate with high capturing capability, high-throughput properties and scalability, can be considered as one of the most important requirements [111,113,123,124]. The usage of the porous beads can supply these needs and can be used as versatile substrates for the integration on many different sensing platform, based on both label and label-free detection approaches.

In this work, the main purpose taken into account was the use of this 3D substrate for the optimization of a DNA–DNA hybridization assay, to be directly integrated in the SMR platforms. This will allow the creation of a label-free sensing system able to couple the characteristic high mass sensitivity of the SMR, with the high capturing capability of the mesoporous beads. The DNA–DNA hybridization assay was selected as a model test based on oligo-probes as biorecognition element, due to their broad application in the detection of relevant medical biomarkers [125–127]. In order to do that, it has been necessary to optimize a bioassay at the beads scale. The mesoporous silica ($mSiO_2$) was chosen as preferential material, thanks to the easy procedures of synthesis that can be used to obtain it. Furthermore, this material shows two important advantages: the pores dimensions that can be easily tuned to be compatible with the DNA immobilization (20 bp long) and the possibility to modify the oxydrilic superficial groups by simple chemical strategies that makes selective the particles loading. In the literature, many different approaches for the synthesis of mesoporous silica beads can be found. In this work the attention was focalized on the acid condensation and on the co-condensation methods for the rapid synthesis of multifunctional substrates. Through the careful tuning of temperature, reagent concentration and time of reaction, it has been possible to obtain mesoporous silica beads with an average diameter of 6 μm , which correspond to the desired dimension range compatible with the dimensions of the SMR embedded channel. Afterward, this method was coupled with a co-condensation strategy, chosen in order to add

specific functional groups on the microbead surface. The co-condensation method was preferred, to more standard post grafting process, in order to keep the morphological properties of the modified beads closest to pristine mesoporous silica. In fact, the co-condensation of specific alkoxy silane with the silica precursor generally shows a limited impact on the beads and pores dimensions. For this purpose, two different organosilane were used: aminopropyltriethoxysilane (APTES) and mercaptopropyltrimethoxysilane (MPTMS), obtaining two different batches of mesoporous beads that have been deeply investigated as substrate for the DNA-DNA hybridization assay.

5.2. Mesoporous silica materials

The increasing interest on porous solid materials date back to 1992, when the Mobil Research and Development Corporation synthesized for the first time a solid mesoporous aluminosilicate gel [128]. The synthesis was developed exploiting the liquid crystal mechanism and they defined this new material with the name of MCM-41 (Mobile Crystalline Materials or Mobil Composition Matter).

Considering the IUPAC definition, a mesoporous material should be characterized by a pore size in the range of 2 – 50 nm, distributed into the material with an ordered structure [129]. The morphology of these structures can vary depending on the starting precursors and on the reaction conditions that can affect both the pores shape and size. So far, scientist from all over the world contributed in the development of a wide spread variety of mesoporous materials [130]. The most studied are the MCM (Mobile Crystalline Materials) [131,132], the SBA (Santa Barbara Amorphous) [133,134], the KIT (developed by Korea scientists) and the FDU (Fudan University of China) series [135,136]. Each of them constitute a specific class of mesoporous material with a well define associated structure (Figure 5.1); among them the hexagonal, the cubic and the lamellar phase constitute the most common type of structure associated to the synthesis of mesoporous materials [117,130,137].

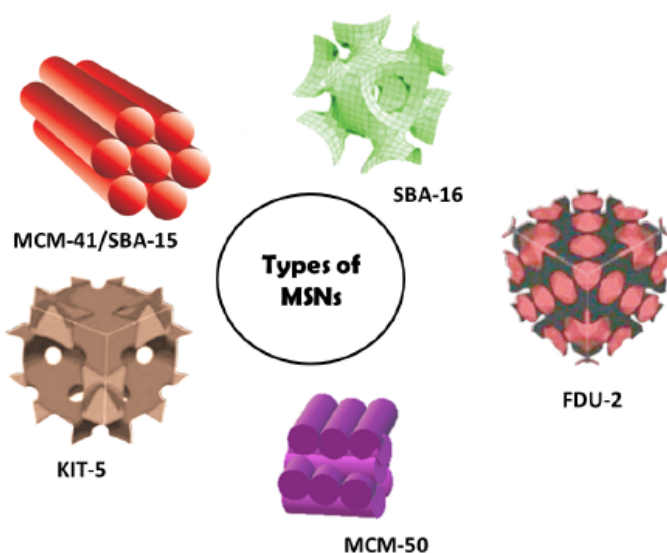


Figure 5.1 Most common types of mesostructured frameworks obtained by the synthesis of mesoporous silica based materials. Picture from “Mesoporous silica nanoparticles: A comprehensive review on synthesis and recent advances” R. Narayan et al. *Pharmaceutics* 2018, 10, 118, doi:10.3390/pharmaceutics10030118.

The mesoporous silica micro or nano-particles (MSMs and MSNs, respectively) are one of the possible materials that can be obtain exploiting the liquid crystal mechanism [138–141]. The MSMs and MSNs are attracting wide interest in many research field like efficient adsorbent carriers for drugs, proteins, DNA, RNA and enzymes loading [123,142]. In fact, the possibility to obtain a uniform porous structure, with tunable pore size, makes these materials suitable for the realization of controlled delivery systems for drugs and other macromolecules [143,144]. Furthermore, the beads surface can be easily functionalized with a great variety of chemical groups [145,146] that results particular attractive also for the usage of this materials in the field of air and water purification [122].

5.3. Mechanism of mesostructured formation

The liquid crystal mechanism [140], proposed by the researchers of Mobil Corporation, is based on the supramolecular assembly of the surfactant micelles into well defined structures, which promote the formation of the mesophase [147]. In this case, the surfactant micelles act as soft template [130,148] that coordinate the “guest” species to rearrange around the surfactant structure (Figure 5.2) [148], as result of the spontaneous behaviour to reduce the interface energy [149,150]. The liquid crystal mechanism, or “soft-template method” is one of the two possible methods that can be used for the synthesis of mesoporous materials, a second strategy is based on a hard-

template method [151,152]. In this case, a preformed mesoporous solid act as structure directors for the rearrangement of the “guest” species; this approach is also known with the name “nanocasting”. For the micro and nano–particles synthesis, the soft–templating method is generally preferred to the hard–templating method; this is probably due to the simplicity of the synthesis procedure and of the tailoring of the mesoporous structure.

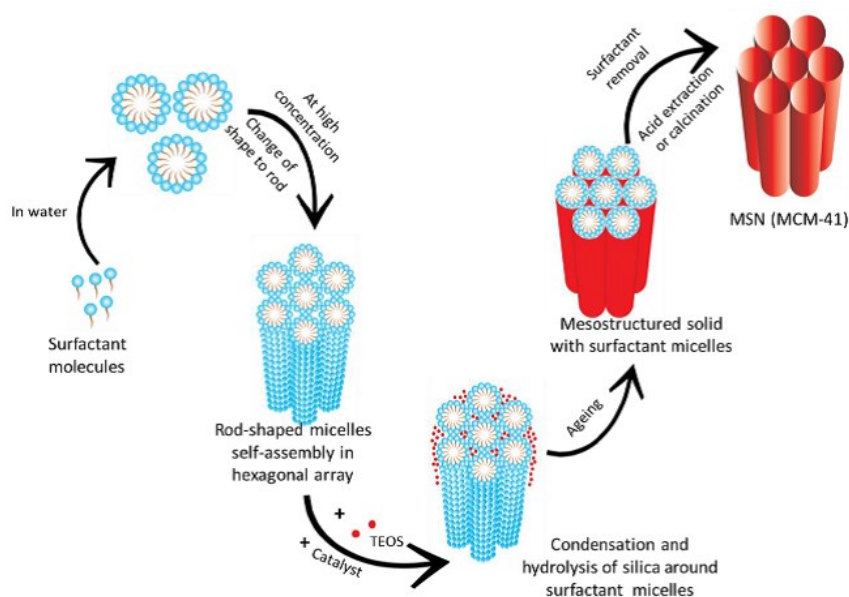


Figure 5.2 Surfactant micelles self-assembly into a rod–shape structure, which is used to direct the condensation and hydrolysis of the silica precursor forming the characteristic mesoporous framework of the silica based materials. Picture from “Mesoporous silica nanoparticles: A comprehensive review on synthesis and recent advances” R. Narayan et al. *Pharmaceutics* 2018, 10, 118, doi:10.3390/pharmaceutics10030118.

Nevertheless, the synthesis of mesostructured silica is based on complex building blocks if compared to the metal or semiconductor nano and micro–particles synthesis. In fact, the characteristic mesostructured requires to take into account the delicate interaction between organic templates and inorganic species (or silica precursors) [153]. Among the experimental factors that should be controlled, the silica condensation rate, the interaction of silica–template, the kinetics of assembly and the growth/nucleation rate play a key role in in the mesostructured formation [117,122,154]. The majority of the mesostructured silica particles are obtained by the modified Stober’s method (sol–gel process) [155]. This strategy involves the hydrolysis and condensation of the silica precursor (Si–OR and Si–OH–containing species) into a colloidal solution (sol) that is fundamental to form the ordered inorganic network (gel) and subsequently the particles [155]. From the structural

point of view, the ordered network can be described as a connection of SiO₄ tetrahedra (or SiO₃ – hybrid material) by corner sharing, stabilized by the siloxane bonds (Si–O–Si) between the precursor molecules. The stability of the gel phase is strongly dependent on the hydrolysis and condensation rate that should maximize the number of siloxane group, decreasing the number of free silanol (Si–OH) and alkoxo (Si–OR) species in solution.

There are two different types of precursors that can be used in the mesoporous silica synthesis: the aqueous solution of silicates that contains different silicate species (metasilicate) and the silicon alkoxide (Si–OR₄), mainly tetramethoxysilane (TMOS) and tetraethoxysilane (TEOS). Focusing the attention on the silicon alkoxide, the hydrolysis/condensation reaction can take place both in acid and basic conditions and the hydrolysis of the Si–OR into Si–OH groups must precede the condensation (Figure 5.3). Starting from the Si–OH terminal groups associated to the precursor molecules, this condensation step involves the Si–O–Si network formation followed by water or alcohol release.

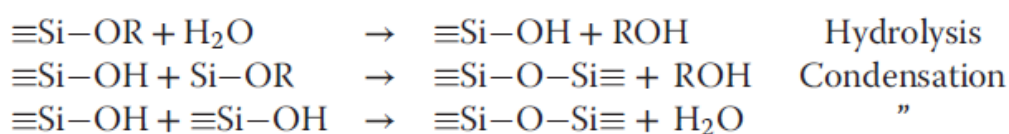


Figure 5.3 Typical reaction pathway of hydrolysis and condensation of the silica precursor during the sol-gel synthesis of the silica based materials. Picture from “The Sol-Gel Handbook: Synthesis, Characterization, and Application”, First Edition 2015 Wiley-VCH.

One of the advantages of the silicon alkoxides is the possibility to introduce specific functional groups, directly during the synthesis process [119,145], using for example an alcoxysilanes mixture (R’Si(OR)₃ + Si(OR)₄) or a diorganodialcoxysilanes (R₂’Si(OR)₂), which are rarely used because of their tendency to turn into chained structures instead of branch like-structures. The nature of the R’ substituents can directly stabilize or destabilize the intermediate forms during hydrolysis/condensation reaction, so the components of the alcoxysilanes mixture must be chosen carefully [155].

The sol-gel process can take place in the presence of both acidic and basic catalysts, with a different hydrolysis/condensation rate [130]. Under acidic conditions, the pH is generally set below the point of zero charge (PZC) and the ≡Si–O[–], ≡Si–OH and ≡Si–OR groups are protonated during the hydrolysis step, with the creation

of leaving groups. Consequently, the central silicon atom becomes more electrophilic, (due to the change of the electron density distribution), and thus more subject to hydrolysis and condensation reactions. On the contrary, under basic conditions the mechanism of reaction is governed by a nucleophilic attack (S_N2 -type) of the silicon atom by the negative charged ions: OH^- during the hydrolysis reaction and $\equiv\text{Si}-\text{O}^-$ during the condensation reaction (Figure 5.4).

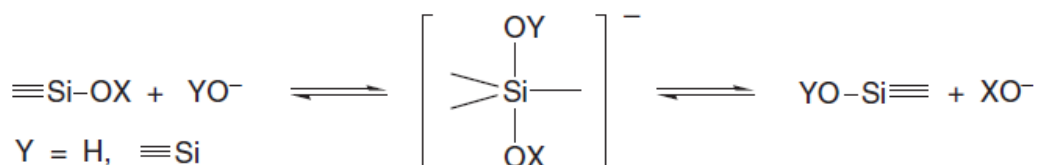


Figure 5.4 Nucleophilic attack pathway of the silicon atoms (alkoxysilane precursor) involved in the synthesis of the mesoporous silica materials under acidic conditions, where, X and Y are respectively R and H for the hydrolysis reaction or R/H and Si \equiv for the condensation reaction. Picture from “The Sol-Gel Handbook: Synthesis, Characterization, and Application”, First Edition 2015 Wiley-VCH.

Considering the two mechanisms (for acidic and basic catalysts), it is possible to predict the reaction rates related to the hydrolysis and condensation [153]. In particular, under acidic conditions the hydrolysis and the condensation rates increase proportionally to the electron density, but for the basic conditions a negative charged intermediate must be stabilized, thus the reaction rate for both, hydrolysis and condensation, increases when the electron density decreases. These behaviors have several consequences on the gel-phase formation, for example in acidic media the hydrolysis of monomeric $\text{Si}(\text{OR})_4$ is favored with respect to the partially hydrolyzed $\text{Si}(\text{OR})_{4-x}(\text{OH})_x$ and to the oligomeric forms, which exhibit a larger number of Si-O-Si bonds. Therefore, in acidic conditions, the formation of chain-like network is preferential and is mainly due to the hydrolysis and condensation reactions affecting the central silicon atoms (Figure 5.5). For basic catalysts, the observed behavior is exactly the opposite: the terminal silicon is the atom preferentially involved in the hydrolysis and condensation reactions and the network shows a branch-like structure (highly condensed) (Figure 5.5). Furthermore, considering the sol-gel reaction in co-presence of multiples alkoxysilane [156] (with special functionalities) or diorgano-dialkoxysilanes (with double functionalities), the acidic catalysts promote, with higher rate respect to the base catalyst.

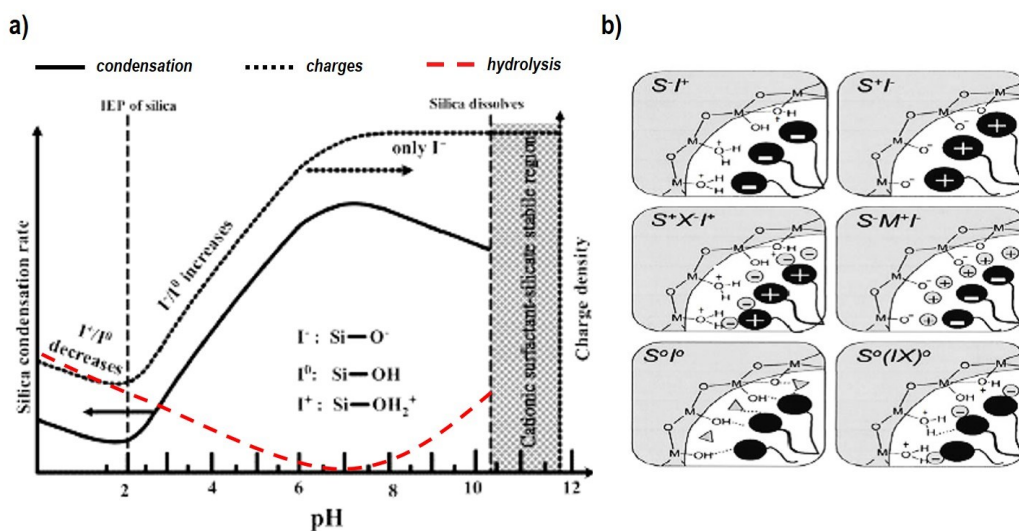


Figure 5.6 pH of reaction affection the condensation/hydrolysis reaction. a) Kinetics of the silicon condensation rates as function of the pH and relative ratio neutral/charged species in solution; b) Possible pathway of interaction between the surfactant micelles and the silica precursors as function of relative charge of the species in solution. Pictures partially modified from “Synthesis of mesoporous silica nanoparticles” Wu et al. Chem Soc Rev 2013, DOI: 10.1039/c3cs35405a and from “A Review: Fundamental aspects of silicate mesoporous materials” Z.A. Allothman, Materials 2012 doi:10.3390/ma5122874.

Nevertheless, the possibility to obtain the formation of the mesophase using surfactants with the same charge of the silica species is allowed in presence of specific mediating ions (M^+ or X^-) (Figure 5.6b). Finally, a third pathway is possible in presence of neutral silica species (I^0) and non-ionic surfactants (S^0): in this case the interaction among them is promoted by hydrogen-bonding [154].

5.4.2. Surfactants and Swelling agents

The formation of the mesophase depends on the presence of surfactants in solution and in particular on their type and concentration [157]. In fact, at low concentrations the surfactant molecules exist as monomers, whereas increasing the concentration they start to combine into isotropic micelles, to reduce the entropy of the system [158–160]. This concentration threshold is also known as “critical micellization concentration” (CMC), and with a further increase of the concentration of surfactants the micelles start to organize into tightly packed array, limiting the surface or interfacial tensions. Depending on the concentration, different array of micelles can be obtained, i.e. exagonal, cubic or lamellar structures that are characteristic of the Liquid Crystal Phase [161,162].

The formation of a particular phase depends not only on the concentration of surfactants, but also on the nature of the surfactants itself (i.e. the length of the hydrophobic chain, the type of hydrophilic head, the presence of specific counter ions). Generally, increasing the length of the hydrophobic carbon chain the CMC is decreased, on the contrary the CMC is shifted to higher values if the radius of the counterion is increase, as well as increasing the pH or the temperature of the synthesis solution [130,154]. The CMC can be reduced also increasing the ionic strength of the synthesis solution or increasing the valence of the counterions.

The presence of the surfactants not only affects the structure of the Liquid Crystal Phase, but also the pores size and the thickness of the pore walls. Depending on the interaction between the inorganic silica species and the organic surfactants, the thickness of the pore walls can be varied. For example, if the interaction is promoted by hydrogen bonding, the framework structure shows thicker walls with enhanced thermal and hydrothermal stability [130]. The size of the pores can be tune changing the hydrophobic chain length that directly affects the aggregation number and the diameter of the micelles. A further increase of the pore diameter can be obtained using auxiliary organic species (i.e. trimethylbenzene) as fillers [163]. In fact, these species are strongly hydrophobic and once added into the synthesis solution they are solubilized inside the surfactant micelles, which lead to an increase of the diameter of the micelles first and consequently to that of the pores. The mesostructures obtained from the addition of the swelling agent show larger pores dimensions, but the pore structure tends to a wormhole-like connection, which is not suitable for the loading of macromolecules of large dimensions. As mentioned at the beginning of the paragraph, different species of surfactants can be used for the synthesis of the mesoporous materials. Recent developments have shown great potential in the usage of the non-ionic surfactants, in particular the triblock-copolymers (Pluronic P65, P123 and F127) [157]. These surfactants can be also associated with different compound of the benzene as swelling agent to enlarge the pore dimensions. In particular, the triblock-copolymers are interesting as structural agent for the synthesis of mesoporous materials in acidic conditions, obtaining networks with 3D cubic, 2D hexagonal, foam-like or disordered structure (pore sizes 5–30 nm) [164].

5.4.3. Alkoxo roup/H₂O ratio (R_w)

The R_w parameter defines how much the silanol group formation is favoured respect to Si–O–Si groups [155]. In particular, the increase of the water amount in the reaction solution, corresponds to lower R_w , favouring the Si–OH formation. Generally, four equivalent of water are required to completely hydrolyse the $Si(OR)_4$ species and this ratio have to be taken into account, together with the pH, in order to optimize the hydrolysis/condensation rate.

5.4.4. Electrolytes

The presence of electrolytes in solution can affect the gelation behaviour of the sol–gel process. Increasing the concentration of charged species, the repulsive barrier among the particles is reduced inducing the coagulation of the colloidal solution. This phenomenon, if not controlled, can reduce the reproducibility of the sol–gel process. In particular, unwanted salt contamination must be avoided, and depending on the catalyst used, it could be necessary to take into account the possible contamination due to the presence of acid or basic counterions.

5.4.5. Reaction temperature

The synthesis temperature for the mesoporous structure can range from 10 to 150 °C, and together with the pH and the composition of the synthesis solution, strongly affects the particle and pore sizes [165]. The ideal temperature can be selected taking into account two important parameter: the Critical Micelle Temperature (CMT), which define the low temperature threshold for the micelles formation, and the Cloud Point (CP) that determine the temperature at which the surfactant precipitates [130]. Particular attention must be applied in the use of non-ionic surfactants that become insoluble at high temperatures. In these cases, the usage of an acid catalyst can shift the CP to higher values, enabling the synthesis at high temperature. However, a low reaction temperature (that reduce the reaction rate) is often desirable in order to obtain materials with crystalline regularity. Furthermore, the reaction temperature can affect also the particle dimensions; higher temperatures normally promote higher hydrolysis/condensation rates [130].

The regularity of the mesoporous structure can be further improved and stabilized by post-synthesis hydrothermal treatments [166]. Depending on the duration of the treatment the mesophase can be also transformed from one network structure to another.

5.5. Template removal

The removal of the template is a fundamental step in order to obtain a free and available porosity [130,154]. This procedure can affect the characteristics of the mesoporous structures and can be performed using different strategies, such as calcination, extraction with solvents, microwave digestion or irradiation using ultraviolet lamps [167]. The calcination is the most common method and ensures a complete elimination of the template. In fact, the organic surfactants can be easily decomposed at high temperature ($> 350^{\circ}\text{C}$) under oxygen or air atmosphere, but in order to avoid the collapse of the mesoporous structure, the calcination must be conducted by using a slow ramp of temperature increase. This approach is particularly suitable in the case of bare mesoporous silicates that do not show any particular chemical functionalities incorporated in the structure. Depending on the nature of the surfactant the calcination temperature can range between 350 and 550 $^{\circ}\text{C}$: high temperature are usually suitable for the removal of the triblock-copolymer and long-chain alkyl surfactants.

The extraction of the template in organic solvent solution represents a second effective way to remove different types of surfactants. Ethanol or THF (tetrahydrofurane) are used as extracting agents, and to improve the removal of the template, the extraction is usually conducted at 80 – 100 $^{\circ}\text{C}$ [168]. This process results particularly useful for the treatment of mesoporous materials synthesized in the presence of alkoxy silane with specific chemical functionalities, like the one used to obtain particles *via* co-condensation process. Unfortunately, the extraction in organic solvent solution is not able to completely remove the surfactants, especially if the triblock-copolymer has been used as template. In this case, the extraction efficiency is about 95% [130].

5.6. Functionalization

In the last years, new bifunctional and multifunctional mesoporous materials have been largely investigated, creating a new class organic/inorganic solids with specific properties and reactivity that allow the use of mesoporous materials as catalyst, adsorbent or sensor substrates [169]. To get the proper functionality, a wide range of organic moieties can be incorporated into the mesoporous structures. In particular, for the silica based materials the surface modification can involve different functionalities, including amine, thiol, carboxylic, chromophore, epoxide, imidazole, and so on [170]. Considering the typical sol-gel process exploited for the synthesis of these materials, the functional groups can be easily incorporated into the structure by two main strategies: grafting and co-condensation procedures [156,171,172]. The addition of functionalities using the grafting procedures is generally based on the superficial modification of the pore wall during a post-synthesis approach. On the contrary, the co-condensation process allows to directly embed the functionalities into the mesoporous framework during the synthesis of the silica beads. Both the strategies show advantages and constraints. In particular, the grafting procedure can be used to incorporate a wider variety of functional groups respect to the co-condensation procedures that require to exploit a precursor compatible with those reagents used for the synthesis of the mesoporous silica materials. Unfortunately, the grafting procedures drastically modify the morphological properties of the mesoporous framework, especially because the addition of the functionalities using the post-synthesis procedures affect the pore shape and dimensions [156]. This problem can be avoid using the co-condensation approach that can ensure a constant pore dimension compared to the non-modified mesoporous framework.

5.7. Methods

5.7.1. Microbeads synthesis

The synthesis of the mesoporous silica beads was accomplished by means of a versatile surfactant/swelling agent template strategy, deeply characterized by Huang et al. 2015 [135]. The synthesis procedures was adapted and modified in order to

obtain the desired silica microbeads that exhibit different functionalities incorporated into the mesoporous framework. A block copolymer surfactant (Pluronic F127) has been chosen as surfactant and combined with a micelle expander characterized by high solubility in the surfactant micelles (toluene).

Synthesis of mesoporous silica microbeads (Figure 5.7). The synthesis started with the dissolution of 1 g of F127 in 60 mL of HCl aqueous solution (2M); the mixture was kept under constant stirring at 500 rpm at room temperature, until the complete dissolution of the surfactant. Then, 3 mL of toluene or trimethylbenzene were added and the mixture was kept at 12 °C, 500 rpm. After 24 h, 4.5 g of tetraethyl orthosilicate (TEOS) were added drop by drop, continuously stirring the mixture for 24 h at 12 °C. Then, the reaction mixture was transferred into a polytetrafluoroethylene (PTFE) bottle, diluted adding 40 mL of HCl (2M) and thermal treated at 100 °C for 1 day. The obtained product was finally separated by centrifugation (4000 rpm for 10 min), washed three times with ethanol and dried at 60 °C. The as synthesized microbeads were calcined at 550 °C under air atmosphere for 6 h, in order to remove the surfactant.

Synthesis of modified mesoporous silica microbeads (Figure 5.7). The procedure described above was adapted in order to realize a co-condensation process for the incorporation of NH₂, COOH and SH functionalities. The strategy foresees the addition of a specific organosilane immediately after the TEOS addition step. Using this strategy it has been possible to modify the chemical properties of the mesoporous framework. In particular, for the NH₂ and SH functionalities, 0.18 and 0.09 g of (3-aminopropyl)triethoxysilane or (3-mercaptopropyl)trimethoxysilane were respectively added (drop by drop) to obtain a modified beads characterized by 1:25 and 1:50 organosilane/TEOS ratio. After the thermal treatment, the surfactant template has been removed using an extraction method based on concentrated ethanol at 80 °C for 24 h.

The COOH functionalities have been obtained modifying the NH₂ terminals using a solution of succinic anhydride (50 mM) in THF and 5% TEA for 3 h at room temperature, by adapting a previous functionalization method [173]. After the reaction, the beads were washed 3 times in THF, 2 times in ethanol and finally 2 times in water followed by drying at 60 °C.

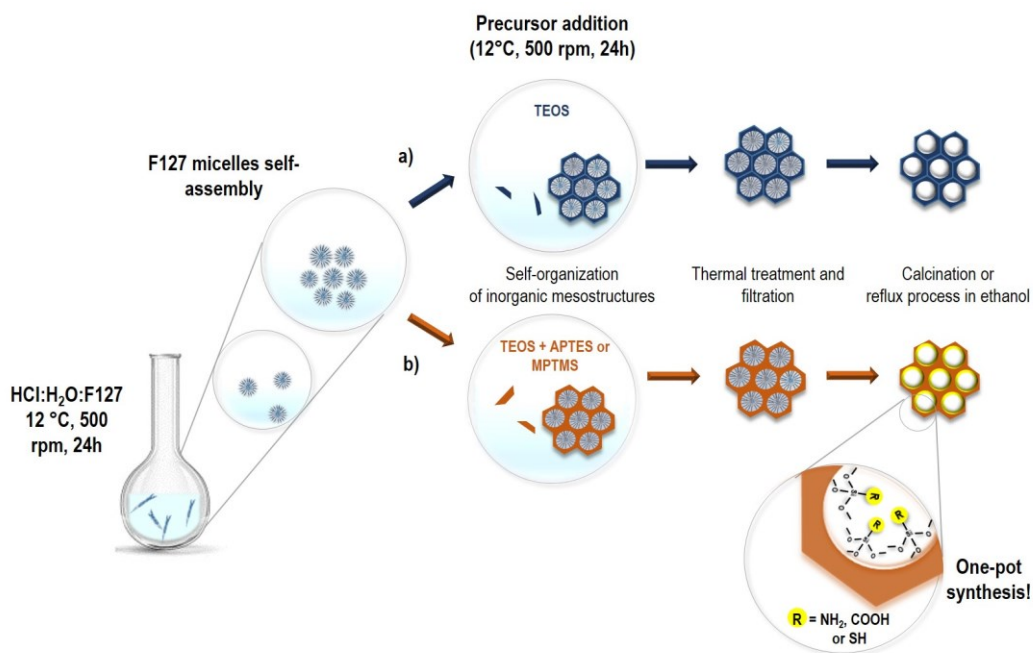


Figure 5.7 Synthesis protocol of mesoporous silica beads characterized by ultra large pores. a) Schematic representation of the mesoporous bare silica framework formation in acidic conditions; b) Schematic representation of the one-pot synthesis used for the formation of a functional mesoporous framework.

5.7.2. Measurement protocols

Branauer–Emmett–Teller analysis (BET). The properties of the beads mesoporous framework has been evaluated by the BET analysis (micrometrics – ASAP 2020 Plus). The N_2 adsorption/desorption has been investigated using 0.06 g of dry beads powder cooled down at 77 K (ramp rate 283 K/min).

Scanning electron microscope analysis (SEM). The morphology of the pores has been characterized by means of a scanning electron microscope – Carl ZEISS MERLINTM. The beads powder were dispersed in ethanol in order to obtain a 2 mg/mL mixture, subsequently 5 μ L of the mixture were deposited on a silicon substrate and dried at room temperature for a few minutes. The samples, as prepared, were used for the SEM analysis.

Thermal gravimetric analysis (TGA). The incorporation of the new chemical functionalities into the mesoporous beads was evaluated by TGA analysis in the temperatures range of 25 – 800 °C. 18–27 mg of powder were analysed and the amount of organosilane incorporated was evaluated taking in to account the following equation:

$$\text{silane \%} = \left[\frac{(mg_{150^{\circ}C} - mg_{600^{\circ}C})}{mg_{150^{\circ}C}} \right] \cdot 100 \quad 5.1$$

Fourier–transform infrared spectroscopy (FTIR). For what concern the NH₂ and COOH modified beads, the effective incorporation of the new functionalities was also evaluated by means of FTIR spectroscopy. Few milligrams of bead–powder were pressed in order to obtain a thin tablet, subsequently dried under N₂ flux and analysed in the 600–4000 cm⁻¹ range.

Ellman’s test. The presence of the SH functionalities, incorporated during the co–condensation synthesis, was evaluated by a chemical test based on the DTNB reagent (5,5’–dithio–bis–[2–nitrobenzoic acid]). The free thiols embedded in the mesoporous framework react with the DTNB molecules, producing the cleavage of the disulphide bond and the release of free TNB⁻² anions, which in water and at neutral or alkaline pH has a yellow colour, easily detectable measuring the relative optical absorbance at 412 nm. In order to obtain this reaction a specific protocols must be followed, which include the preparation of two working solutions. Solution A: 50 mM sodium acetate and 2 mM DTNB have been dissolved in deionized water. Solution B: 1 M Tris has been dissolved in water and the pH adjusted at 8. Then, 50 µL of solution A, 100 µL of solution B and 840 µL of water have been poured into a 1.5 mL Eppendorf and carefully mixed. The optical absorbance (421 nm) of the as prepared solution has been used to evaluate the background signal. Subsequently, 10 µL of bead powder solution (2 mg/mL in water) were added and incubated for 5, 30 and 60 min (each condition of incubation was evaluated in triplicate). The reaction solution was collected and the optical absorbance measured after the beads separation (centrifugation at 8 g for 3 min). Furthermore, in order to estimate the concentration of free thiols, a standard calibration curve was build analysing the optical density of different concentration of L–cysteine (starting from 1 mM). Each point of the calibration curve was evaluated in triplicate.

Bead–based assay: Pores availability. The free–entrance in the pores framework has been verify by the evaluation of the fluorescein isothiocyanate (FITC) uptake. First, a stock solution of FITC (1 µM) was obtained dissolving the reagent in sodium phosphate buffer at pH 7. Then, 2 mg of bead–powder were incubated overnight with the FITC solution, in order to promote the complete diffusion of the molecules inside the mesoporous framework. Afterwards, the bead–powder was

separated from the solution by centrifugation (8 g 3 min), and washed three times with sodium phosphate buffer. The residual solution was used to evaluate the amount of uptake, comparing the fluorescence intensity of the solution with and without the particles incubation, with the fluorescence spectrometer Perking Elmer LS55. The concentration of the uptake was evaluated using a calibration curve obtained from standard concentration of FITC in sodium phosphate buffer (starting from 1 μM). Considering the high fluorescence intensity, the samples and the calibration solutions were diluted 1:400 just before the spectrofluorometric measurement. The silica beads separated after the FITC incubation were collected and suspended in ethanol (2 mg/mL), few μL of the suspension were used for the optical analysis (fluorescence optical microscope Leica DMLB) of the fluorescence emitted from the FITC molecules adsorbed by the beads.

Bead-based assay: Passivation. Different passivation agents were tested to reduce the background signal, which can derive from non-specific interaction between the silica surface of the beads and the reagents/molecules used during the bead-based assay. An ELISA-like test was used for this purpose, and a specific molecules label with an HRP-enzyme was used to report this event. Herein, the main protocol used for the passivation of the silica and modified silica beads is shown. 2 mg of beads powder was incubated overnight with 500 μL of sodium phosphate buffer (pH 7), the solution was constantly kept under stirring at 400 rpm at 22 $^{\circ}\text{C}$. The beads were separated from the buffer by centrifugation (8 g – 3 min), and incubated with the selected blocking agent, bovine serum albumin (BSA) or cysteine, for 1 h at 22 $^{\circ}\text{C}$ under continuous stirring (400 rpm). Then, the beads were separated by centrifugation (8 g – 3 min) and incubated with 500 μL of streptavidin-HRP (50 $\mu\text{g}/\text{mL}$) in saline sodium citrate (SSC)-tween buffer, for 1 h at 22 $^{\circ}\text{C}$ under continuous stirring (400 rpm). Subsequently, the beads were separated by centrifugation (8 g – 3 min) and washed three times with the SSC-tween buffer. The beads were finally re-suspended (Figure 5.8) in 500 μL of deionized water, 15 μL of them were poured in a 1.5 mL Eppendorf and incubated with 200 μL of TMB substrate. The reaction was blocked after 30 sec adding 200 μL of H_2SO_4 . Then, the reaction solution was separated from the beads by centrifugation (8 g – 3 min) and the relative optical density (OD) was evaluated by the means of a microplate reader Ivymen Optic System at two different wavelengths (450 and 630 nm). Considering

the large number of combination between blocking agent type (BSA and cysteine) and condition of incubation, in this section it is not reported the related list of the possible variations that can be easily evaluated from the experimental section.

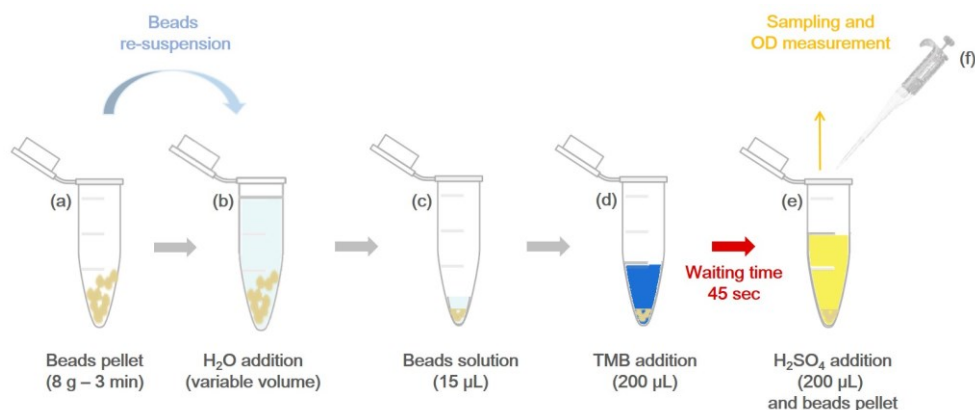


Figure 5.8 Schematic representation of the final steps relative to the ELISA-like test. The beads previously incubated, with specific molecules of interest, were separated from the washing buffer and re-suspended in 500 μL of water (a-b). Subsequently, 15 μL of this solution were sampled and putted in a new Eppendorf (c). Finally, 200 μL of TMB and 200 μL of H_2SO_4 were added (with a waiting time of 45 sec) (d-e). The colorimetric reaction was quantified sampling 200 μL of the final solution (after the beads separation) (f).

Bead-based assay: Immobilization and Hybridization. The same protocol described above for the passivation, was slightly modified and used for the ssDNA probe immobilization and hybridization. In particular, the first step of incubation was modified by incubating the beads with 1 μM of ssDNA probe in sodium phosphate buffer (pH 7). After the overnight incubation the beads were separated from the solution by centrifugation (8 g – 3 min) and washed three times with sodium phosphate buffer. For the probe immobilization tests, the ssDNA was labelled with a biotin molecule that can react with high specificity with Streptavidin-HRP (Str-HRP). The incubation step with the blocking agent was removed and the optimized passivating agent was directly added into the buffer for the Str-HRP incubation (SSC 5X – tween 0.025% – BSA 1%).

For the hybridization test, the immobilization protocol was further modified. In particular, the ssDNA probe without biotin label was incubated O/N, the incubation was followed by some washing steps and finally the ssDNA target was incubated. In particular, 1 μM ssDNA target in SSC 5X – tween 0.025% buffer was incubated for 1 h at 22 $^\circ\text{C}$ (continuously stirring), then the beads were separated by centrifugation (8 g – 3 min) and washed three times with the same buffer. Finally, the beads were

incubated with 50 $\mu\text{g}/\text{mL}$ of Str-HRP in SSC 5X – tween 0.025% – BSA 1% buffer. For the TMB/ H_2SO_4 colorimetric reaction and the OD measurement was used the same protocols show for the passivation tests. Furthermore, for both immobilization and hybridization different condition of: concentration (DNA target between 1000 nM to 0.001 nM / DNA probe from 1 to 10 μM), time of DNA incubation (from 10 min to 60 min), final volume (100 – 250 – 500 – 1000 μL) and time of TMB incubation (45 sec, 2 min and 30 sec or 5 min) were tested, but in order to simplify the reading the related protocols variations can be directly evaluated from the experimental section.

5.8. Microporous silica beads characterization

The as-synthesized mesoporous silica beads were deeply physico-chemically characterized, in order to understand the influence of the different strategies of synthesis on the beads and pores dimensions and on the pores structure and morphology. The BET physical absorption was used to analyse the specific surface area and the pores dimensions as function of the synthesis method. In particular, by means of this technique it has been possible to investigate the influence of the synthesis temperature, the swelling agent (tetramethylbenzidine and Toluene) for the acid-condensation method, and the presence of different type and concentration of organosilanes (APTES and MPTMS) for the co-condensation synthesis.

The mesoporous structure was analysed also from a morphological point of view. The silica beads have been characterized by a scanning electron microscope (SEM). The characterization of the mesoporous structures obtained by co-condensation, due to the addition of different organosilanes, was of great interest in order to select the synthesis method able to preserve pore size and morphology as similar as possible to those obtained for the pristine mesoporous beads.

Following, the microporous beads synthesized by the co-condensation method were chemically analysed in order to qualitatively and quantitatively confirm the presence of additional chemical functionalities. For this purposes, three different techniques were used: TGA, FTIR and Elman's test. The TGA was used to quantify the presence of new chemicals groups as function of different organosilanes type and concentration. The FTIR and the Elman's test were used as qualitative analysis in order to verify the chemical nature of the added functional groups. Furthermore, the

Ellman's test was used as semi-quantitative method for the study of free thiols groups and particular to investigate the availability of these functionalities to small molecules interaction.

5.8.1. Specific surface area and pore size

The preferential method for the synthesis of the mesoporous silica beads was the acidic condensation, as motioned in paragraph 5.7.2 the influence of different synthesis temperatures and swelling agents were taken into account in order to obtain beads with diameter of 3 – 6 μm and pore size greater than 15 nm. Thanks to a combined physical and morphological analysis it has been possible to understand the influence of these parameters.

The BET analysis has revealed that decreasing the synthesis temperature, from room temperature ($R\text{T}=20\text{ }^{\circ}\text{C}$) to $14\text{ }^{\circ}\text{C}$, and fixing the swelling agent (toluene) the particles size increases from few hundred of nanometre to few micrometre (Figure 5.9a and 5.9b). The specific surface area is kept constant ($400\text{--}450\text{ m}^2/\text{g}$) and the absorption isotherm has shown a typical type IV shape, characteristic of mesoporous materials. Further reducing the synthesis temperature to $12\text{ }^{\circ}\text{C}$ the particles size seems to be stabilized and the specific surface area is increased up to $550\text{--}600\text{ m}^2/\text{g}$ (Figure 5.9c) keeping the characteristic isotherm with a type IV shape, which describe the absorption behaviour for the mesoporous materials [158,174].

In order to reduce the risk for the operator, a different swelling agent was tested, in the same synthesis condition. In particular, the TMB agent was used as substitute of toluene. From the BET analysis the increment of the specific surface area seems to be comparable to the $12\text{ }^{\circ}\text{C}$ /toluene synthesis (Figure 5.9d) as well the isotherm shape.

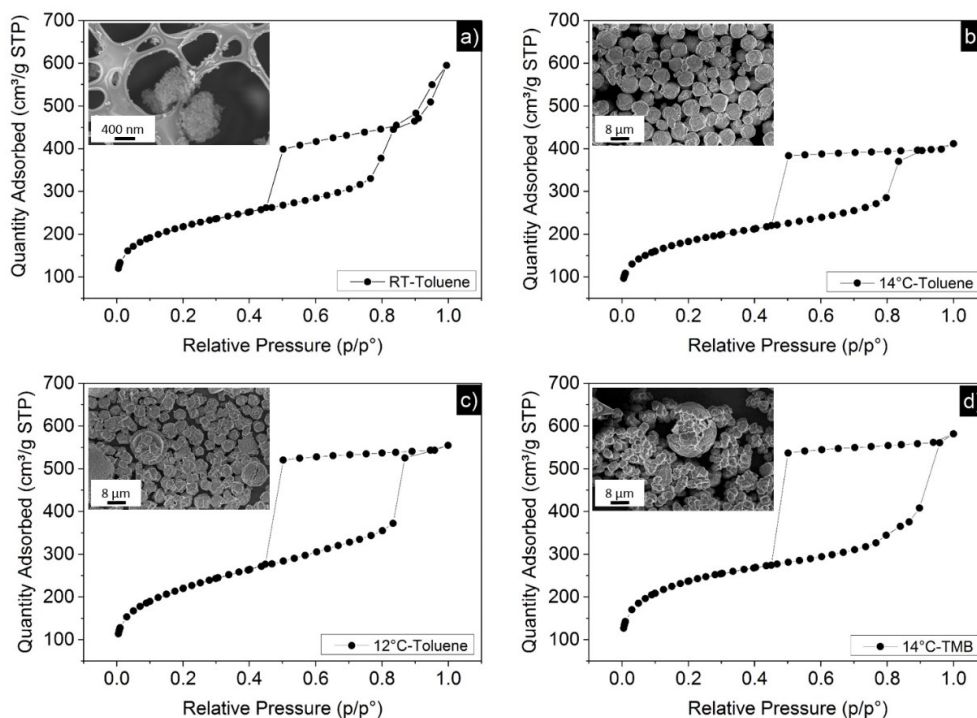


Figure 5.9 BET adsorption/desorption curves characteristic of different mesoporous silica beads: a–b–c) respectively synthesized at 22–14–12 °C using toluene as swelling agent; d) synthesized at 14 °C using TMB as swelling agent. In the inset of each graph are displayed the SEM images of the mesoporous silica beads.

The specific surface area analysis was further supported by the visual analysis of the pore shape and size. As it is possible to observe from Figures 5.10a and 5.10b the pore width distribution seems to be unaffected by the change of the synthesis temperature, from RT to 14 °C. In fact, using toluene as swelling agent for both the synthesis temperature, the pore dimension is centred at about 15 nm. Further decreasing the temperature to 12 °C a temperature threshold is reached, below which the pore dimension is slightly increased (17–20 nm) and the incremental pore volume is doubled respect to the previous synthesis temperature (Figure 5.10c).

Unfortunately, the pore size analysis has revealed that changing the swelling agent, the diameter distribution is no more centred on a specific pore width and the incremental pore volume drastically drop down (Figure 5.10d). Furthermore, as it possible to observe from the SEM images (Insets Figure 5.9a–b–c) the pore morphology and distribution seems to be much more regular for the 14 °C/toluene and 12 °C/toluene synthesis. Observing the SEM image that show the mesoporous structure for the 14 °C/TMB synthesis (Inset Figure 5.10d) the morphology of the pores is not clear, but this can be due also to the SEM image quality.

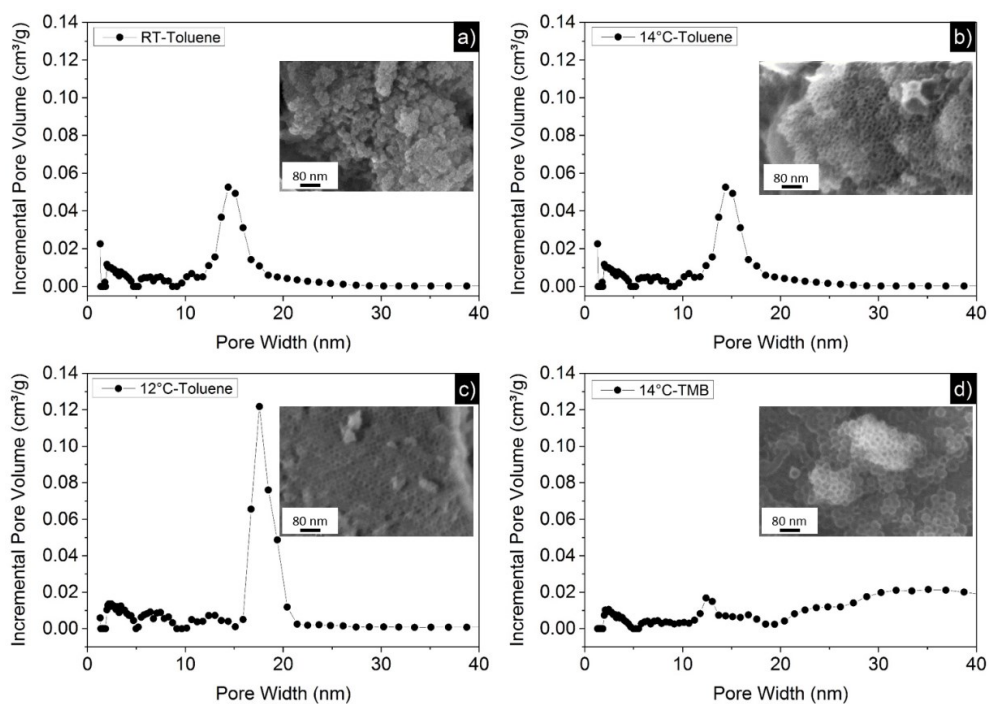


Figure 5.10 BET pore volumes as function of the width distribution, characteristic of different mesoporous silica beads; a–b–c) respectively synthesized at 22–14–12 °C using toluene as swelling agent; d) synthesized at 14 °C using TMB as swelling agent. In the inset of each graph are reported the SEM images of the mesoporous framework obtained from the different synthesis methods.

Considering the results relative to the specific surface area and the pore dimension analysis, the synthesis conditions that allow to reach the desired particles and pore size seem to be the 12 °C/toluene method. These synthesis conditions were applied to the co-condensation method in order to obtain microparticles with the desired dimensions and with specific superficial functional groups. In particular, two different organosilanes were used to obtain three different chemical functionalities on the microparticles surface. The APTES molecule was used to add amine and carboxyl groups, thanks to the possibility to further modify the amine terminal group with a post-treatment with succinic anhydride (SA) in THF reaction solution. A second organosilane, the MPTMS, was used to add thiol groups. For both organosilanes, two different concentrations were tested: 1:50 and 1:25, that represent the organosilane (APTES or MPTMS) to TEOS (silica precursor) ratio. In the following paragraphs, the type and the concentration of organosilane tested for the mesoporous silica beads are stated and resumed in Table 5.1.

<i>Sample name</i>	<i>Silica precursor</i>	<i>Organosilane</i>	<i>Ratio</i>
<i>Bare mSiO₂</i>	TEOS	-	-
<i>50NH₂</i>	TEOS	APTES	1:50
<i>25NH₂</i>	TEOS	APTES	1:25
<i>50COOH</i>	TEOS	APTES+SA	1:50
<i>25COOH</i>	TEOS	APTES+SA	1:25
<i>50SH</i>	TEOS	MPTMS	1:50
<i>25SH</i>	TEOS	MPTMS	1:25

Table 5.1 Resume of the reagents ratio used for the synthesis of the bare and modified mesoporous silica beads; for the co-condensation process the silica precursor/organosilane ratio are specified.

In order to investigate the influence of the organosilane addition on the mesoporous structure, a BET analysis has been conducted and the specific surface area and pore size distribution were compared with the pristine mSiO₂ beads results. In Figures 5.10a and 5.10b the absorption/desorption isotherm behaviour for the APTES and MPTMS modified mSiO₂ beads are reported, respectively. For the samples 50NH₂ and 50COOH (Figure 5.11a) the hysteresis curves show a shape similar to the one characteristic for the pristine mSiO₂ beads, which is representative of the presence of interconnected mesopores with a wide shape and dimension distribution. The specific surface area, computed by the BET analysis, is around 565 and 469 m²/g for the 50NH₂ and 50COOH, respectively. The increment of the APTES concentration, during the co-condensation process, seems to drastically affect the specific surface area and the adsorption/desorption isotherm shape. In particular, observing the hysteresis curves for the sample 25NH₂ and 25COOH (Figure 5.11a) it is possible to hypothesize the presence of interstitial pores due to small particles aggregates. For these samples, the specific surface area has been reduced respectively to 341 and 391 m²/g, as it is possible to observe from Table 5.2. Concerning the addition of the MPTMS molecules, this seems to partially reduce the specific surface area to 560 and 624 m²/g for the 50SH and 25SH samples, respectively. In contrast to what observed for the addition of the APTES molecules, for the MPTMS the specific surface area seems to increase with the organosilane concentration. Furthermore, the hysteresis curve for the 25SH sample shows a shape comparable to mesoporous materials with a narrow distribution of the mesopore size. For the 50SH samples, the hysteresis curve seems to be comparable to the one attained with the pristine mSiO₂ beads, with a wider distribution of pore size and shape.

Comparing the specific surface area values of the different modified mSiO₂ beads with that characteristic of the pristine mSiO₂ (740 m²/g), it seems that the addition of the organosilane, during the co-condensation process, could reduce the overall specific surface area. In general, the increment of the organosilane concentration seems to affect the morphology and size of the pores in a different way depending on the type of the organosilane.

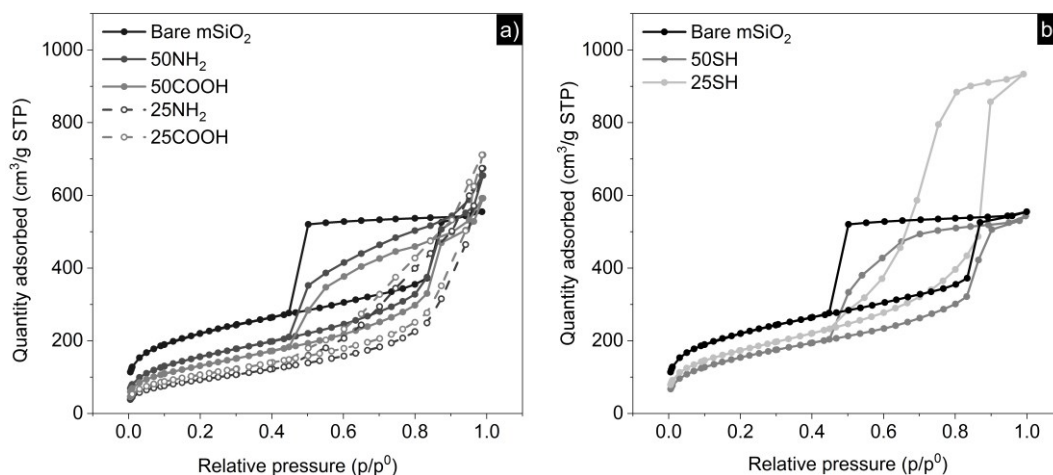


Figure 5.11 BET analysis of different modified mesoporous silica beads; a) comparison of the adsorption/desorption behaviour between the bare and the modified mSiO₂ with two different ratio of APTES (50NH₂ and 25NH₂) and APTES+SA (50COOH and 25COOH). b) comparison of the adsorption/desorption behaviour between the bare and the modified mSiO₂ with two different ratio of MPTMS (50SH and 25SH).

The hypothesis about the modification of the pore size and shape distribution has been confirmed analysing the density functional theory (DFT) computation of the pore width (Figures 5.12a and 5.12b) and the SEM images for the different sample (reported in paragraph 5.8.2). Focusing the attention on the pore width distribution, it is possible to observe the change of the pore width as function of the APTES and MPTMS concentration. For the 25NH₂ and 25COOH samples, the pore size distribution is wider than the one observed for lower APTES concentration and for the pristine mSiO₂ (Figure 5.12a). In particular, the pore distribution seems to be expanded between 16 and 30 nm, but the pore volume is halved respect to the 50NH₂ and 50COOH samples (Figure 5.12a), which show a pore width distribution more similar to the bare mSiO₂ (between 16–20 nm). The expansion of the pore size distribution can be due to the presence of interstitial pores, deriving from the aggregation of small particles and not to a real mesoporous structure.

For what concern the 50SH and 25SH samples, the pore width distribution seem to be kept quite narrow (Figure 5.12b), even if it is possible to identify two different interval: 16 – 20 nm for the 50SH sample and 20 – 27 nm for the 25SH samples. Furthermore, for this last sample the pore volume seems increased if compared to the bare mSiO₂. For the 50SH sample, it is possible to observe a small increment of the pore volume for the pore width from 20 to 27 nm that is not present in the bare mSiO₂ sample.

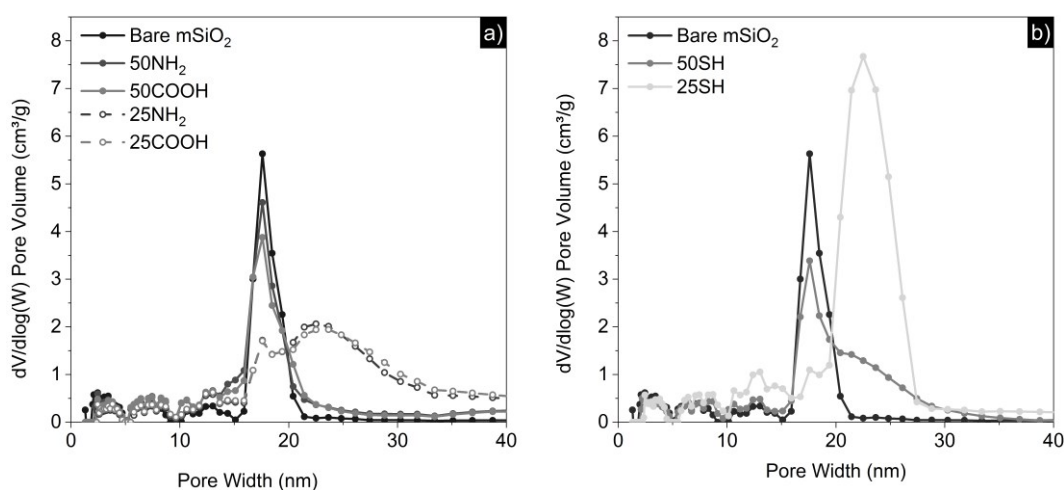


Figure 5.12 BET analysis of different modified mesoporous silica beads; a) comparison of the pore width distribution between the bare and the modified mSiO₂ with two different ratio of APTES (50NH₂ and 25NH₂) and APTES-SA (50COOH and 25COOH), b) Comparison of the pore width distribution between the bare and the modified mSiO₂ with two different ratio of MPTMS (50SH and 25SH).

Sample	BET surface area (m^2/g)	BJH adsorption pore area (m^2/g)	BJH desorption pore area (m^2/g)	DFT pore size (nm)	DFT pore volume (cm^3/g)
mSiO ₂	740.84	501.86	878.30	17.57	5.63
50NH ₂	565.31	486.22	762.28	17.57	4.61
50COOH	479.91	447.36	691.96	17.57	3.88
50SH	560.03	460.21	778.68	17.57	3.39
25NH ₂	341.97	341.08	475.28	22.51	2.06
25COOH	391.60	380.62	511.61	23.65	1.94
25SH	624.97	559.84	935.38	23.65	6.97

Table 5.2 Resume of the BET analysis. In the table are reported the BET surface area, BJH adsorption/desorption pore area and DFT pore size for the bare and modified mesoporous silica beads.

Considering the results obtained from the BET analysis, the mSiO₂ beads modified with MPTMS during the co-condensation process seem to be suitable candidates for the optimization of the DNA-DNA hybridization assay. In particular,

the possibility to maintain a specific surface area similar to the pristine mSiO₂ beads and to improve the pore distribution are interesting features for this purpose.

5.8.2. Morphological analysis

The BET analysis was followed by the morphological study of the silica beads and pores shape, accomplished by means of a scanning electron microscope. From the analysis of Figure 5.13a, the mSiO₂ sample shows an homogeneous particle size distribution, this homogeneity seems to be slightly reduced due to the presence of the organosilanes in the co-condensation process, which can influence the reaction kinetic. In particular, for the modified mSiO₂ beads with APTES (Figure 5.13b) the average particles size has been slightly increased respect to the pristine mSiO₂ sample, with a significant presence of damaged particles. For what concern the MPTMS modified beads, the overall particle dimension has been reduced even if the diameter dispersion seems to be characterized by a lower homogeneity (Figure 5.13c).

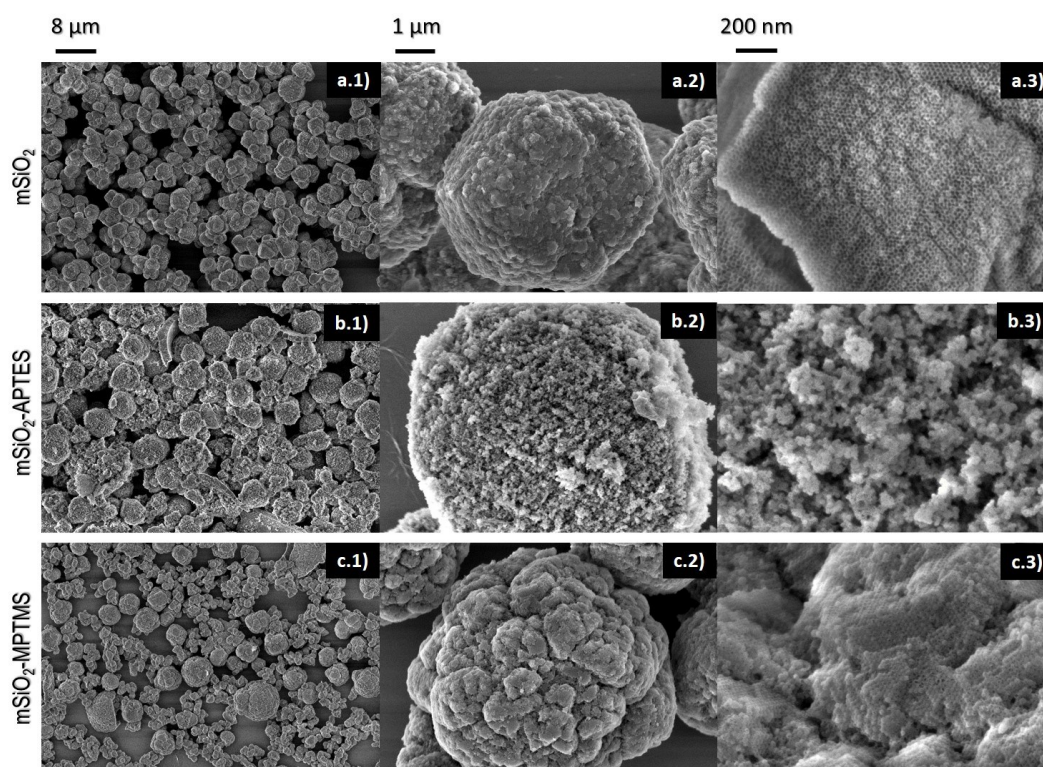


Figure 5.13 SEM images of different modified mSiO₂ beads; a–b–c) are respectively the images relative to bare, APTES modified and MPTMS modified mSiO₂ beads; The series 1–2–3 represent the 5, 50 and 250 kX magnifications.

Analysing the mesostructured network obtained with three different synthesis approaches, the pristine $mSiO_2$ beads show a honeycomb ordered structure (hexagonal cells). The addition of organosilane during the co-condensation synthesis affected the mesostructured in different way depending on the organosilane type. By using APTES, the obtained mesostructured network totally loosed the characteristic ordered hexagonal shape to acquire an interstitial porosity, primarily due to small particles aggregation. Contrary, the addition of MPTMS during the co-condensation seems to preserve the ordered hexagonal structure observed for the pristine $mSiO_2$, even if slightly modified in terms of pore dimensions as already observed from the BET analysis.

Considering the particles dimension observed from the SEM analysis, the beads population was characterized by the means of a granulometer, which allowed the evaluation of the particles size distribution. As it possible to observe from the graph reported in figure 5.14, the beads population shows an average diameter of about 5 μm . The distribution is quite homogeneous and the presence of a shoulder above 10 μm can be mainly due to the formation of aggregate. The small peak between 0.1 and 1 μm can be referred to the presence of a limited presence of particles still at the growing stage.

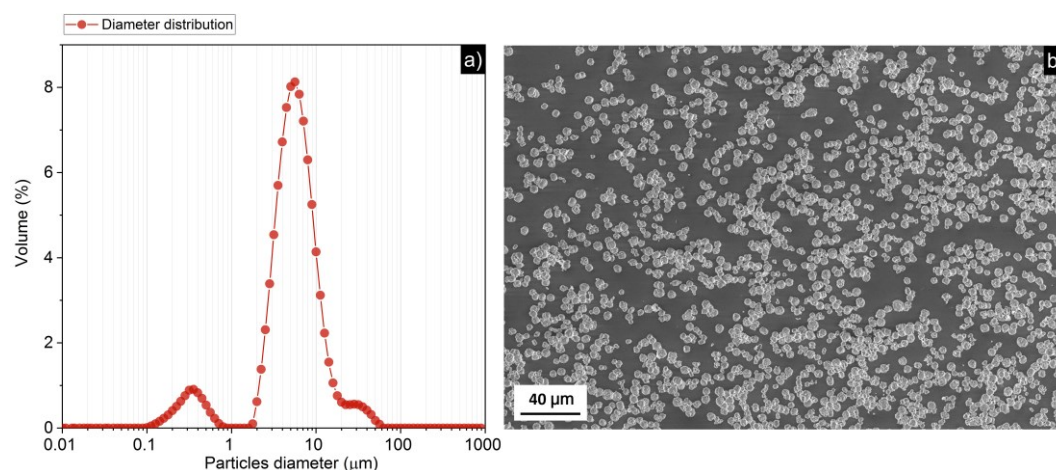


Figure 5.14 Particles size analysis. a) Mesoporous silica beads diameter distribution obtained from the granulometry analysis at 1.3 mbar, b) SEM images (1kX) of the beads population.

5.8.3. Functional group analysis

The effective functional groups incorporation, in the mesoporous structure, has been verified by means of different analyses. In particular, the amount of incorporated

organosilane has been evaluated by TGA, whereas the chemical nature of the functional group has been attributed by FTIR spectroscopy and Elman's test.

In order to understand the effectiveness of the co-condensation as method for the incorporation of new chemical functionalities, the TGA was used to compare the high temperature degradation behaviour of the different mesoporous beads. First of all, the pristine $mSiO_2$ was analysed as reference material (Figure 5.14), the degradation has been subsequently compared to the one observed for the modified silica beads (measurement repeated for two $mSiO_2$ samples). As it is possible to observe from the thermograms in Figure 5.14, the pristine $mSiO_2$ shows the major weight loss around $64.80 - 66.43$ °C, mainly caused by the evaporation of adsorbed water molecules [175]. In the second temperature range ($150 - 600$ °C) a further decrease of the sample weight is observed (about $2.36 - 2.04\%$), probably due to the degradation of synthesis residues.

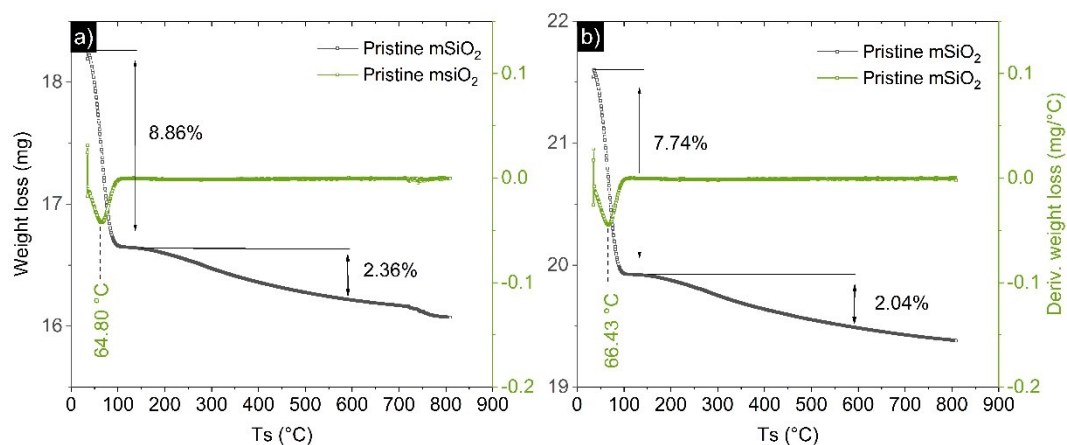


Figure 5.15 TGA of the unmodified mesoporous silica beads; a-b) are the thermograms obtained from two different synthesis batches of pristine $mSiO_2$ beads, respectively.

Analysing the thermograms of the APTES modified $mSiO_2$, the first weight loss is observed up to 150 °C (Figure 5.15a-b). This weight loss is similar for both the APTES concentration and seems to be slightly lower than the one observed for the pristine $mSiO_2$, which is probably due to the reduction of the specific surface area and a different hygroscopic behaviour. A second weight loss can be observed in the $150 - 600$ °C range [176][177]: 15.50% for the APTES 50 and 18.72% for the APTES 25. The difference between the percentages is probably linked to the different amount of organosilane added/incorporated during the co-condensation process. Some of the APTES modified beads were further treated with SA in THF solution,

in order to transform the amine groups into carboxyl groups. The as treated samples were analysed with TGA in order to understand the amount of amine terminal groups converted in carboxyl groups (APTES/SA). Analysing the relative thermograms (Figure 5.15c-d), for both the starting concentration of APTES/SA, three different thermal transitions are observed. The first around 70 °C is mainly caused by the adsorbed water loss as already observed for the previous samples. In this case, the loss is further reduced to 2.03 and 2.12%, this can be due to a further reduction of the specific surface area respect to the APTES modified beads. Differently for what observed for the APTES samples, in the 150 – 600 °C range there are two visible weight losses, one around 207 – 209 °C and a second one around 278 – 281 °C.

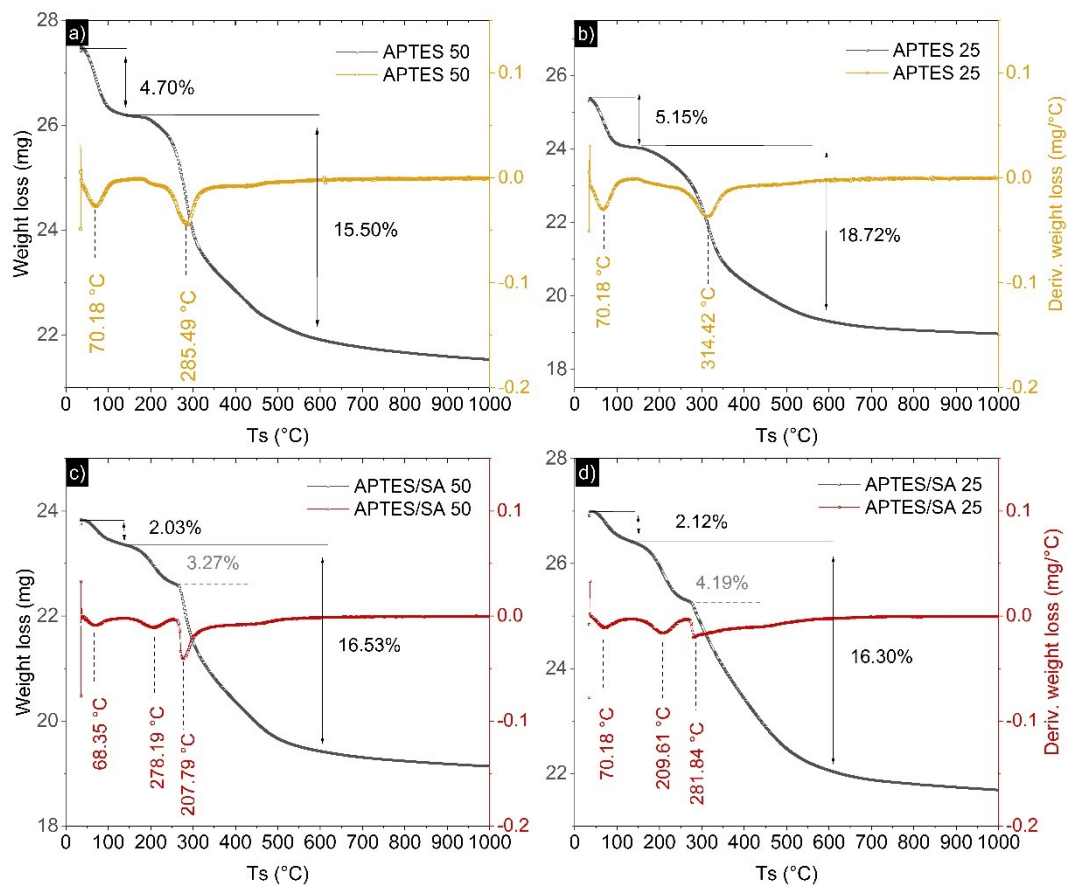


Figure 5.16 TGA of the unmodified mesoporous silica beads; a-b) are respectively the thermograms obtained from two different APTES content (1:50 and 1:25 ratio); c-d) are respectively the thermograms obtained after the modification of the APTES mSiO₂ (1:50 and 1:25 ratio) with succinic anhydride post-synthesis treatment.

The first weight loss has been observed only for the APTES/SA samples, and can represent the amount of amine groups converted in carboxyl groups (subsequently degraded). The loss is respectively 3.27% for the APTES/SA 50 and 4.19% for the

APTES/SA 25. The second weight loss is associated at the same transition temperature observed for the APTES samples. In particular, for the APTES/SA 50 the weight loss percentage (16.53 %) is compatible to that observed for the APTES 50. In the case of the APTES/SA 25, the weight loss (16.30%) is slightly smaller than what observed for the correspondent APTES samples.

Considering true the assumption that attribute to the weight loss at 207 – 209 °C to the degradation of the carboxyl groups, the limited conversion of the APTES terminal amine can be due to two main factors. The concentration of SA could be too low, limiting the conversion, or the SA diffusion through the mesopores could be prevented by the mesoporous structure itself or it requires more time for the diffusion inside the whole bead.

The same TGA test was performed also for the MPTMS modified beads. The thermograms in Figures 5.16a–b show the degradation behaviour for the MPTMS 50 and MPTMS 25 samples. For both it is possible to observe two thermal transitions, the first at low temperature (< 150 °C) corresponding to the loss of the adsorbed water molecules. The second, between 243 – 357 °C, due to the loss of the MPTMS. For these samples, the loss percentage seems to be not directly correlated to the amount of the organosilane added during the co–condensation process. In particular, for the MPTMS 25 the weight loss, of about 7.93%, result to be smaller than the weight loss associated to the MPTMS 50 sample (20.79%). Nevertheless, it is worth to notice that increasing the MPTMS concentration the hydrolysis/condensation rate can be modified disadvantaging the organosilane incorporation.

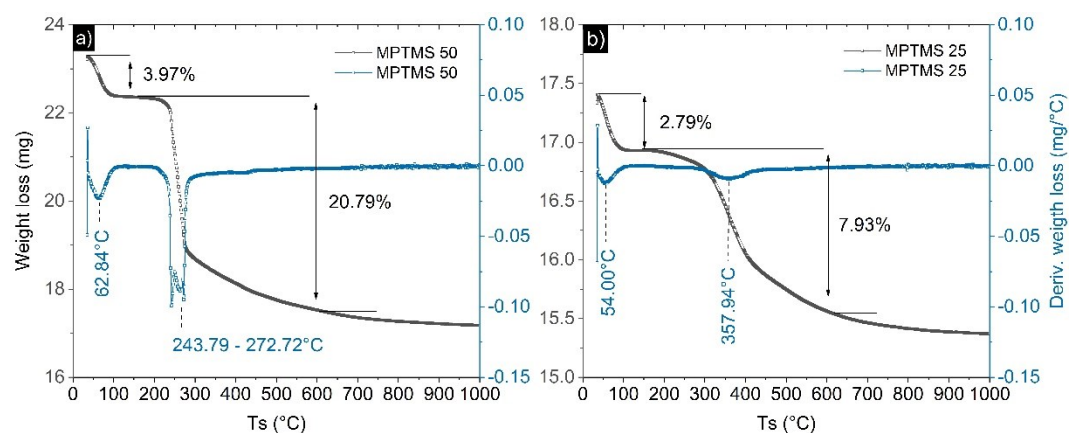


Figure 5.17 TGA of the unmodified mesoporous silica beads; a-b) are respectively the thermograms obtained from two different MPTMS content (1:50 and 1:25 ratio).

The quantity of organosilane incorporated during the co-condensation process has been estimated taking into account the specific surface area, derived from the BET analysis and the milligrams of organosilane lost during the TGA. In the Table 5.3 the organosilane density are resumed for each samples; the values take into account the correction relative the weight loss due to the synthesis residues in the 150 – 600 °C temperature range. This factor has been calculated as the average of the weight loss, at high temperature, for two samples of pristine mSiO₂.

As expected from the trend of the thermograms, the silane density increases with increasing concentration of the organosilane added during the co-condensation process. Only the MPTMS modified beads show an inverted trend and the highest silane density was recorded by the MPTMS 50 sample. The as-calculated silane density can be misleading for the quantification of the amine group conversion to carboxyl group. In fact, the values reported in Table 5.3 shows the silane density related to the total weight loss of the system APTES + SA. Considering the thermal degradation step at 207 – 209 °C (Figures 5.15c-d), it is possible to suppose that the weight loss due to the degradation of the carboxyl groups is 21.76 and 39.21% of the total APTES/SA loss, for the SA 50 and SA 25 samples, respectively. Converting these percentage values, the correspondent carboxyl group densities are $1.72 \cdot 10^{13}$ and $4.48 \cdot 10^{13}$ molecules/cm². If the hypothesis is true, the conversion of the terminal amine group of the APTES modified particles, involved only some of the available groups.

<i>Sample</i>	<i>Specific Area (m²/g)</i>	<i>H₂O adsorbed (mg)</i>	<i>Silane embedded (mg)</i>	<i>Silane density (molecules/cm²)</i>
<i>Pristine mSiO₂</i>	769.0441	1.64	–	–
<i>APTES50</i>	569.8806	1.291	4.3	$1.14 \cdot 10^{14}$
<i>APTES/SA50</i>	493.6356	0.4829	3.94	$7.91 \cdot 10^{13}$
<i>MPTMS50</i>	569.8806	0.9246	4.84	$1.37 \cdot 10^{14}$
<i>APTES25</i>	341.9749	1.3068	4.75	$2.31 \cdot 10^{14}$
<i>APTES/SA25</i>	341.6031	0.5727	4.4	$1.14 \cdot 10^{14}$
<i>MPTMS25</i>	624.9655	0.485	1.38	$3.57 \cdot 10^{13}$

Table 5.3 Evaluation of the silane molecules embedded as function of the specific area of bare and modified mesoporous silica beads.

Two different strategies were used in order to confirm the incorporation of the APTES (or APTES/SA) and the MPTMS molecules in the mesoporous structure of the silica beads. Concerning the modification with APTES and APTES/SA, the

presence of the amine and carboxyl group was verified by the means of the FTIR analysis (Figure 5.17a-b). The characteristic Si-O-Si stretching, related to the silica matrix and the condensation of organosilane (APTES) are clearly visible in the region comprised between 1000–1250 cm^{-1} . The CH_2 stretching ($\nu\text{C-H}_2$), due to the backbone of the siloxane, are identified by the peaks at 2800–2980 cm^{-1} (Figure 5.17c). The presence of the primary amine bending ($\delta\text{N-H}$) at 1614–1617 cm^{-1} confirms the incorporation of the APTES molecules during the co-condensation process.

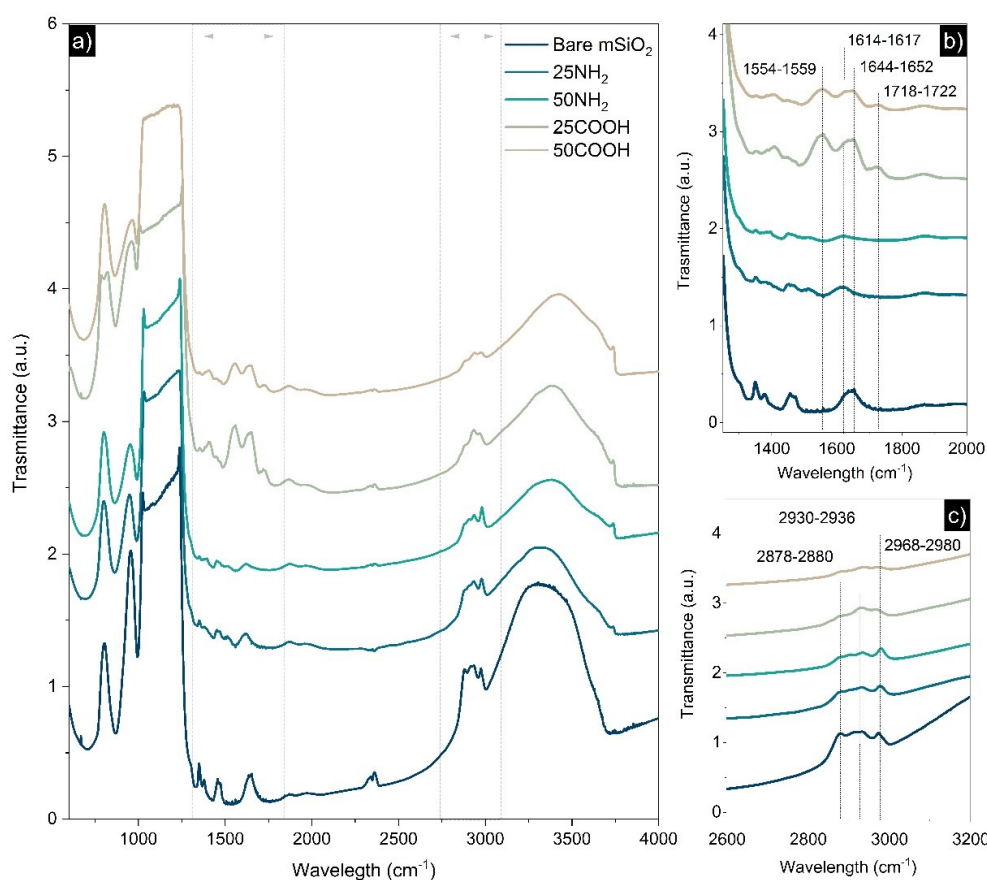


Figure 5.18 FTIR spectra a) of bare and APTES or APTES/SA modified mSiO_2 beads; b-c) magnification of the FTIR peaks related to the amine and carboxyl functionalities and to the siloxane framework, respectively.

Unfortunately, the stretching of the primary amine resulted not clearly visible due to the overwhelming of the broad peak relative to the hydroxyl group stretching ($\nu\text{O-H}$) at 3400–3700 cm^{-1} . The secondary amide stretching ($\nu\text{C=O}$) at 1644–1652 cm^{-1} is representative of the effective reaction of the NH_2 terminal group, characteristic for the APTES modified beads, with the SA molecule. The $\nu\text{O-H}$ shows a reduced intensity for the APTES and APTES/SA modified samples, whereas the $\nu\text{C=O}$ is not present in the APTES samples, as expected. The effective covalent

bonding between the primary amine, of the APTES molecules, with succinic anhydride is further confirmed by the stretching of the C=O dimer H-bonded (terminal carboxyl acid) at 1718–1722 cm^{-1} .

Furthermore, the $\delta\text{N-H}_2$ is drastically reduced and the $\delta\text{N-H}$ (secondary amine bending) appear as proof of the amide bonding formation. As it is possible to observe from Figure 5.17b, there is a decrement of the peaks corresponding to the $\delta\text{N-H}$ and $\delta\text{O-H}$ as function of the concentration of the modified APTES/SA 50 respect to the APTES/SA 25. The same behaviour is observed also for the characteristic $\delta\text{N-H}_2$ of the APTES modified beads.

A few peaks correspondent to some ethoxy moieties are visible in the region comprised between 1390–1440 cm^{-1} , their presence is probably due to the incomplete siloxane condensation or to the presence of non-hydrolyzed APTES.

The effective incorporation of the MPTMS in the mesoporous matrix was verified by means of the Elman's test. This was preferred to the standard FTIR analysis because the aliphatic thiol stretching generally present a very low intensity peak at 2500–2580 cm^{-1} . The Elman's test allows the direct quantification of free sulfhydryl group at neutral pH. The Elman's reagent reacts specifically only with the free thiol group and the reaction is characterized by a high molar extinction and very short response time. As it is possible to observe in Figure 5.18, the amount of available thiol functionalities is lower than the total amount of MPTMS incorporated during the co-condensation process. The molecule density was computed taking as reference the calibration curve of known concentration of L-Cysteine that was used as reference thanks to the quantification of its characteristic thiol functionality. In order to avoid an underestimation of the bonded DTNB molecules, the quantification has been evaluated testing three different reaction times: 5 – 30 – 60 minutes. The variation of the density values between these conditions is limited to a small range and also the negative controls (pristine mSiO_2) show a relative increase of the signal increasing the reaction time.

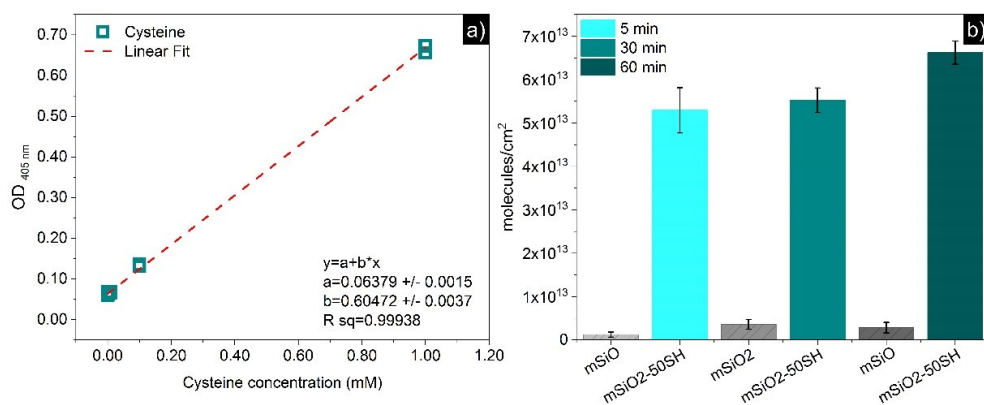


Figure 5.19 Ellman's test a) Cysteine standard calibration curve used for the quantification of the unknown amount of SH functionalities; b) molecules density of SH functionalities for the MPTMS modified mSiO₂ beads, the time of incubation with the DTNB reagent was varied in the 5 – 60 min range.

There is a slight difference between quantification of the incorporated thiol functionalities, evaluated by TGA ($1.37 \cdot 10^{14}$ molecules/cm²), or by Ellman's test ($6.62 \cdot 10^{13}$ molecules/cm²). This can be mainly due to different phenomena. For instance, the structure of the mesopores can block the diffusion of the molecules into the whole internal area of the microbeads. Furthermore, the TGA cannot completely distinguish between the weight loss due to MPTMS chemically incorporated and synthesis residues.

Considering the results obtained by the physico-chemical analysis of the modified mesoporous beads, the MPTMS samples has been chosen as preferential substrate for the DNA-DNA hybridization assay. The addition of this organosilane during the co-condensation synthesis seems to keep the specific surface area close to that characteristic for the pristine mSiO₂ beads. Furthermore, the superficial free thiol groups allow the usage of a simple reaction chemistry for the immobilization of the DNA probe. In fact, modifying the 5' terminal of the DNA sequence with a thiol group and adjusting the pH of the reaction it is possible to easily immobilize the probe via disulphide bond formation.

5.9. Optimization of the DNA hybridization assay

The optimization of the DNA-DNA hybridization assay was conducted starting from the evaluation of the pores availability and the thiol group reactivity. In the previous paragraph, the physico-chemical properties of the MPTMS modified particles were tested, in particular the presence and the amount of the thiol functionalities was quantified by the means of the Elman's test and the TGA,

respectively. In order to understand the correlation between the incorporated thiol functionalities and their effective accessible amount, a preliminary FITC conjugation assay was performed and the results for the MPTMS 50 and MPTMS 25 samples were compared.

The optimization of the DNA–DNA hybridization assay was conducted by means of a modified ELISA–like protocol, exploiting the conjugation of the DNA sequences with a biotin molecule to quantify both the probe immobilization and the hybridization event. Indeed, thanks to biotin, the presence of the DNA sequences could be easily detected via biotin–streptavidin–HRP interaction. First, the non-specific adsorption, due to the mesoporous structure of the beads, was studied testing different passivation agents (BSA and Cysteine) and different incubation conditions. Once the non-specific adsorption was reduced, the optimization of the DNA–DNA hybridization test started with the analysis of the influence of the passivation agent on the probe immobilization and hybridization. In order to lower the limit of detection, different assay procedures were tested: in particular, the DNA probe concentration was optimized to reach the maximum efficient assembly on the mesoporous surface. The volume and the time of probe incubation were changed in order to understand how this could influence the kinetics of probe immobilization.

A broad range of target concentrations was tested (1 μ M to 0.1nM) in order to quantify the LOD reachable with this ELISA–like detection method. Furthermore, the final volume used for the microbeads suspension and the time of reaction of the TMB substrate were tested in order to further increase the ability to detect low concentration of the DNA target.

5.9.1. Evaluation of the pores availability

The effective access inside the mesoporous structure and the availability of the thiol functionalities were tested by means of a FITC conjugation assay. The high chemical reactivity between the isothiocyanate terminal group (FITC molecule) and the terminal thiol functionalities on the MPTMS beads was exploited for this purpose. The conjugation test was repeated three times in order to check the homogeneity of the MPTMS beads synthesis and the amount of conjugated FITC was evaluated by fluorescence spectrometry evaluating the decrement of the fluorescent signal as function of three different beads samples (Figure 5.19). In order

to avoid the saturation of the signal, the starting concentration of the FITC solution was $1 \mu\text{M}$, diluted 1:400 (2.5 nM) for the fluorescence measurement. Comparing the samples MPTMS 50 (50SH) and MTPMS 25 (25SH) to the pristine mSiO_2 beads it is possible to observe an intense reduction of the signal, due to the presence of superficial thiol functionalities. With this analysis the lower MPTMS content of the 25SH samples compared to the 50SH has been also confirmed. The same behaviour was observed from the TGA quantification of the thiol groups and the Elman's test. For the pristine mSiO_2 sample, a slight reduction of the fluorescence intensity is visible compared to that of the starting FITC solution ($1 \mu\text{M}$).

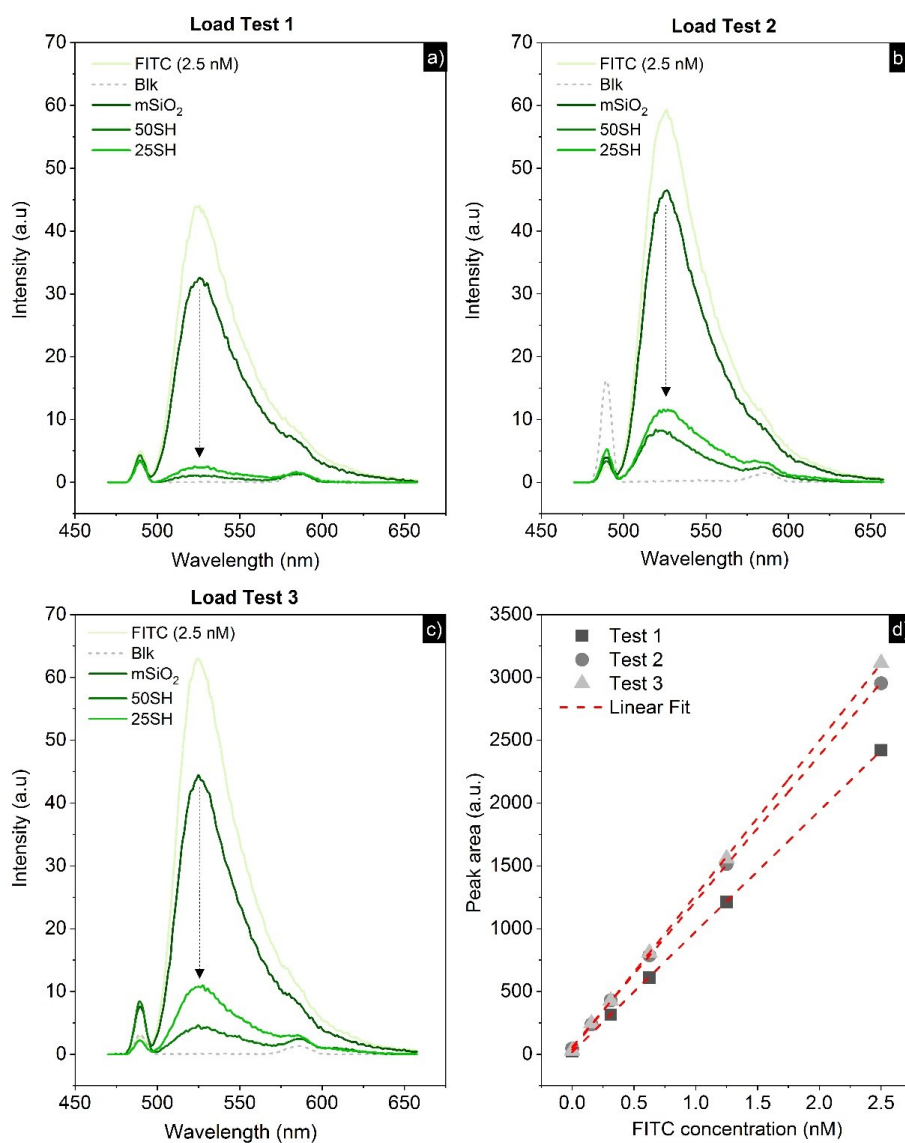


Figure 5.20 FITC uptake test, a-b-c) the reduction of the FITC fluorescence intensity as function of the substrate used (bare and SH modified mSiO_2 beads); the test was performed three times; d) FITC standard calibration curves related to the inter-experiment triplicates.

This indicates a non-specific absorption phenomenon of the FITC molecules into the mesoporous structure of the silica microbeads. In order to avoid any possible contamination, the buffer solution (used for the dilution of the measured solution) was analysed and the fluorescent signal is reported in the graph as dashed line (Figures 5.19a–b–c). The amount of the conjugated FITC was computed by means of a titration curves measured for each test (Figure 5.19d). The peak area correspondent to each FITC concentration was evaluated integrating the fluorescent signal, and the linear fit of the different concentrations was used to determine the unknown FITC concentration for the mSiO₂, 50SH and 25SH samples. The quantity of FITC conjugated molecules is reported in Figure 5.20a as molecule density (molecules/cm²), calculated taking into account the specific superficial area of each samples (measured by the BET analysis, paragraph 5.8.3). The FITC density reported in Figure 5.20a was calculated as the average over the three conjugation tests. The lower amount of thiol functionalities for the 25SH samples is confirmed as mentioned above, but considering the different specific superficial area for the 50SH and 25SH samples, the final FITC density variation is about $3 \cdot 10^{10}$ molecules/cm².

The different fluorescence intensity between the microbead samples has been observed also by means of an optical microscope, equipped with a suitable fluorescence–imaging set-up. From Figures 5.20b–c–d, a different fluorescent emission is appreciable for the three samples, the MPTMS50 shows the higher emission, as expected from the previous experiments. The fluorescent emission of the mSiO₂, due to physically adsorbed or trapped FITC, is only slightly visible.

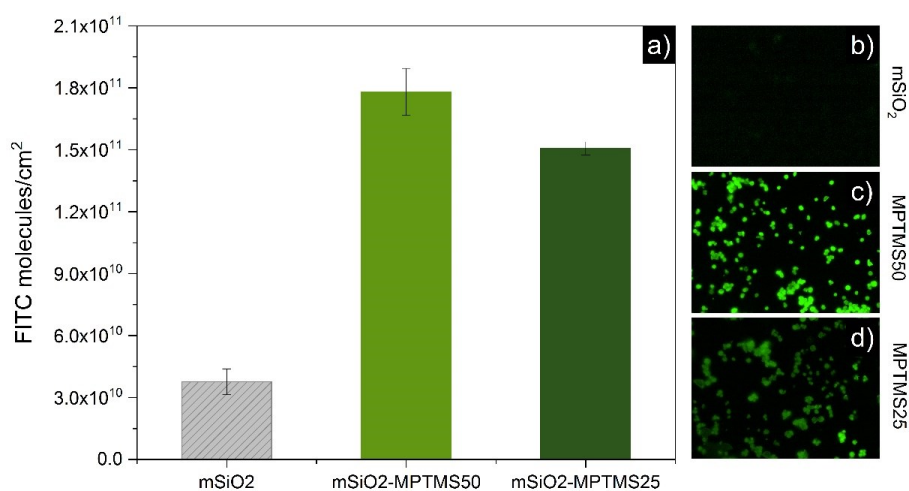


Figure 5.21 Figure 5.19 FITC molecules density a) grafted by the SH functionalities of the modified mSiO₂ beads; b) microscope images of the FITC fluorescence intensity.

The amount of thiol functionalities accessible to the FITC molecules was compared to the amount of functionalities incorporated during the co-condensation process and the results are reported in Table 5.4. As expected, the thiol functionalities reachable by the diffusion of the FITC molecules into the mesoporous structure are smaller than the total amount of functionalities incorporated during the synthesis. This can be due to the structure of the mesopores, not completely interconnected, or to the diffusion kinetic that could require a longer time of incubation.

<i>Sample</i>	<i>SH density (molecules/cm²) TGA</i>	<i>SH density (molecules/cm²) FITC test</i>
<i>MPTMS 50</i>	$1.37 \cdot 10^{14}$	$1.78(\pm 0.11) \cdot 10^{11}$
<i>MPTMS 25</i>	$3.57 \cdot 10^{13}$	$1.51(\pm 0.03) \cdot 10^{11}$

Table 5.4 Comparison of the SH incorporated during the co-condensation synthesis: comparison of TGA and FITC test based quantification.

5.9.2. Optimization of the surface passivation

One of the major problems in the optimization of a biomolecular assay is the false positive rate, which can be correlated with the presence of interference species (like other competitive molecules or the labelling molecules used for the event detection). In order to avoid or reduce this phenomenon, it is fundamental to select the most efficient passivation agent for this purpose.

Considering the surface chemistry of the MPTMS modified beads, the first passivation agent taken into account was the cysteine molecule. In fact, working in an oxidant environment the formation of a disulphide bond can be easily promoted, coupling the terminal thiol of the cysteine molecule and the terminal thiol groups of the MPTMS modified beads. It is well known that the acid dissociation constant (pKa) determines the thiol:thiolate ratio for a given pH value. For L-cystein at a physiological pH of 7.4, the percentage of deprotonated thiol is around 10%, in fact the pKa for this molecule is around 8–8.30. Indeed, in order to increase the percentage of the thiolate anionic form, it is necessary to work at $\text{pH} \geq 8$. Concerning the MPTMS modified beads, the surface charge for any pH value is negative, as reported in the literature from the z-potential studies [178]. For these reasons, it is important to optimize the reaction buffer evaluating the concentration of saline species and surfactant agents. In particular, in order to reduce the repulsion due to the

negative charged surface of the beads, three different buffer were tested: SSC 0.5X/Tween 0.025%, SSC 1X/Tween 0.025% and SSC 5X/Tween 0.05%. Furthermore, to proof the effectiveness of the oxidant environment, three different pH condition were taken into account: 4.5, 6.5 and 8.5.

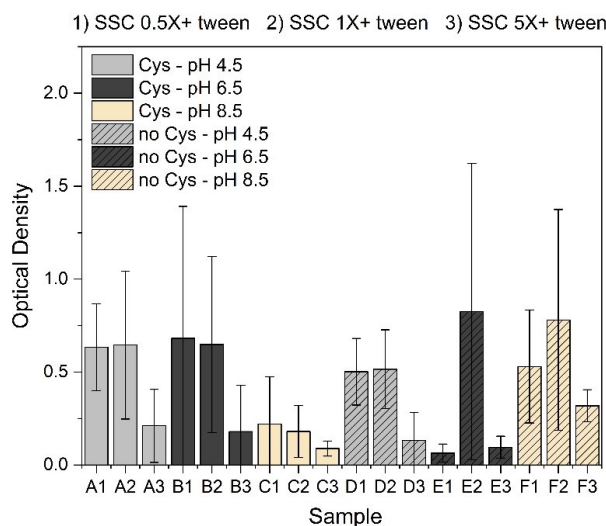


Figure 5.22 Passivation using cysteine as blocking agent: in the graph, the different condition of pH and buffer used for the cysteine incubation are reported.

The results of the cysteine passivation are reported in Figure 5.21 and represent the average OD values calculated over three repetitions for each condition of incubation. The MPTMS modified beads were treated with the possible combinations of buffer composition and pH values, with and without cysteine. Subsequently, the non-specific signal was evaluated incubating the MPTMS beads with Streptavidin-HRP. The semi-quantitative amount of non-specific binding was expressed in OD values and it is depended on the colorimetric reaction due to the conversion of the TMB substrate by the HRP enzyme. As expected, the best passivation effect was obtained at pH value higher than 8.0, and the non-specific signal has been further reduced increasing the SSC concentration in the incubation buffer. The SSC 5X/tween 0.025% seems to ensure the minimum non-specific signal and the minimum standard deviation. The same optimized protocol was tested on the three different microporous beads types: pristine mSiO₂, 50SH and 25SH modified. The passivation test was repeated twice and the results are shown in Figure 5.22a-b. Unfortunately, a poor inter experiment repeatability was observed for both mSiO₂ and 50SH samples. Furthermore, for the 25SH modified beads the OD values

recorded are too high and for these reason the passivation protocol cannot be considered effective.

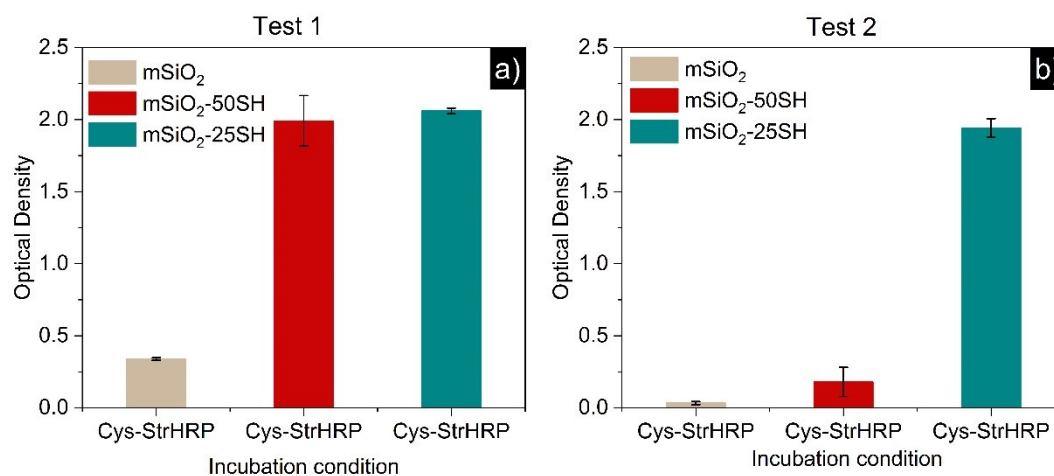


Figure 5.23 Cysteine passivation. Comparison of the effectiveness and reproducibility (a-b) of the passivation test for the bare and SH modified mSiO₂ beads. The value are the average of three repetitions, and the error bars are their standard deviation.

Considering the poor repeatability of the cysteine passivation and the structural properties of the substrate, the protocol was modified including a new passivation agent, the BSA molecule. The low passivation efficiency can be derived from the mesoporous structure that is characterized by high specific negative charged surface area that could attract the streptavidin molecules on the beads surface. The BSA was tested as supporting molecule for the non-specific signal suppression, pre-treating the mesoporous beads with a cysteine/BSA solution. Furthermore, for some of the tested incubation conditions, the BSA molecule was added during the final incubation with Str-HRP to enforce the passivating power. In order to understand, if the combined use of BSA and cysteine was effective, different incubation conditions were tested for the 50SH and 25SH samples. In particular, some of the samples were treated with or without the addition of BSA to the cysteine solution and subsequently incubated with Streptavidin-HRP or Streptavidin-HRP/BSA 1%. As it is possible to observe from the Figure 5.23, all the samples treated with the BSA/cysteine solution show a low non-specific binding signal, further reduced if the Str-HRP incubation was conducted in a BSA 1% buffer. Analysing the 50SH and 25SH samples treated only with cysteine, the non-specific signal was reduced below an OD value of 0.02 for the 50SH samples, only if the samples were finally incubated with Str-HRP in presence of BSA 1%. This behaviour has not been observed for the 25SH samples, where the

total suppression of non-specific signal was experimentally detected only for the samples passivated with the BSA/cysteine solution. Comparing the results obtained from the passivation of the 50SH and 25SH samples, the different passivation strategies seems to be more effective for the MPTMS 50 microbeads, especially for the BSA/cysteine treated samples. In general, the non-specific signals detected for these samples are almost half the signals observed for the 25SH sample.

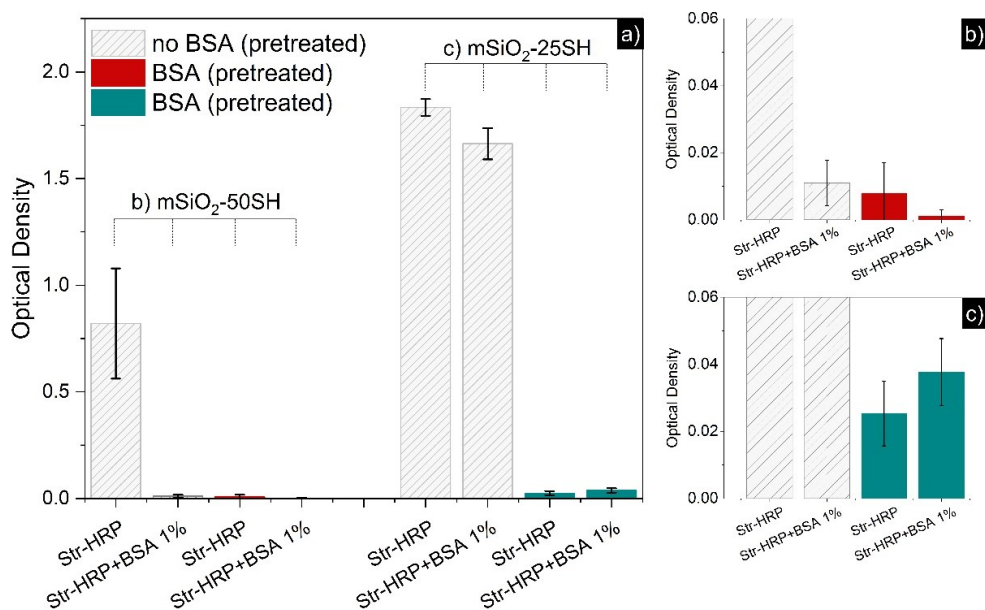


Figure 5.24 Cysteine-BSA coupled passivation. a) Comparison of the effect of the passivation on the 50SH and 25SH modified mSiO₂ beads and relative magnification (b-c).

The samples pre-treated only with cysteine show really high optical density values, this behaviour can be correlated to the secondary interaction induced by the presence of the cysteine molecule. In order to verify this hypothesis a third passivation protocol was tested: in this case, the only passivation agent was the BSA molecules. In particular, the effectiveness of this method was evaluated using BSA as pre-treatment agent and during the incubation of the Str-HRP. The experiment was conducted taking into analysis the 25SH samples, that shown the higher non-specific signals in the presence of cysteine. In Figure 5.24 the results are reported: removing cysteine from the passivation pre-treatment the non-specific signals are decreased below an OD value of 0.25. From this experiment, it is furthermore possible to hypothesize that the presence of BSA only, in the Str-HRP incubation buffer, is sufficient for the non-specific signal suppression. This result is quite interesting from

the optimization point of view, in fact with this new protocol it is possible to totally remove the primary passivation step and therefore to reduce the overall assay time.

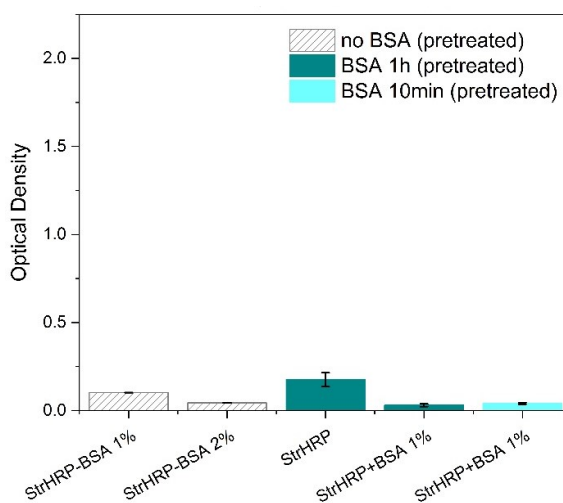


Figure 5.25 BSA passivation. Evaluation of the effectiveness of the BSA used as pre-treatment and/or during the Str-HRP incubation. The OD scale was settled up to 2.25 in order to simplify the comparison with the graph reported in figure 5.23.

5.9.3. Evaluation of the non-specific signal influence on probe immobilization and target detection

Considering the best passivation test results and the amount of available functional groups for the MPTMS modified microbeads, the 50SH samples has been considered as reference samples for the optimization DNA beads assay. The influence of the passivation method on the DNA probe immobilization and hybridization was analysed comparing different incubation conditions. In particular, the second and third passivation tests, executed in the previous paragraph, have been repeated including the DNA probe immobilization step. The DNA probe utilised was a 20bp sequence, modified at the 5' with a thiol group and at the 3' with a biotin-teg, which allows to detect the amount of probe immobilized by the biotin-streptavidin interaction. After the probe immobilization, the samples were treated with or without cysteine and finally incubated with Str-HRP or Str-HRP/BSA 1%; the results are reported in Figure 5.25a-b, respectively. The graph reported in Figure 5.25a confirms the low efficiency of the passivation method with cystein, in particular for the 50SH samples. In fact, the negative controls (without DNA) show a poor suppression of the non-specific signal for the cysteine-treated samples if compared to

the non-treated ones. The cystein passivation seems to be effective only for the pristine mSiO₂ sample; this is quite probably due to a lower non-specific adsorption of the unmodified mesoporous structure and it is not directly associated with the passivation process.

The same experiment has been repeated post-treating the samples with BSA 1%, which was added in the Str-HRP incubation buffer (Figure 5.25b). For this experiment a further negative control was taken into account: the noDNA/no-cysteine. This new condition has been fundamental to analyse the passivation effect of the BSA molecules, added in the Str-HRP incubation process. As it is possible to observe from the inset of the graph, the post-treatment with BSA was able to reduce the non-specific signal without the need of the cystein passivation step. This new protocols seems to be effective for both the substrates (mSiO₂ and 50SH) and compatible with the DNA probe immobilization. Focusing the attention on the DNA/no-cysteine and DNA/cysteine samples, the molecules density detected for this last samples is higher.

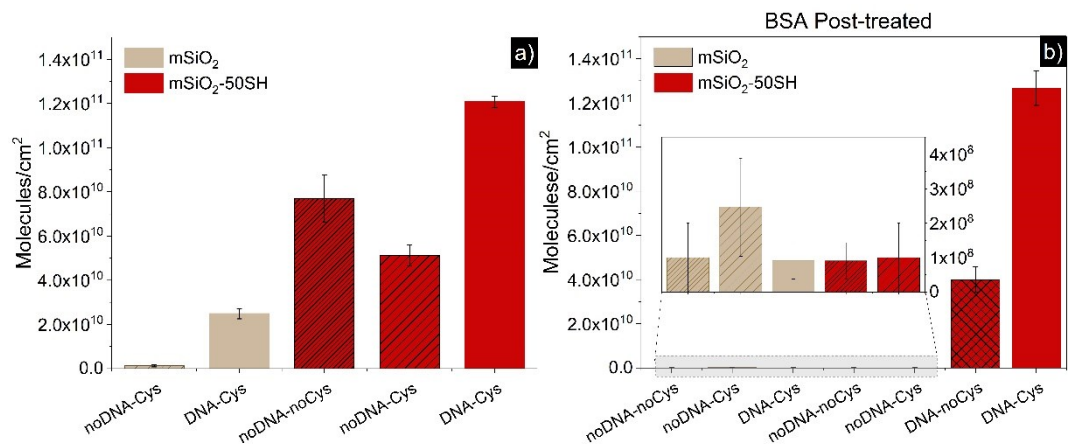


Figure 5.26 Passivation test using two different strategies, the test was conducted with the ssDNA probe immobilized on the beads surface. a) samples of bare and SH modified mSiO₂ beads passivated with cysteine; b) second test conducted by coupling the passivating effect of cysteine with a post-treatment with BSA.

For this reason, the comparison between the passivation test with and without Cysteine was repeated also in the presence of the target DNA sequence. Furthermore, the hybridization test was repeated twice in order to evaluate the repeatability of the protocol. All the samples were treated with BSA only during the Str-HRP incubation, because, as confirmed in the previous paragraph, the passivating effect of the BSA molecule can be considered effective also as post-treatment (after the probe immobilization and hybridization).

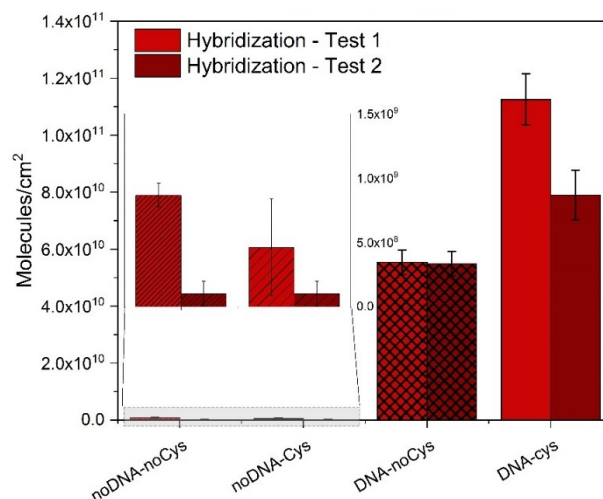


Figure 5.27 Evaluation of the passivation effectiveness if applied to the hybridization **test**, the strategies applied was the treatment with cysteine and subsequently with BSA during the Str-HRP incubation.

Analysing the graph reported in Figure 5.26, it is clear that the presence of the cysteine molecules induce an overestimation of the amount of the DNA target hybridized, even if the cause of that is not completely clear. For this reason, the BSA post-treated protocol has been considered as the more effective way to reduce the non-specific signal without influence the quantification of the hybridization event. Indeed, the amount relative to the target DNA is compatible with the amount of the DNA probe immobilized. Furthermore, this protocol shows a higher intra experiment reproducibility compared to the cysteine passivation method.

5.9.4. Optimization of the DNA target detection

After the optimization of the passivation protocol, which can drastically influence the quantification of the target amount, it has been possible to optimize the parameters that can further improve the DNA target recognition, in terms of limit of detection. In particular, there are different parameters that can be taken into account:

- the DNA probe incubation volume, in order to guarantee the homogenous kinetics of diffusion of the probe molecules into the mesoporous structure of the MPTMS microbeads;
- the DNA probe concentration, which is a critical parameter in terms of surface density on the beads functionalities;
- the time of incubation of the DNA target as a function of the concentration: lowering the target concentration an higher time range can be required to

guarantee the complete diffusion of the molecules into the mesoporous structure;

- the final suspension volume used for the enzymatic reaction, in order to be able to distinguish different concentration of hybridized target;
- the enzymatic reaction time range that should be calibrated over the DNA target concentration, in order to detect the smaller amount of molecules present in solution.

The optimization test has been started considering the main critical aspect for the optimization of a biomolecular assay on mesoporous substrate: the homogeneity of the probe molecule immobilization. In order to guarantee the most effective conditions for a homogeneous molecular diffusion, the time and the volume of the probe incubation have been analysed (Figure 5.27 and 5.28). In particular, the MPTMS beads were incubated with a 1 μM DNA probe solution and the kinetic of absorption was qualitatively monitored by the UV-vis spectrometry. As it is possible to observe from Figure 5.27, in the time range of 30 – 120 min there are some small fluctuations of the absorbed quantity, but the kinetic can be considered almost at the equilibrium comparing this range with the absorption curve of the overnight (O/N) incubation.

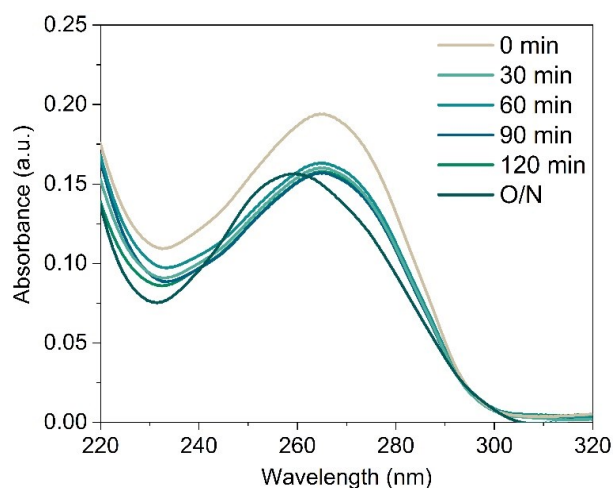


Figure 5.28 Evaluation of the ssDNA immobilization kinetic, the SH modified mSiO_2 beads were incubated with the ssDNA and the kinetic of internalisation was evaluated by means of the UV-spectrometry at different time of incubation.

Taking this last condition as reference, a second experiment was conducted changing the volume used for the DNA probe incubation. Four different conditions have been taken into account (300–200–100–50 μL) and compared with two different

volume of final suspension (Figure 5.28). This volume is the amount of buffer solution added to the beads before the division into smaller volumes that are used to quantify the amount of the DNA probe immobilized (TMB-HRP reaction) (see paragraph 5.7.3 – Figure 5.8). The overall variability of the amount of probe (expressed as molecule density) shows high values independently of the incubation volume, with a lower variation of the total amount of probe for the samples suspended in 1000 μL .

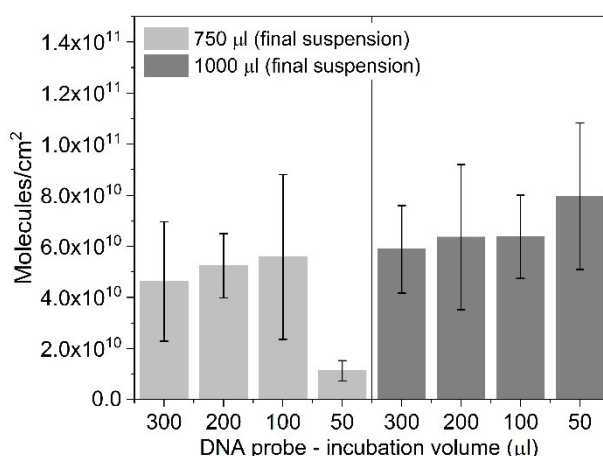


Figure 5.29 ssDNA incubation volume, evaluation of the effect of the incubation volume and final suspension over the immobilized DNA molecules.

Considering the results obtained from the previous optimization tests (time and volume of incubation), the influence of the DNA probe concentration was evaluated through a hybridization test. In fact, analysing the amount of target molecules (incubated at high concentration) it is possible to understand if the density of the probe on the mesostructures is efficient or not. In the graph reported in Figure 5.29, it is possible to observe the correlation between probe concentration (incubation solution) and target molecule density. For probe concentration $\geq 5 \mu\text{M}$, the amount of detected target starts to decrease, this means that the probe assembly is starting to become more and more packed and the intramolecular space has been reduced, lowering the free-space for the hybridization with the target molecule. Considering both the hybridization test n° 2, which shows a lower variability of the tested condition (Figure 5.29), the optimal concentration of DNA probe was evaluated to be in the 2.5 – 5 μM saturation range. This should guarantee the most efficient distribution of the probe sequences on the mesoporous structure.

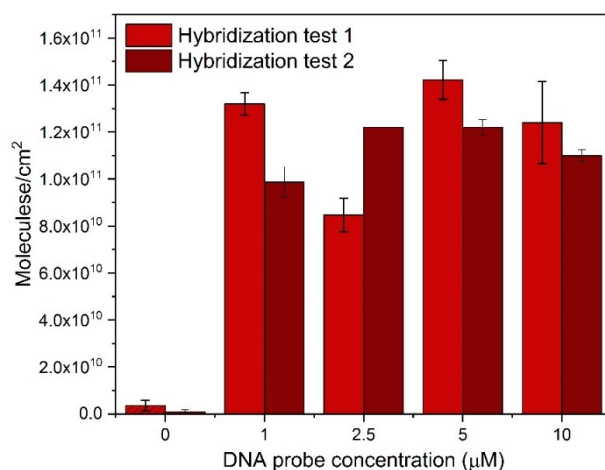


Figure 5.30 Evaluation of the DNA probe concentration, the ability to detect the DNA target was evaluated varying the probe concentration. The test was repeated in order to evaluate the reproducibility.

Once the optimal concentration for the DNA probe immobilization was selected, the ability to detect the DNA target molecules was evaluated, taking into account the influence of the incubation time as preliminary experiment. Two different target solutions were tested: 1 µM and 1 nM, in order to analyse the behaviour for high and low concentration (Figure 5.30a-b). Furthermore, for the 1 nM target incubation, two different times of the TMB–HRP reaction were analysed (45 sec, 5 min).

For the 1 µM DNA target, the time of incubation seems to not influence the amount of hybridization events, and as it is possible to observe from Figure 5.30a the effectiveness of the passivation protocol is confirmed by two negative controls. The noProbe/Target that allowed to evaluate the non-specific signal related to the eventual target adsorption onto the mesoporous bead and the Probe/noTarget, which was essential to confirm the absence of non-specific signal associated with the adsorption of the Str–HRP molecules. These results validate the efficiency of the passivation approach also for the future integration of the bead assay with the SMR.

The same experiment was repeated for the 1 nM DNA target (Figure 5.30b): the choice of two different TMB–HRP reaction times derives from the need to ensure the proper time interval to correctly evaluate the difference between samples incubated with low concentration of target solution. The molecule density fluctuation for the different incubation time (within the same TMB–HRP reaction time) seems to be confined inside a very narrow range. A slighter increase of the molecule density is observed for longer TMB–HRP reaction time. This approach can be useful in order to distinguish very low target concentration if the blank samples

(Probe/noTarget) does not undergo to an extreme increase of the non-specific signal as function of the reaction time.

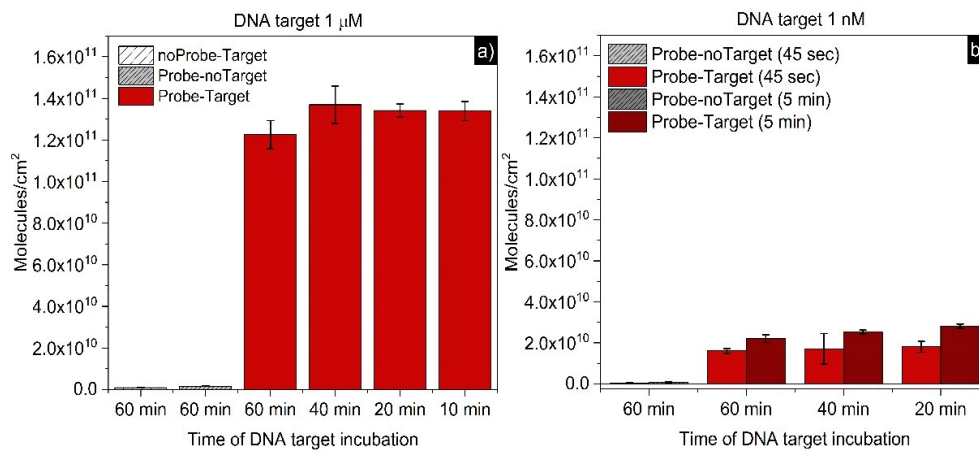


Figure 5.31 Evaluation of the time of incubation for the DNA target detection, considering two different concentration of DNA probe a-b) 1 μ M and 1 nM. Two different TMB-HRP reaction time has been tested: 45 seconds and 5 minutes.

Considering the results relative to the time of incubation and TMB-HRP reaction time, the best condition (60 min of target incubation) has been used to evaluate the dynamic range for the DNA-hybridization test. In Figure 5.31 the amount of hybridized DNA molecules for the target concentration range comprise between 0 – 1000 nM and 0 – 1 nM are reported; in order to compare the results, both the ranges has been evaluated with a TMB-HRP reaction time of 45 seconds.

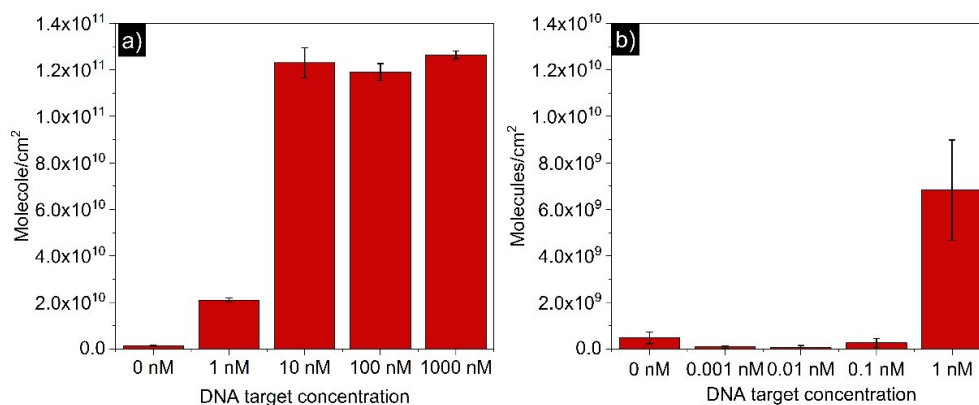


Figure 5.32 Minimum concentration of DNA target detectable, the concentration of incubation was varied in the 0-1000 nM (a) and 0-1 nM (b) ranges.

For the high concentration test (Figure 5.31a) the amount of hybridized DNA target seems to reach a plateau above the concentration of 100 nM. On the contrary,

the low concentration test (Figure 5.31b) seems to undergo a flattening of the response below 1 nM target concentration. Considering these results, it seems that the bead assay shows a poor and a not effective dynamic range. In the case of the low concentration range, the same experiment was repeated increasing the TMB–HRP reaction time. Unfortunately, the same strategy cannot be applied for high concentration, in fact in this case it should be necessary to drastically reduce this parameter, and a further reduction of the reaction time (below 45 sec) can be inconvenient if applied to the manual procedure.

In Figure 5.32a–b is possible to observe the detected amount of DNA target for the low concentration range at higher TMB–HRP reaction time. This strategy seems to be poorly effective on the capability to distinguish the target concentration in the 0.001 – 0.1 nM range. The main observable effect has been the increase of the signal associated with the 1 nM target concentration for both the TMB–HRP reaction time.

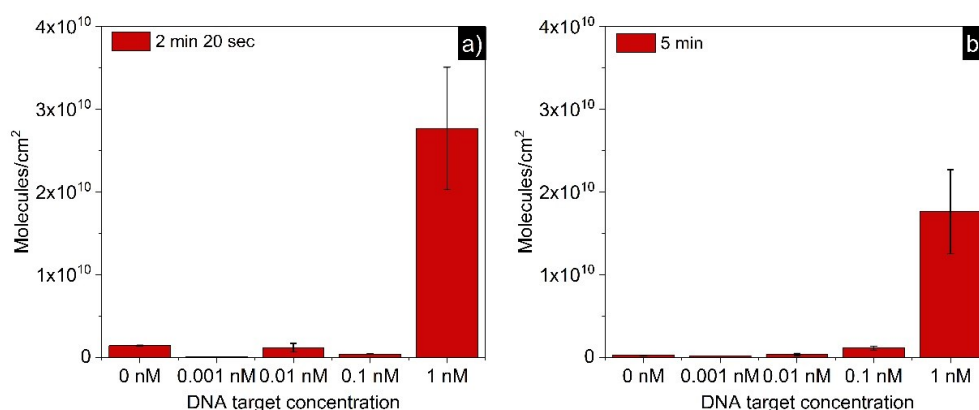


Figure 5.33 Evaluation of the effect of the TMB reaction time, different concentration of DNA target were detected at two reaction: a) 2 min and 20 sec, b) 5 min.

Considering the results obtained from the previous experiments and since the DNA–hybridization assay can be optimized also using a modifiable amount of microparticles, a new intermediate dynamic range has been tested. In particular, the final suspension volume has been changed, trying to concentrate the amount of beads in the volume used during the TMB–HRP reaction. Four different conditions has been tested (100 – 250 – 500 – 1000 μ L). In this case, the target concentrations range (0 – 100 nM) was selected in order to understand the behaviour for medium–low target concentrations. As it is possible to observe from the graphs reported in Figure 5.33, when changing the final volume from 1000 μ L (the reference standard for the previous experiments) to 100 μ L, both the dynamic range and the molecules density

values are increased of one order of magnitude. The relative limit of detection, estimated from 3 times the standard variation of the blank samples ($3SD_{\text{blk}} + \text{blk}$) ranges between 11.97 to 3.13 pM.

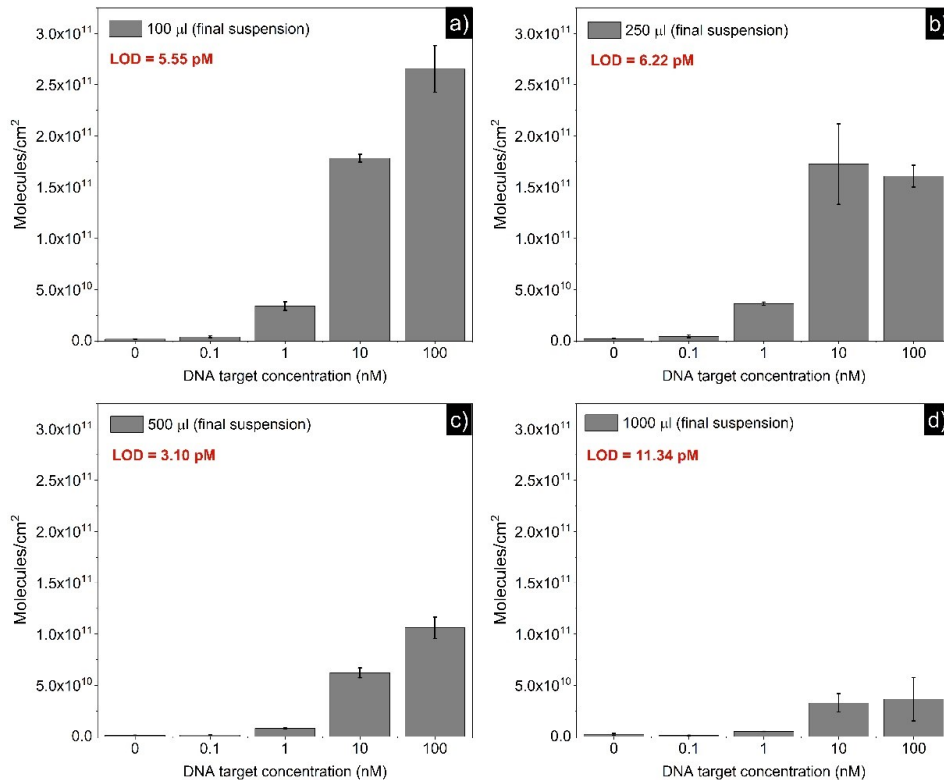


Figure 5.34 Variation of the final suspension volume and evaluation of the related LOD, different volume of the final suspension were tested in order to detect the DNA target incubated in the 0–100 nM range. The limit of detection for each final suspension volume is reported in the graphs.

The dynamic range and the LOD relative to the bead assay could be theoretically further increased with the integration of this protocol with the direct quantification of the amount of target with the SMR platform. In this case, the quantification would be directly executed using the microgravimetric approach, which shows the possibility to reach a minimum detectable mass of 0.09 pg (for the best glass SMR fabricated).

Conclusion

In this work, an innovative process for the rapid fabrication of a monolithic glass SMR has been presented. The process was based on a femtosecond laser writing of a fused silica substrate, enabling the reduction and simplification of fabrication procedures that are normally based on complex and time-consuming approaches. The femtosecond 3D approach has permitted to define in a single-step the suspended resonant structure and the embedded microfluidic channel. In fact, the usage of a transparent substrate opened the possibility to directly focus the laser spot inside the suspended structure, creating the channel path during the same step that involved the SMR geometry definition. SMRs with different dimension of the suspended beam and the embedded channel were tested, and the minimum detectable mass and the responsivity of each platform were estimated. The resonance properties of the as fabricated SMRs have been accurately characterized in terms of frequency, quality factor and Allan's deviation. The best result showed a mass resolution of 0.09 pg and a mass responsivity of 539 Hz/ng, making this glass SMRs competitive with the state of the art resonators. Furthermore, the ability of the SMR to be used as high precision platform for the liquids density detection has been verified, and a density resolution of $1.04 \cdot 10^{-3} \text{ kg/m}^3$ was observed. The performance of the glass SMR could be in principle further improved by reducing their dimensions, in particular decreasing the thickness of the suspended structure, and using a different transparent substrate for the fabrication, like material with higher Young's modulus (i.e. sapphire - Al_2O_3).

Considering the increasing interest in these platforms as high sensitive devices for the study of single cell or single beads, the biosensing capability of the glass SMRs has

been demonstrated by evaluating the presence of *P. fluoresces* (microbial mass) contained in different solutions (variable concentration). The LOD and LOQ calculated from the microgravimetric measurements are respectively 150 and 481 bacteria. The total transparency of our SMR provides the opportunity of monitoring the channel even using an inverted microscope, thus paving the way for a new methodology of integrated optical and microgravimetric characterizations.

In this context, the second part of the thesis work was focused on the optimization of an innovative bioassay based on the use of mesoporous beads as capturing substrates. The idea derived from the possibility to flow and stop the beads directly inside the SMR, thus defining a new label-free sensing system that couple the high capturing ability of the porous beads with the high mass sensitivity of the SMR. In this perspective, the work has been centred on the development of a specific bead-synthesis protocol and on the optimization of the bead-based assay, evaluating the capturing capability and defining the LOD for the labelled-sensing configuration (ELISA-like approach). In fact, the integration of the bead-based assay into the SMR platform requires a deep knowledge of the functionalities of each of them as singular systems. For the SMR platform, this knowledge has been acquired, during the first part of the thesis work, by the careful mechanical characterization and testing the SMRs as density sensors. For what concern the bead-based system, a systematic optimization of a DNA-DNA hybridization assay was conducted. In particular, many different aspects were analysed: the bead-DNA interaction and the evaluation of the non-specific signal influence, which results fundamental for the creation of a label-free sensing approach based on the gravimetric detection of the binding event. The final evaluation of the DNA target detection has been essential for the estimation of the LOD range that can be reached with the bead-based assay. Optimizing the DNA target concentration and the volume involved in the incubation and detection solution the best LOD values range from 11.97 to 3.13 pM. This value could be further improved with the integration of the bead-based system with the SMR, removing the barrier of the labelled sensing.

In order to demonstrate the effectiveness of the envisioned SMR-microbeads system further challenges still need to be overcome. An important constraint, for the implementation of the SMR-microbeads system, is represented by the need of an efficient blocking system able to aggregate a certain number of microbeads in the

middle of the SMR. In fact, the here presented resonator show, in principle, the ability to distinguish the frequency variation due to a single microbead flowing inside the channel. On the other hand, the frequency variation due to the biomolecules loaded on a single bead is far smaller and in order to detect this event it is necessary to sum the signals deriving from a population of beads present at the same time inside the SMR. In this perspective, a first step was done trying to implement a dielectrophoretic system, which is largely used in literature as tool for cells and particles aggregation. Thanks to the compatibility of the SMR fabrication process with standard lithographic techniques, it has been possible to add two coplanar electrodes on top of the suspended beam that act as dielectrophoresis source (Appendix C). Considering the challenges under debate, it is clear that the SMR–microbeads system still needs a deep study and optimization of boundary constraints for its real operative applications.

References

- [1] G.S.W. D.R. Thevenot, K.Toth, R.A.Durst, Electrochemical biosensors : recommended definitions and classification, *Biosens. Bioelectron.* 16 (2001) 121–131.
- [2] A.P.F. Turner, Biosensors: sense and sensibility, *Chem Soc Rev.* 42 (2013). doi:10.1039/c3cs35528d.
- [3] A.F.C.& F.Caruso, Biosensors : recent advances, *Reports Progress Phys.* 60 (1997) 1397–1445.
- [4] D. Ramos, E. Gil-santos, H.D. Tong, C. Van Rijn, Arrays of Dual Nanomechanical Resonators for Selective Biological Detection, *Anal. Chem.* 81 (2009) 2274–2279.
- [5] P. Dextras, K.R. Payer, T.P. Burg, W. Shen, Y.C. Wang, J. Han, S.R. Manalis, Fabrication and characterization of an integrated microsystem for protein preconcentration and sensing, *J. Microelectromechanical Syst.* 20 (2011) 221–230. doi:10.1109/JMEMS.2010.2093563.
- [6] M.M. Modena, Y. Wang, D. Riedel, T.P. Burg, Resolution enhancement of suspended microchannel resonators for weighing of biomolecular complexes in solution., *Lab Chip.* 14 (2014) 342–50. doi:10.1039/c3lc51058a.
- [7] N. Cermak, S. Olcum, F.F. Delgado, S.C. Wasserman, K.R. Payer, M.A. Murakami, S.M. Knudsen, R.J. Kimmerling, M.M. Stevens, Y. Kikuchi, A. Sandikci, M. Ogawa, V. Agache, F. Baléras, D.M. Weinstock, S.R. Manalis, High-throughput measurement of single-cell growth rates using serial microfluidic mass sensor arrays, *Nat. Biotechnol.* 34 (2016) 1052–1059. doi:10.1038/nbt.3666.
- [8] J.L. Arlett, E.B. Myers, M.L. Roukes, Comparative advantages of mechanical biosensors, *Nat. Nanotechnol.* 6 (2011) 203–215. doi:10.1038/nnano.2011.44.
- [9] J.L. Arlett, M.L. Roukes, Ultimate and practical limits of fluid-based mass detection with suspended microchannel resonators, *J. Appl. Phys.* 108 (2010) 1–11. doi:10.1063/1.3475151.
- [10] G. Binnig and C.F. Quate, Atomic Force Microscope, *Phys. Rev. Lett.* 56 (1986). doi:10.1103/PhysRevLett.56.930.
- [11] O. Wolter, J. Greschner, Micromachined silicon sensors for scanning force microscopy, *J. Vac. Sci. Technol. B.* 1353 (2014) 0–5. doi:10.1116/1.585195.
- [12] T.R. Albrecht, S. Akamine, T.E. Carver, C.F. Quate, T.R. Albrecht, S. Akamine, T.E. Carver, C.F. Quate, Microfabrication of cantilever styli for the atomic force microscope, *J. Vac. Sci. Technol. A.* 3386 (2012). doi:10.1116/1.576520.
- [13] T. Thundat, R.J. Warmack, G.Y. Chen, D.P. Allison, T. Thundat, F.L.J. Warmack, G.Y. Chen, D.P. Allison, Thermal and ambient-induced deflections of scanning force microscope cantilevers Thermal and ambient-induced deflections of scanning force

- microscope, *Appl. Phys. Lett.* 2894 (1994) 1–4. doi:10.1063/1.111407.
- [14] T. Thundat, E.A. Wachter, S.L. Sharp, R.J. Warmack, T. Thundat, E.A. Wachter, S.L. Sharp, R.J. Warmack, Detection of mercury vapor using resonating microcantilevers, *Appl. Phys. Lett.* 1695 (1995) 1–4. doi:10.1063/1.113896.
- [15] D. Lange, C. Hagleitner, A. Hierlemann, O. Brand, H. Baltes, Complementary Metal Oxide Semiconductor Cantilever Arrays on a Single Chip : Mass-Sensitive Detection of Volatile Organic Compounds, *Anal. Chem.* 74 (2002) 3084–3095. doi:10.1021/ac011269j CCC.
- [16] R. Berger, E. Delamarche, H.P. Lang, C. Gerber, E. Delamarche, H.P. Lang, C. Gerber, J.K. Gimzewski, E. Meyer, Surface Stress in the Self-Assembly of Alkanethiols on Gold, *Science* (80-.). 276 (2016) 2021–2024.
- [17] J.K.G. J. Fritz, M.K. Baller, H.P. Lang, H. Rothuizen, P. Vettiger, E. Meyer, H.-J. Guntherodt, Ch. Gerber, Translating Biomolecular Recognition into Nanomechanics, *Science* (80-.). 288 (2000) 316–318. doi:doi:10.1126/science.288.5464.316.
- [18] G. Wu, R.H. Datar, K.M. Hansen, T. Thundat, R.J. Cote, A. Majumdar, Bioassay of prostate-specific antigen (PSA) using microcantilevers, *Nature.* 19 (2001) 856–860.
- [19] G. Wu, H. Ji, K. Hansen, T. Thundat, R. Datar, R. Cote, M.F. Hagan, a K. Chakraborty, a Majumdar, Origin of nanomechanical cantilever motion generated from biomolecular interactions., *Proc. Natl. Acad. Sci. U. S. A.* 98 (2001) 1560–1564. doi:10.1073/pnas.98.4.1560.
- [20] K.S. Hwang, S. Lee, S.K. Kim, J.H. Lee, T.S. Kim, Micro- and Nanocantilever Devices and Systems for Biomolecule Detection, *Annu. Rev. Anal. Chem.* (2009) 77–98. doi:10.1146/annurev-anchem-060908-155232.
- [21] S. Ghosh, S. Mishra, R. Mukhopadhyay, Enhancing sensitivity in a piezoresistive cantilever-based label-free DNA detection assay using ssPNA sensor probes, *J. Mater. Chem. B.* 2 (2014) 960–970. doi:10.1039/c3tb21392g.
- [22] N.H. Zhang, Z.Q. Tan, J.J. Li, W.L. Meng, L.W. Xu, Interactions of single-stranded DNA on microcantilevers, *Curr. Opin. Colloid Interface Sci.* 16 (2011) 592–596. doi:10.1016/j.cocis.2011.04.013.
- [23] A.E. Cetin, M.M. Stevens, N.L. Calistri, M. Fulciniti, S. Olcum, R.J. Kimmerling, N.C. Munshi, S.R. Manalis, Determining therapeutic susceptibility in multiple myeloma by single-cell mass accumulation, *Nat. Commun.* 8 (2017). doi:10.1038/s41467-017-01593-2.
- [24] S. Olcum, N. Cermak, S.C. Wasserman, S.R. Manalis, High-speed multiple-mode mass-sensing resolves dynamic nanoscale mass distributions., *Nat. Commun.* 6 (2015) 7070. doi:10.1038/ncomms8070.
- [25] A. Boisen, S. Dohn, S.S. Keller, S. Schmid, M. Tenje, Cantilever-like micromechanical sensors, *Reports Prog. Phys.* 74 (2011). doi:10.1088/0034-4885/74/3/036101.

- [26] E.B. and L.B. F.A. Sandoval, M. Geitner, Resonance frequency shift of strongly heated micro-cantilevers, *J. Appl. Phys.* 234503 (2015). doi:10.1063/1.4922785.
- [27] M. Godin, P.J. Williams, V. Tabard-cossa, O. Laroche, L.Y. Beaulieu, R.B. Lennox, P. Gru, Surface Stress , Kinetics , and Structure of Alkanethiol Self-Assembled Monolayers, *Langmuir*. 20 (2004) 7090–7096.
- [28] M. Calleja, P.M. Kosaka, Á. San Paulo, J. Tamayo, Challenges for nanomechanical sensors in biological detection, *Nanoscale*. 4 (2012) 4925. doi:10.1039/c2nr31102j.
- [29] J. Mertens, C. Rogero, M. Calleja, D. Ramos, J.A. Martín-Gago, C. Briones, J. Tamayo, Label-free detection of DNA hybridization based on hydration-induced tension in nucleic acid films., *Nat. Nanotechnol.* 3 (2008) 301–307. doi:10.1038/nnano.2008.91.
- [30] Z. Hu, T. Thundat, R.J. Warmack, Z. Hu, T. Thundat, R.J. Warmack, Investigation of adsorption and absorption-induced stresses using microcantilever sensors Investigation of adsorption and absorption-induced stresses using microcantilever sensors, *J. Appl. Phys.* 427 (2012). doi:10.1063/1.1378333.
- [31] B. Ilic, H.G. Craighead, S. Krylov, W. Senaratne, C. Ober, Attogram detection using nanoelectromechanical oscillators, 3694 (2004). doi:10.1063/1.1650542.
- [32] Y.T. Yang, C. Callegari, X.L. Feng, K.L. Ekinici, M.L. Roukes, Zeptogram-Scale Nanomechanical Mass Sensing, (2006) 10–13.
- [33] T.P. Burg, A.R. Mirza, N. Milovic, C.H. Tsau, G. a. Popescu, J.S. Foster, S.R. Manalis, Vacuum-packaged suspended microchannel resonant mass sensor for biomolecular detection, *J. Microelectromechanical Syst.* 15 (2006) 1466–1476. doi:10.1109/JMEMS.2006.883568.
- [34] T.P. Burg, J.E. Sader, S.R. Manalis, Nonmonotonic energy dissipation in microfluidic resonators, *Phys. Rev. Lett.* 102 (2009) 1–4. doi:10.1103/PhysRevLett.102.228103.
- [35] C.A. Van Eysden, J.E. Sader, C.A. Van Eysden, J.E. Sader, Frequency response of cantilever beams immersed in viscous fluids with applications to the atomic force microscope : Arbitrary mode order Frequency response of cantilever beams immersed in viscous fluids with applications to the atomic force microscope :, *J. Appl. Phys.* 101 (2007) 44908–0–11. doi:10.1063/1.2654274.
- [36] C. Ricciardi, G. Canavese, R. Castagna, I. Ferrante, A. Ricci, S.L. Marasso, L. Napione, F. Bussolino, Integration of microfluidic and cantilever technology for biosensing application in liquid environment, *Biosens. Bioelectron.* 26 (2010) 1565–1570. doi:10.1016/j.bios.2010.07.114.
- [37] M. Melli, G. Scoles, M. Lazzarino, Fast detection of biomolecules in diffusion-limited regime using micromechanical pillars, *ACS Nano*. 5 (2011) 7928–7935. doi:10.1021/nn202224g.
- [38] M.S. Weinberg, C.E. Dubé, A. Petrovich, A.M. Zapata, Fluid Damping in Resonant Flexural Plate Wave Device, *J. Microelectromechanical Syst.* 12 (2003) 567–576.
- [39] G. Palmara, A. Chiadò, R. Calmo, C. Ricciardi, Succinic anhydride functionalized microcantilevers for protein immobilization and quantification, *Anal. Bioanal.*

- Chem. (2016) 7917–7926. doi:10.1007/s00216-016-9920-2.
- [40] T.P. Burg, S.R. Manalis, Suspended microchannel resonators for biomolecular detection, *Appl. Phys. Lett.* 83 (2003) 2698. doi:10.1063/1.1611625.
- [41] D.J.B. and Q.L. H. Sun, T. Olsen, J. Zhu, J. Tao, B. Ponnaiya, S.A. Amudson, A bead-based microfluidic approach to integrated single-cell gene expression analysis by quantitative RT-PCR, *RSC Adv.* 5 (2014) 4886–4893. doi:10.1039/C4RA13356K.
- [42] H. Suárez, A. Gámez-valero, R. Reyes, S. López-martín, M. Josefa, J.L. Carrascosa, C. Cabañas, F.E. Borràs, M. Yáñez-mó, A bead-assisted flow cytometry method for the semi-quantitative analysis of Extracellular Vesicles, *Sci. Rep.* (2017) 1–11. doi:10.1038/s41598-017-11249-2.
- [43] R.A. Barton, B. Ilic, S.S. Verbridge, B.R. Cipriany, J.M. Parpia, H.G. Craighead, Fabrication of a nanomechanical mass sensor containing a nanofluidic channel, *Nano Lett.* 10 (2010) 2058–2063. doi:10.1021/nl100193g.
- [44] A. De Pastina, D. Maillard, L.G. Villanueva, Fabrication of suspended microchannel resonators with integrated piezoelectric transduction, *Microelectron. Eng.* 192 (2018) 83–87. doi:10.1016/j.mee.2018.02.011.
- [45] M.F. Khan, S. Schmid, Z.J. Davis, S. Dohn, A. Boisen, Fabrication of resonant micro cantilevers with integrated transparent fluidic channel, *Microelectron. Eng.* 88 (2011) 2300–2303. doi:10.1016/j.mee.2011.02.096.
- [46] M.G. Von Muhlen, N.D. Brault, S.M. Knudsen, S. Jiang, S.R. Manalis, Label-free biomarker sensing in undiluted serum with suspended microchannel resonators, *Anal. Chem.* 82 (2010) 1905–1910. doi:10.1021/ac9027356.
- [47] S.M. Knudsen, M.G. Von Muhlen, S.R. Manalis, Quantifying particle coatings using high-precision mass measurements, *Anal. Chem.* 84 (2012) 1240–1242. doi:10.1021/ac300034r.
- [48] S. Schmid, L.G. Villanueva, M.L. Roukes, Fundamentals of nanomechanical resonators, 2016. doi:10.1007/978-3-319-28691-4.
- [49] A. Boisen, S. Dohn, S.S. Keller, S. Schmid, M. Tenje, Cantilever-like micromechanical sensors, *Reports Prog. Phys.* 74 (2011) 36101. doi:10.1088/0034-4885/74/3/036101.
- [50] R. Abdolvand, B. Bahreyni, J.E.Y. Lee, F. Nabki, Micromachined resonators: A review, *Micromachines.* 7 (2016). doi:10.3390/mi7090160.
- [51] G. Canavese, A. Ricci, G.C. Gazzadi, I. Ferrante, A. Mura, S.L. Marasso, C. Ricciardi, Resonating Behaviour of Nanomachined Holed Microcantilevers, *Sci. Rep.* 5 (2015) 3–8. doi:10.1038/srep17837.
- [52] X.M.H. Huang, X.L. Feng, C.A. Zorman, M. Mehregany, M.L. Roukes, VHP, UHF and microwave frequency nanomechanical resonators, *New J. Phys.* 7 (2005). doi:10.1088/1367-2630/7/1/247.
- [53] D.I. Bradley, R. George, A.M. Guénault, R.P. Haley, S. Kafanov, M.T. Noble, Y.A. Pashkin, G.R. Pickett, M. Poole, J.R. Prance, M. Sarsby, R. Schanen, V. Tsepelin, T. Wilcox, D.E. Zmееv, Operating Nanobeams in a Quantum Fluid, *Sci.*

- Rep. 7 (2017) 1–8. doi:10.1038/s41598-017-04842-y.
- [54] B.A. Bircher, R. Krenger, T. Braun, Automated high-throughput viscosity and density sensor using nanomechanical resonators, *Sensors Actuators, B Chem.* 223 (2016) 784–790. doi:10.1016/j.snb.2015.09.084.
- [55] S. Yamada, S. Schmid, A. Boisen, Resonant photothermal IR spectroscopy of picogram samples with microstring resonator, 2013 Transducers Eurosensors XXVII 17th Int. Conf. Solid-State Sensors, Actuators Microsystems, TRANSDUCERS EUROSENSORS 2013. (2013) 846–849. doi:10.1109/Transducers.2013.6626899.
- [56] N.E. Weckman, A.A. Seshia, Reducing dissipation in piezoelectric flexural microplate resonators in liquid environments, *Sensors Actuators, A Phys.* 267 (2017) 464–473. doi:10.1016/j.sna.2017.10.035.
- [57] Y. Jia, S. Du, A.A. Seshia, Twenty-Eight Orders of Parametric Resonance in a Microelectromechanical Device for Multi-band Vibration Energy Harvesting, *Sci. Rep.* 6 (2016) 1–8. doi:10.1038/srep30167.
- [58] A.M. Eriksson, M. V. Voinova, L.Y. Gorelik, Nonresonant high frequency excitation of mechanical vibrations in a graphene based nanoresonator, *New J. Phys.* 17 (2015) 1–6. doi:10.1088/1367-2630/17/3/033016.
- [59] A. Labuschagne, N.F.J. van Rensburg, A.J. van der Merwe, Comparison of linear beam theories, *Math. Comput. Model.* 49 (2009) 20–30. doi:10.1016/j.mcm.2008.06.006.
- [60] Microcantilever Transducers : A New Approach in Sensor Technology, (n.d.).
- [61] D. V. Land, A.P. Levick, J.W. Hand, The use of the Allan deviation for the measurement of the noise and drift performance of microwave radiometers, *Meas. Sci. Technol.* 18 (2007) 1917–1928. doi:10.1088/0957-0233/18/7/018.
- [62] D.W. Allan, Should the Classical Variance Be Used As a Basic Measure in Standards Metrology?, *IEEE Trans. Instrum. Meas.* IM-36 (1987) 646–654. doi:10.1109/TIM.1987.6312761.
- [63] D. V Land, The use of the Allan deviation for the identification and measurement of noise and drift in measurement data., (2014) 1–19.
- [64] T.P. Burg, M. Godin, S.M. Knudsen, W. Shen, G. Carlson, J.S. Foster, K. Babcock, S.R. Manalis, Weighing of biomolecules, single cells and single nanoparticles in fluid, *Nature.* 446 (2007) 1066–1069. doi:10.1038/nature05741.
- [65] M. Godin, A.K. Bryan, T.P. Burg, K. Babcock, S.R. Manalis, Measuring the mass, density, and size of particles and cells using a suspended microchannel resonator, *Appl. Phys. Lett.* 91 (2007) 1–4. doi:10.1063/1.2789694.
- [66] N. Cermak, S. Olcum, F.F. Delgado, S.C. Wasserman, K.R. Payer, M.A. Murakami, S.M. Knudsen, R.J. Kimmerling, M.M. Stevens, Y. Kikuchi, A. Sandikci, M. Ogawa, V. Agache, F. Baléras, D.M. Weinstock, S.R. Manalis, High-throughput measurement of single-cell growth rates using serial microfluidic mass sensor arrays, *Nat. Biotechnol.* 34 (2016) 1052–1059. doi:10.1038/nbt.3666.
- [67] N. Cermak, J.W. Becker, S.M. Knudsen, S.W. Chisholm, S.R. Manalis, M.F. Polz, Direct single-cell biomass estimates for marine bacteria via Archimedes' principle,

- ISME J. 11 (2017) 825–828. doi:10.1038/ismej.2016.161.
- [68] K. Sugioka, J. Xu, D. Wu, Y. Hanada, Z. Wang, Y. Cheng, K. Midorikawa, Femtosecond laser 3D micromachining: A powerful tool for the fabrication of microfluidic, optofluidic, and electrofluidic devices based on glass, *Lab Chip*. 14 (2014) 3447–3458. doi:10.1039/c4lc00548a.
- [69] J. Qiu, K. Miura, K. Hirao, Femtosecond laser-induced microfeatures in glasses and their applications, *J. Non. Cryst. Solids*. 354 (2008) 1100–1111. doi:10.1016/j.jnoncrysol.2007.02.092.
- [70] R. Osellame, H.J.W.M. Hoekstra, G. Cerullo, M. Pollnau, Femtosecond laser microstructuring: An enabling tool for optofluidic lab-on-chips, *Laser Photonics Rev.* 5 (2011) 442–463. doi:10.1002/lpor.201000031.
- [71] F. He, Y. Liao, J. Lin, J. Song, L. Qiao, Y. Cheng, F. He, K. Sugioka, Femtosecond laser fabrication of monolithically integrated microfluidic sensors in glass, *Sensors (Switzerland)*. 14 (2014) 19402–19440. doi:10.3390/s141019402.
- [72] S. Kawata, H.B. Sun, T. Tanaka, K. Takada, Finer features for functional microdevices, *Nature*. 412 (2001) 697–698. doi:10.1038/35089130.
- [73] C.-W. Chang, C.-Y. Chen, T.-L. Chang, C.-J. Ting, C.-P. Wang, C.-P. Chou, Sapphire surface patterning using femtosecond laser micromachining, *Appl. Phys. A*. 109 (2012) 441–448. doi:10.1007/s00339-012-7048-6.
- [74] J.W. Chan, T.R. Huser, S.H. Risbud, D.M. Krol, Modification of the fused silica glass network associated with waveguide fabrication using femtosecond laser pulses, *Appl. Phys. A Mater. Sci. Process.* 76 (2003) 367–372. doi:10.1007/s00339-002-1822-9.
- [75] A. Champion, Y. Bellouard, Direct volume variation measurements in fused silica specimens exposed to femtosecond laser, *Opt. Mater. Express*. 2 (2012) 789. doi:10.1364/OME.2.000789.
- [76] H. Huang, L.-M. Yang, J. Liu, Direct welding of fused silica with femtosecond fiber laser, *Spie Lase.* (2012) 824403. doi:10.1117/12.906076.
- [77] K. Sugioka, J. Xu, D. Wu, Y. Hanada, Z. Wang, Y. Cheng, K. Midorikawa, Femtosecond laser 3D micromachining: a powerful tool for the fabrication of microfluidic, optofluidic, and electrofluidic devices based on glass, *Lab Chip*. 14 (2014) 3447–3458. doi:10.1039/C4LC00548A.
- [78] D.M. Krol, Femtosecond laser modification of glass, *J. Non. Cryst. Solids*. 354 (2008) 416–424. doi:10.1016/j.jnoncrysol.2007.01.098.
- [79] R.R. Gattass, E. Mazur, Femtosecond laser micromachining in transparent materials, *Nat. Photonics*. 2 (2008) 219–225. doi:10.1038/nphoton.2008.47.
- [80] E.A. Romanova, A.I. Konyukhov, Study of irradiation conditions and thermodynamics of optical glass in the problem of modification of materials by femtosecond laser pulses, *Opt. Spectrosc.* 104 (2008) 784–790. doi:10.1134/S0030400X08050226.
- [81] R. a. Libby, E. a. Williams, *Topics in Applied Physics*. Volume 44, 1980. doi:10.1007/978-3-642-10506-7_1.

- [82] R. Menzel, *Photonics: Linear and Nonlinear interaction of laser light and matter*, second edi, Springer US, 2007.
- [83] D. Tan, K.N. Sharafudeen, Y. Yue, J. Qiu, *Femtosecond laser induced phenomena in transparent solid materials: Fundamentals and applications*, *Prog. Mater. Sci.* 76 (2016) 154–228. doi:10.1016/j.pmatsci.2015.09.002.
- [84] B.C. Stuart, M.D. Feit, A.M. Rubenchik, B.W. Shore, M.D. Perry, *Laser-induced damage in dielectrics with nanosecond to subpicosecond pulses*, *Phys. Rev. Lett.* 74 (1995) 2248–2251. doi:10.1103/PhysRevLett.74.2248.
- [85] K. Sugioka, Y. Cheng, *Ultrafast lasers—reliable tools for advanced materials processing*, *Light Sci. Appl.* 3 (2014) 1–12. doi:10.1038/lsa.2014.30.
- [86] S.M. Eaton, H. Zhang, P.R. Herman, F. Yoshino, L. Shah, J. Bovatsek, A.Y. Arai, *Heat accumulation effects in femtosecond laser-written waveguides with variable repetition rate*, *Opt. Express.* 13 (2005) 4708. doi:10.1364/OPEX.13.004708.
- [87] C.B. Schaffner, J.F. García, E. Mazur, *Bulk heating of transparent materials using a high-repetition-rate femtosecond laser*, *Appl. Phys. A Mater. Sci. Process.* 76 (2003) 351–354. doi:10.1007/s00339-002-1819-4.
- [88] S. Kiyama, S. Matsuo, S. Hashimoto, Y. Morihira, *Examination of etching agent and etching mechanism on femtosecond laser microfabrication of channels inside vitreous silica substrates*, *J. Phys. Chem. C.* 113 (2009) 11560–11566. doi:10.1021/jp900915r.
- [89] B. Xu, W.Q. Du, J.W. Li, Y.L. Hu, L. Yang, C.C. Zhang, G.Q. Li, Z.X. Lao, J.C. Ni, J.R. Chu, D. Wu, S.L. Liu, K. Sugioka, *High efficiency integration of three-dimensional functional microdevices inside a microfluidic chip by using femtosecond laser multifoci parallel microfabrication*, *Sci. Rep.* 6 (2016) 1–9. doi:10.1038/srep19989.
- [90] R. Taylor, C. Hnatovsky, E. Simova, *Applications of femtosecond laser induced self-organized planar nanocracks inside fused silica glass*, *Laser Photonics Rev.* 2 (2008) 26–46. doi:10.1002/lpor.200710031.
- [91] S.W. Luo, H.Y. Tsai, *Fabrication of 3D photonic structure on glass materials by femtosecond laser modification with HF etching process*, *J. Mater. Process. Technol.* 213 (2013) 2262–2269. doi:10.1016/j.jmatprotec.2013.06.023.
- [92] J. Thomas, M. Heinrich, J. Burghoff, S. Nolte, A. Ancona, A. Tünnermann, D. Tan, K.N. Sharafudeen, Y. Yue, J. Qiu, K. Sugioka, J. Xu, D. Wu, Y. Hanada, Z.Z. Wang, Y. Cheng, K. Midorikawa, J. Qiu, K. Miura, K. Hirao, O. Of, R. Osellame, H.J.W.M. Hoekstra, G. Cerullo, M. Pollnau, D.M.M. Krol, S. Kiyama, S. Matsuo, S. Hashimoto, Y. Morihira, M. Hermans, J. Gottmann, F. Riedel, F. He, Y. Liao, J. Lin, J. Song, L. Qiao, Y. Cheng, F. He, K. Sugioka, R.R. Gattass, E. Mazur, C.-W. Chang, C.-Y. Chen, T.-L. Chang, C.-J. Ting, C.-P. Wang, C.-P. Chou, S. Kawata, H.B. Sun, T. Tanaka, K. Takada, M. Hermans, J. Gottmann, F. Riedel, L. Xue, L. Wang, T. Xiong, C. Jiang, W. Yuan, K. Sugioka, Y. Cheng, S.W. Luo, H.Y. Tsai, J.W. Chan, T.R. Huser, S.H. Risbud, D.M.M. Krol, Y. Bellouard, A. Said, M. Dugan, P. Bado, B. Xu, W.Q. Du, J.W. Li, Y.L. Hu, L.-M.L. Yang, C.C.

- Zhang, G.Q. Li, Z.X. Lao, J.C. Ni, J.R. Chu, D. Wu, S.L. Liu, K. Sugioka, A. Champion, Y. Bellouard, Y. Liao, J. Qi, P. Wang, W. Chu, Z.Z. Wang, L. Qiao, Y. Cheng, E.A. Romanova, A.I. Konyukhov, H. Huang, L.-M.L. Yang, J. Liu, Y. Bellouard, A. Champion, Selective, laser-induced etching of fused silica at high scan-speeds using KOH, *Sci. Rep.* 5 (2014) 1–9. doi:10.2961/jlmn.2014.02.0009.
- [93] Y. Bellouard, A. Said, M. Dugan, P. Bado, Fabrication of high-aspect ratio, microfluidic channels and tunnels using femtosecond laser pulses and chemical etching, *Opt. Express.* 12 (2004) 2120. doi:10.1364/OPEX.12.002120.
- [94] V. Maselli, R. Osellame, G. Cerullo, R. Ramponi, P. Laporta, L. Magagnin, P.L. Cavallotti, Fabrication of long microchannels with circular cross section using astigmatically shaped femtosecond laser pulses and chemical etching, *Appl. Phys. Lett.* 88 (2006) 86–89. doi:10.1063/1.2203335.
- [95] Y. Bellouard, A. Champion, The femtoprint project, *Symp. Laser Precis. Microfabr.* 7 (2011) 1–9. doi:10.2961/jlmn.2012.01.0001.The.
- [96] M.F. Khan, S. Schmid, P.E. Larsen, Z.J. Davis, W. Yan, E.H. Stenby, A. Boisen, Online measurement of mass density and viscosity of pL fluid samples with suspended microchannel resonator, *Sensors Actuators, B Chem.* 185 (2013) 456–461. doi:10.1016/j.snb.2013.04.095.
- [97] O. Malvar, D. Ramos, C. Martnez, P. Kosaka, J. Tamayo, M. Calleja, Highly sensitive measurement of liquid density in air using suspended microcapillary resonators, *Sensors (Switzerland)*. 15 (2015) 7650–7657. doi:10.3390/s150407650.
- [98] G. Bratbak, I. Dundas, Bacterial dry matter content and biomass estimates, *Appl. Environ. Microbiol.* 48 (1984) 755–757.
- [99] J.S. Daniels, Label-Free Impedance Biosensors : Opportunities and Challenges, (2007). doi:10.1002/elan.200603855.
- [100] P. Kalita, A. Bhola, N. Goel, V. Sritharan, S. Gupta, Molecular Systems Design & Engineering, *Mol. Syst. Des. Eng.* (2017). doi:10.1039/C7ME00037E.
- [101] K. Nagamine, K. Okamoto, S. Otani, H. Kaji, M. Kanzaki, M. Nishizawa, *Biomaterials Science*, (2014) 252–256. doi:10.1039/c3bm60179j.
- [102] H.T. Ngo, H. Wang, A.M. Fales, B.P. Nicholson, C.W. Woods, T. Vo-dinh, dengue diagnosis †, *Analyst.* 139 (2014) 5655–5659. doi:10.1039/C4AN01077A.
- [103] S. Ray, G. Mehta, S. Srivastava, Label-free detection techniques for protein microarrays : Prospects , merits and challenges, (2010) 731–748. doi:10.1002/pmic.200900458.
- [104] T. Brown, DNA Conjugates and Sensors, n.d.
- [105] E. Gizeli and C.R.Lowe, *Biomolecular sensors*, 2002.
- [106] J.E. Butler, Solid supports in enzyme-linked immunosorbent assay and other solid-phase immunoassays., *Methods.* 22 (2000) 4–23. doi:10.1006/meth.2000.1031.
- [107] W. Kusnezow, J.D. Hoheisel, Solid supports for microarray immunoassays., *J. Mol. Recognit.* 16 (2003) 165–76. doi:10.1002/jmr.625.
- [108] J. V Jokerst, J. Chou, J.P. Camp, J. Wong, A. Lennart, A.A. Pollard, P.N. Floriano, N. Christodoulides, G.W. Simmons, Y. Zhou, M.F. Ali, J.T. Mcdevitt, Location of

- Biomarkers and Reagents within Agarose Beads of a Programmable Bio-nano-chip, (2011) 613–624. doi:10.1002/sml.201002089.
- [109] J.C. and J.T.M. J. Chou, A. Lennart, J-Wong, M.F. Ali, P.N. Floriano, N.Christodoulides, Modeling analyte transport and capture in porous bead sensors, NIH Puplic Access. 84 (2014) 2569–2575. doi:10.1021/ac2022822.Modeling.
- [110] E. Kulla, J. Chou, G. Simmons, J. Wong, M.P. Mcrae, R. Patel, P.N. Floriano, N. Christodoulides, R.J. Leach, M. Ian, J.T. Mcdevitt, Enhancement of performance in porous bead-based microchip sensors:effects of chip geometry on bio-agent capture, 5 (2015) 48194–48206. doi:10.1039/C5RA07910A.Enhancement.
- [111] A.N. and C.Y. C. Lei, C. Xu, Ultrasensitive ELISA enhanced by dendritic mesoporous silica nanoparticles, Mater. Chem. B. (2016). doi:10.1039/C6TB01023G.
- [112] S. Derveaux, B.G. Stubbe, K. Braeckmans, C. Roelant, K. Sato, J. Demeester, S.C. De Smedt, Synergism between particle-based multiplexing and microfluidics technologies may bring diagnostics closer to the patient, (2008) 2453–2467. doi:10.1007/s00216-008-2062-4.
- [113] J.A. Thompson, H.H. Bau, Microfluidic , bead-based assay : Theory and experiments &, 878 (2010) 228–236. doi:10.1016/j.jchromb.2009.08.050.
- [114] C. Nicosia, J. Huskens, Materials Horizons Reactive self-assembled monolayers : from surface functionalization to gradient formation, (2014) 32–45. doi:10.1039/c3mh00046j.
- [115] E. Ruckenstein, Z.F. Li, Surface modification and functionalization through the self-assembled monolayer and graft polymerization, 113 (2005) 43–63. doi:10.1016/j.cis.2004.07.009.
- [116] Z.P. Aguilar, Nanomaterials for Medical Applications, n.d.
- [117] R. Narayan, U.Y. Nayak, A.M. Raichur, S. Garg, Mesoporous silica nanoparticles: A comprehensive review on synthesis and recent advances, Pharmaceutics. 10 (2018) 1–49. doi:10.3390/pharmaceutics10030118.
- [118] M. Mahmoodi, A. Behzad-behbahani, S. Sharifzadeh, S. Sadat, A. Tamaddon, Co-condensation synthesis of well-defined mesoporous silica nanoparticles : effect of surface chemical modification on plasmid DNA condensation and transfection, (2017) 995–1004. doi:10.1049/iet-nbt.2017.0078.
- [119] Y.R. Han, J. Park, H. Kim, H. Ji, S.H. Lim, C. Jun, A one-step co-condensation method for the synthesis of well-defined functionalized mesoporous SBA-15 using trimethylsilylanes as organosilane sources †, Chem. Commun. (2015) 1–4. doi:10.1039/C5CC07286G.
- [120] S.-H. Wu, C.-Y. Mou, H.-P. Lin, Synthesis of mesoporous silica nanoparticles, Chem. Soc. Rev. 42 (2013) 3862. doi:10.1039/c3cs35405a.
- [121] S. Huh, J.W. Wiench, J. Yoo, M. Pruski, V.S. Lin, Organic Functionalization and Morphology Control of Mesoporous Silicas via a Co-Condensation Synthesis Method, (2003) 4247–4256. doi:10.1021/cm0210041.
- [122] V.B. Cashin, D.S. Eldridge, A. Yu, D. Zhao, Surface functionalization and

- manipulation of mesoporous silica adsorbents for improved removal of pollutants: A review, *Environ. Sci. Water Res. Technol.* 4 (2018) 110–128. doi:10.1039/c7ew00322f.
- [123] J. Chou, J. Wong, N. Christodoulides, P.N. Floriano, X. Sanchez, J. Mcdevitt, Porous Bead-Based Diagnostic Platforms: Bridging the Gaps in Healthcare, (2012) 15467–15499. doi:10.3390/s121115467.
- [124] D. Sarma, P. Carl, E. Climent, R.J. Schneider, K. Rurack, Multifunctional Polystyrene Core/Silica Shell Microparticles with Antifouling Properties for Bead-Based Multiplexed and Quantitative Analysis, *ACS Appl. Mater. Interfaces.* 11 (2018) 1321–1334. doi:10.1021/acsami.8b10306.
- [125] A. Chiado, C. Novara, A. Lamberti, F. Geobaldo, F. Giorgis, P. Rivolo, Immobilization of Oligonucleotides on Metal–Dielectric Nanostructures for miRNA Detection, *Anal. Chem.* (2016). doi:10.1021/acs.analchem.6b02186.
- [126] C.C. R. Bonnet, C. Farre, L. Valera, L. Vossier, F. Leon, T. Dagland, A. Pouzet, N. Jaffrezic–Renault, J. Fareh, C. Fournier–Wirth, Highly labeled methylene blue–ds DNA silica nanoparticles for signal enhancement of immunoassays: application to the sensitive detection of bacteria in human platelet concentrates, *Analyst.* (2018). doi:10.1039/C8AN00165K.
- [127] R.D. Agata, G. Spoto, W. Wang, Advanced methods for microRNA biosensing : a problem–solving perspective, (2019).
- [128] C.T. Kresge, M.E. Leonowicz, W.J. Roth, J.C. Vartuli, J.S. Becht, Ordered mesoporous molecular sieves synthesized by a liquid– crystal template mechanism, 359 (1992) 710–712.
- [129] A.D.M. and A. Wilkinson, International Union of Pure and Applied Chemistry Compendium of Chemical Terminology, 2014. doi:https://doi.org/10.1351/goldbook.M03853.
- [130] Y.W. and W.Z. Dongyuan Zhao, Ordered mesoporous materials, Wiley–vch, 2013.
- [131] R. Mokaya, W. Zhou, W. Jones, A method for the synthesis of high quality large crystal MCM–41, (1999) 51–52.
- [132] E. Ng, J. Goh, T.C. Ling, R.R. Mukti, Eco–friendly synthesis for MCM–41 nanoporous materials using the non–reacted reagents in mother liquor, *Nanoscale Res. Lett.* 8 (2013) 1. doi:10.1186/1556–276X–8–120.
- [133] C. Pirez, J. Morin, J.C. Manayil, A.F. Lee, K. Wilson, Microporous and Mesoporous Materials Sol–gel synthesis of SBA–15 : Impact of HCl on surface chemistry, *Microporous Mesoporous Mater.* 271 (2018) 196–202. doi:10.1016/j.micromeso.2018.05.043.
- [134] N. Rahmat, A.Z. Abdullah, A.R. Mohamed, A Review : Mesoporous Santa Barbara Amorphous–15 , Types , Synthesis and Its Applications towards Biorefinery Production Norhasyimi Rahmat , 2 Ahmad Zuhairi Abdullah , 2 Abdul Rahman Mohamed Faculty of Chemical Engineering , University Technology MARA , S, *Am. J. Appl. Sci.* 7 (2010) 1579–1586.

- [135] L. Huang, M. Kruk, Versatile surfactant/swelling-agent template for synthesis of large-pore ordered mesoporous silicas and related hollow nanoparticles, *Chem. Mater.* 27 (2015) 679–689. doi:10.1021/cm5028749.
- [136] D. Carmona, F. Balas, J. Santamaria, Pore ordering and surface properties of FDU-12 and SBA-15 mesoporous materials and their relation to drug loading and release in aqueous environments, *Mater. Res. Bull.* 59 (2014) 311–322. doi:10.1016/j.materresbull.2014.07.039.
- [137] C. Yu, J. Fan, B. Tian, D. Zhao, Morphology Development of Mesoporous Materials: A Colloidal Phase Separation Mechanism, *Chem. Mater.* 16 (2004) 889–898. doi:10.1021/cm035011g.
- [138] J.L.Blin and M.Imperator-Clec, Mechanism of self-assembly in the synthesis of silica mesoporous materials: in situ studies by X-ray and neutron scattering, *Chem. Soc. Rev.* (2013) 4071–4082. doi:10.1039/c2cs35362h.
- [139] K. Flodstro, Mechanism of Mesoporous Silica Formation . A Time-Resolved NMR and TEM Study of Silica - Block Copolymer Aggregation, (2004) 680–688.
- [140] J.C.G. and C.G.G. George S.Attard, Liquid-crystalline phases as templates for the synthesis of mesoporous silica, *Lett. to Nat.* 378 (1995) 366–368.
- [141] A. Sundblom, C.L.P. Oliveira, A.E.C. Palmqvist, J.S. Pedersen, Modeling in Situ Small-Angle X-ray Scattering Measurements Following the Formation of Mesostructured Silica, (2009) 7706–7713.
- [142] A. Popat, S.B. Hartono, F. Stahr, J. Liu, S.Z. Qiao, G.Q. Lu, Mesoporous silica nanoparticles for bioadsorption, enzyme immobilisation, and delivery carriers, *Nanoscale.* 3 (2011) 2801–2818. doi:10.1039/c1nr10224a.
- [143] J. Zhang, W. Sun, L. Bergman, J.M. Rosenholm, M. Lindén, G. Wu, H. Xu, H.C. Gu, Magnetic mesoporous silica nanospheres as DNA/drug carrier, *Mater. Lett.* 67 (2012) 379–382. doi:10.1016/j.matlet.2011.09.086.
- [144] F. Torney, B.G. Trewyn, V.S.Y. Lin, K. Wang, Mesoporous silica nanoparticles deliver DNA and chemicals into plants, *Nat. Nanotechnol.* 2 (2007) 295–300. doi:10.1038/nnano.2007.108.
- [145] W.Y.D. Yong, Z. Zhang, G. Cristobal, W.S. Chin, One-pot synthesis of surface functionalized spherical silica particles, *Colloids Surfaces A Physicochem. Eng. Asp.* 460 (2014) 151–157. doi:10.1016/j.colsurfa.2014.03.039.
- [146] P. Li, X.Q. Zhang, Y.J. Chen, T.Y. Bai, H.Z. Lian, X. Hu, One-pot synthesis of thiol- and amine-bifunctionalized mesoporous silica and applications in uptake and speciation of arsenic, *RSC Adv.* 4 (2014) 49421–49428. doi:10.1039/c4ra06563h.
- [147] F. Schuth, Non-siliceous Mesostructured and Mesoporous, (2001) 3184–3195. doi:10.1021/cm011030j.
- [148] Y. Wan, D. Zhao, On the Controllable Soft-Templating Approach to Mesoporous Silicates, 107 (2007). doi:10.1021/cr068020s.
- [149] S.T. Hyde, G.E. Schroder, Novel surfactant mesostructural topologies : between lamellae and columnar (hexagonal) forms, 8 (2003) 5–14. doi:10.1016/S1359-0294.
- [150] A. Fogden, S.T. Hyde, G. Lundberg, Bending Energy of Surfactant Films, 87 (1991)

949–955.

- [151] Y.W. An-Hui Lu, Dongyuan Zhao, Nanocasting a versatile strategy for creating nanostructured porous materials, n.d.
- [152] A. Ruplecker, F. Kleitz, E. Salabas, F. Schu, V. La, Q. Gk, R. V May, V. Re, M. Recci, V. September, Hard Templating Pathways for the Synthesis of Nanostructured Porous Co₃O₄, (2007) 485–496. doi:10.1021/cm0610635.
- [153] S.H. Wu, H.P. Lin, Synthesis of mesoporous silica nanoparticles, Chem. Soc. Rev. 42 (2013) 3862–3875. doi:10.1039/c3cs35405a.
- [154] Z. AlOthman, A Review: Fundamental Aspects of Silicate Mesoporous Materials, Materials (Basel). 5 (2012) 2874–2902. doi:10.3390/ma5122874.
- [155] David Levy and Marcos Zayat, ed., The Sol-Gel Handbook: Synthesis, Characterization, and application, First Edit, Wiley-VCH, 2015.
- [156] F. Hoffmann, M. Cornelius, J. Morell, M. Fröba, Silica-Based Mesoporous Organic – Inorganic Hybrid Materials Angewandte, (2006) 3216–3251. doi:10.1002/anie.200503075.
- [157] I.R. Schmolka, A review of block polymer surfactants, J. Am. Oil Chem. Soc. 54 (1977) 110–116. doi:10.1007/BF02894385.
- [158] J.C.P. Broekhoff, Mesopore Determination from Nitrogen Sorption Isotherms: Fundamentals, Scope, Limitations, Elsevier Scientific Publishing Company, n.d. doi:10.1016/S0167-2991(09)60243-3.
- [159] X.S. Zhao, G.Q.M. Lu, G.J. Millar, Advances in Mesoporous Molecular Sieve MCM-41, 5885 (1996) 2075–2090. doi:10.1021/ie950702a.
- [160] A. Steel, S.W. Car, M.W. Anderson, NMR Study of Surfactant Mesophases in the Synthesis of Mesoporous Silicates, (1994) 1571–1572.
- [161] P. Fromherz, Micelle structure a surfactant-block model, Chem. Phys. Lett. 77 (1981).
- [162] D. Myers, Surfactant science and technology, 3rd Editio, John Wiley & Sons, 2006.
- [163] L. Huang, M. Kruk, Versatile Surfactant/Swelling-Agent Template for Synthesis of Large-Pore Ordered Mesoporous Silicas and Related Hollow Nanoparticles, (2015). doi:10.1021/cm5028749.
- [164] L. Huang, M. Kruk, Synthesis of ultra-large-pore FDU-12 silica using ethylbenzene as micelle expander, J. Colloid Interface Sci. 365 (2012) 137–142. doi:10.1016/j.jcis.2011.09.044.
- [165] X. Lv, L. Zhang, F. Xing, H. Lin, Microporous and Mesoporous Materials Controlled synthesis of monodispersed mesoporous silica nanoparticles : Particle size tuning and formation mechanism investigation, Microporous Mesoporous Mater. 225 (2016) 238–244. doi:10.1016/j.micromeso.2015.12.024.
- [166] K. Song, J. Guan, Z. Wang, C. Xu, Q. Kan, Post-treatment of mesoporous material with high temperature for synthesis super-microporous materials with enhanced hydrothermal stability, Appl. Surf. Sci. 255 (2009) 5843–5846. doi:10.1016/j.apsusc.2009.01.016.
- [167] A. Hozumi, H. Sugimura, K. Hiraku, T. Kameyama, O. Takai, Low-Temperature

- Elimination of Organic Components from Mesostructured Organic – Inorganic Composite Films Using Vacuum Ultraviolet Light, (2000) 3842–3847. doi:10.1021/cm000546k.
- [168] R.M. Grudzien, B.E. Grabicka, M. Jaroniec, Effective method for removal of polymeric template from SBA-16 silica combining extraction and temperature-controlled calcination {, (2006) 819–823. doi:10.1039/b515975j.
- [169] M.E. Davis, Ordered porous materials for emerging applications, *Nature*. 417 (2002) 813–821.
- [170] V. Biju, Chemical modification and bioconjugate reaction of nanomaterials for sensing, imaging, drug delivery and therapy, 43 (2014). doi:10.1039/c3cs60273g.
- [171] G. Kickelbick, Hybrid Inorganic – Organic Mesoporous Materials, (2004) 3102–3104. doi:10.1002/anie.200301751.
- [172] D. Rath, S. and K.M.P. Rana, Organic amine functionalized silica based mesoporous materials: an update of syntheses and catalytic applications, *RSC Adv.* (2014). doi:10.1039/C4RA08005J.
- [173] A. Chiadò, G. Palmara, S. Ricciardi, F. Frascella, M. Castellino, M. Tortello, C. Ricciardi, P. Rivolo, Colloids and Surfaces B: Biointerfaces Optimization and characterization of a homogeneous carboxylic surface functionalization for silicon-based biosensing, *Colloids Surfaces B Biointerfaces*. 143 (2016) 252–259. doi:10.1016/j.colsurfb.2016.03.048.
- [174] M.T. S. Lowell, J.E. Shields, M.A. Thomas, *Characterization of Porous Solids and Powders: Surface Area, Pore Size and Density*, Kluwer Academic Publishers, 2004. doi:10.1007/978-1-4020-2303-3.
- [175] G.B. Heggannavar, C.G. Hiremath, D.D. Achari, V.G. Pangarkar, M.Y. Kariduraganavar, Development of Doxorubicin-Loaded Magnetic Silica – Pluronic F - 127 Nanocarriers Conjugated with Transferrin for Treating Glioblastoma across the Blood – Brain Barrier Using an in Vitro Model, *ACS Omega*. 3 (2018) 8017–8026. doi:10.1021/acsomega.8b00152.
- [176] M.Y. and H.B. Y. Shen, Y. Zhang, X. Zhang, X. Zhou, X. Teng, Horseradish peroxidase-immobilized magnetic mesoporous silica nanoparticles as a potential candidate to eliminate intracellular reactive oxygen species, *Nanoscale*. (2015). doi:10.1039/C4NR06269H.
- [177] F. Nhavene, G. Ferreira, A. Id, J. Araujo, D.A. Gomes, Biodegradable Polymers Grafted onto Multifunctional Mesoporous Silica Nanoparticles for Gene Delivery, 41 (n.d.) 1–16. doi:10.3390/chemengineering2020024.
- [178] Y. Yu, J. Addai-Mensah, D. Losic, Functionalized diatom silica microparticles for removal of mercury ions, *Sci. Technol. Adv. Mater.* 13 (2012). doi:10.1088/1468-6996/13/1/015008.
- [179] D.L. Taylor, R. Kapur, T. Adams, K.A. Giuliano, M. Mrksich, H.G. Craighead, D.R. Jung, R. Kapur, T. Adams, K.A. Giuliano, M. Mrksich, *Critical Reviews in Biotechnology Topographical and Physicochemical Modification of Material Surface to Enable Patterning of Living Cells Topographical and Physicochemical*

Modification of Material Surface to Enable Patterning of Living Cells, 2008. doi:10.1080/20013891081700.

- [180] T.B.J. Masao Washizu, Generalized multipolar dielectrophoretic force and electrorotational torque calculation, *J. Electrostat.* 38 (1996) 199–211.
- [181] K. Svoboda, S.M. Block, Biological applications of optical forces, (1994).
- [182] A. Ozcelik, J. Rufo, F. Guo, Y. Gu, P. Li, J. Lata, T.J. Huang, Acoustic tweezers for the life sciences, *Nat. Methods.* 15 (2018). doi:10.1038/s41592-018-0222-9.
- [183] J. Voldman, Dielectrophoretic traps for cell manipulation, in: *BioMeMS Biomed. Nanotechnol.*, Springer, Boston, MA, 2006. doi:https://doi.org/10.1007/978-0-387-25845-4_8.
- [184] H.-G.R. and M.M. B.R. Patil, M. Mirsafaei, P.P. Cielecki, A.L.F. Cauduro, J. Giutowski, ITO with embedded silver grids as transparent conductive electrodes for large area organic solar cells, *IOP Sci.* (2017) 0–11. doi:doi.org/10.1088/1741-2552.
- [185] M. Mazur, J. Domaradzki, D. Kaczmarek, S. Moh, F. Placido, Sheet resistance and optical properties of ITO thin films deposited by magnetron sputtering with different O₂/ar flow ratio, *Proc. 2010 Int. Students Young Sci. Work. “Photonics Microsystems”*, STYSW 2010. (2010) 60–63. doi:10.1109/STYSW.2010.5714168.

Appendix A: Single Clamped beam design

The clamped-clamped beam geometry has been chosen as preferential design to test the femtosecond laser direct writing. In fact, this design shows less complex fabrication problematic, which concern with the mechanical stability of the suspended beam and the embedded channel path. Nevertheless, in order to investigate the effectiveness of this new fabrication method, a single clamped beam design was also tested (Figure A.1). The main constrain linked to the femtosecond laser direct writing is the minimum beam thickness achievable, strongly dependent to the minimum size of the laser spot. Working with a 50X objective, this size is around 10 μm and it allows to obtain suspended beam with a minimum thickness of 30 μm , making the beam structure quite heavy. This has a small impact for the realization of a double clamped beam, but can drastically affect the mechanical stability of a single clamped beam.

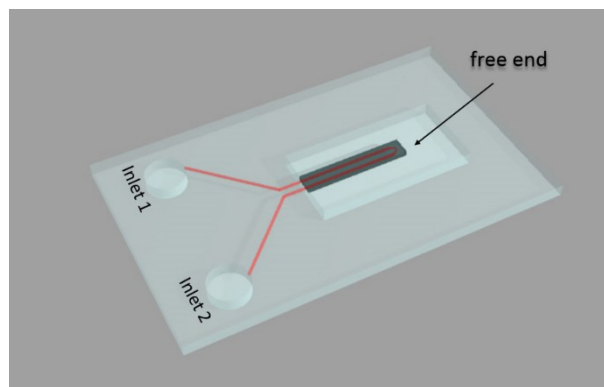


Figure A.1 Schematic representation of the single clamped beam. In red is highlighted the embedded-channel path along the suspended structure and the connection with the inlets.

In fact, the main problem observed, in the cantilever fabrication, was the self-standing properties, which limited the maximum length achievable around 750 μm , coupled with a width of about 70 μm . The second problem observed was related to the impossibility to completely empty the embedded microchannels from the exposed glass, mostly at the tip of the beam (Figure A.2). This is probably caused by the channel length coupled with the KOH etching protocol that is unfortunately limited by the diffusion for distance higher than 2 mm. Nevertheless, this problem can be in principle solved changing the design of the fluidic system by reducing the distance between the cantilever structure and the inlet, finding a new design for the PDMS fluidic interface.

The as obtained suspended structure was tested from the mechanical point of view. The first mode resonance frequencies of three cantilevers were measured: as it is possible to observe from Figure A.2, the resonance frequencies range from 39 to 71 kHz. For each of the sample the Q factor (air as surrounding media) was estimated from the Lorentz fit of the resonance curves (overlapped to the frequency peak in Figure A.2). The values ranges from 1042 to 1385, which results in higher Q factors with respect to the clamped-clamped beam ones. From the inset in Figure A.2 (optical microscope images of the SMR) it is possible to observe the critical aspect of the channel opening, as previously described. In fact, the samples F2_2 and F2_3 show only a partial release of the embedded channel in the region near the clamping (dracker line along the beam), which bridges to a different beam mass and resonance frequency even if the dimensions are the same.

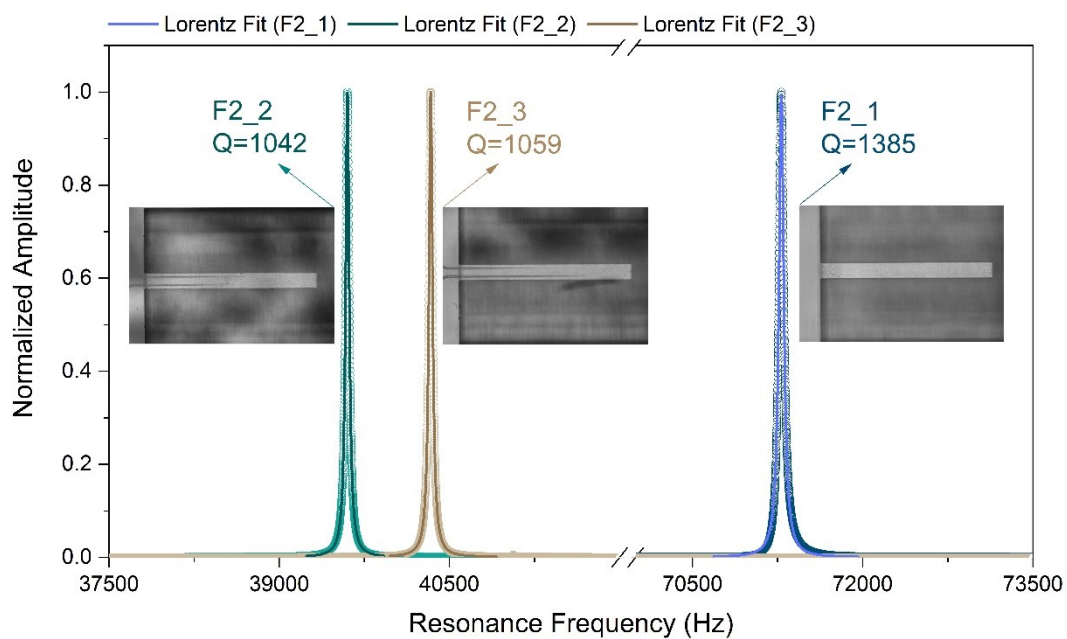


Figure A.2 First mode resonance frequencies. In the graph are represented the resonance peak and the Q factor for three clamped beam, two of them show a partial presence of the embedded fluidic channel near the clamping region.

Considering the first mode resonance frequency of these three samples as a good approximation of the resonance frequency for the final SMR cantilever design-, and considering the mass of the resonators comprised between 3.72 and 2.68 pg, the responsivity should be in the range of few tens of Hz/ng. Therefore, the overall responsivity results lowered with respect to the one estimated for the bridge samples.

In order to complete the mechanical characterization of the single clamped beam, Allan's deviation analysis was performed (Figure A.3a). The sample F2_1 was selected as representative sample for the clamped beam set, and the results of the Allan's deviation were compared with the Allan's deviation of the bridge resonator with the same nominal dimensions (Figure A.3b-c). The glass cantilever shows a frequency stability three times improved than the bridge resonator one, respectively $5.79 \cdot 10^{-9}$ and $1.67 \cdot 10^{-8}$. Considering the possibility to accomplish the complete release of the embedded channel, the cantilever can be an attractive alternative to the bridge design.

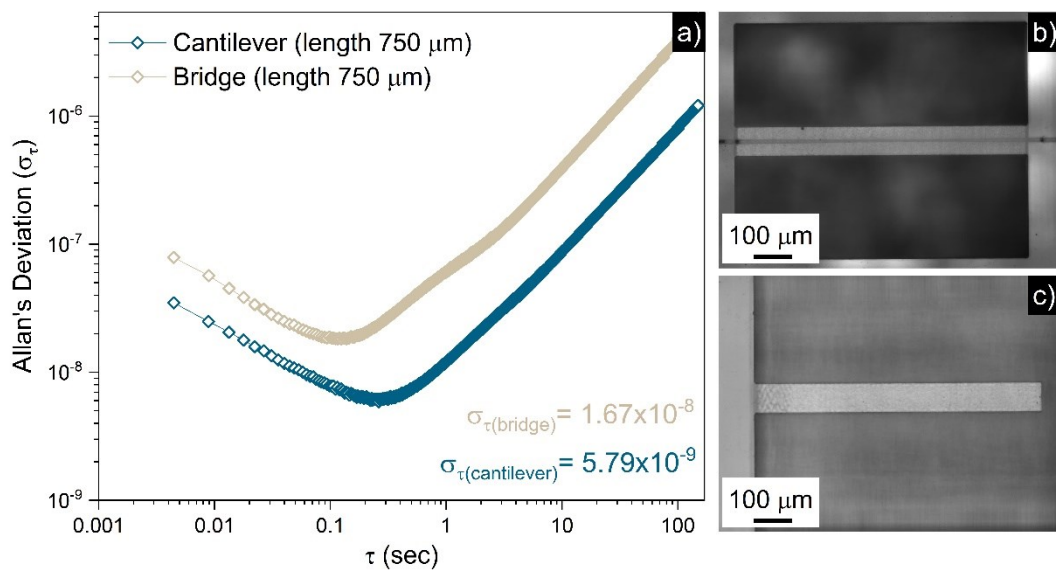


Figure A.3 Allan's deviation analysis. a) In the graph are reported the Allan's deviation values as function of the time, comparing the behaviour for a cantilever and a bridge suspended structure. b-d) Optical microscope images of the bridge and cantilever SMR.

**Appendix B: SMRs
characterization**

Considering the large number of tested designs, this appendix resumes the main mechanical properties related to different clamped–clamped beam resonators with variable length, width and thickness. Taking into account the different geometries and dimensions of the embedded channel (Chapter 3), the resonance frequency (f_0) (air and vacuum measurement), the mass and the responsivity (\mathfrak{R}) have been evaluated and resumed in the Table B.1.

L (μm)	W (μm)	h (μm)	$channel$ (μm)	$channel$ (μm)	$Mass$ (μg)	f_0 Air (Hz)	f_0 Vac (Hz)	\mathfrak{R} (Hz/ ng)
450	50	45	32.17	14.69	1.76	$1.177 \cdot 10^6$	$1.179 \cdot 10^6$	334
500	50	45	32.17	14.69	1.96	$8.504 \cdot 10^5$	$8.503 \cdot 10^5$	217
750	50	45	32.17	14.69	2.94	$4.057 \cdot 10^5$	$4.059 \cdot 10^5$	69
450	50	45	31.28	34.96	1.15	$1.235 \cdot 10^6$	$1.237 \cdot 10^6$	539
500	50	45	31.28	34.96	1.27	$1.010 \cdot 10^6$	$1.010 \cdot 10^6$	396
750	50	45	31.28	34.96	1.91	$4.585 \cdot 10^5$	$4.584 \cdot 10^5$	120
450	75	45	32.17	14.69	2.88	$1.215 \cdot 10^6$	–	211
500	75	45	32.17	14.69	3.20	$8.870 \cdot 10^5$	$8.870 \cdot 10^5$	139
750	75	45	32.17	14.69	4.80	$4.429 \cdot 10^5$	$4.433 \cdot 10^5$	46
450	75	45	30.55	59.04	1.56	$9.790 \cdot 10^5$	$9.793 \cdot 10^5$	314
500	75	45	30.55	59.04	1.73	$8.289 \cdot 10^5$	$8.293 \cdot 10^5$	239
750	75	45	30.55	59.04	2.60	$4.421 \cdot 10^5$	$4.427 \cdot 10^5$	85
450	50	45	32.17	14.69	1.76	$1.170 \cdot 10^6$	$1.170 \cdot 10^6$	332
450	50	45	32.17	14.69	1.76	$1.193 \cdot 10^6$	$1.194 \cdot 10^6$	339
450	50	45	32.17	14.69	1.76	$1.235 \cdot 10^6$	$1.236 \cdot 10^6$	350
450	75	45	32.17	14.69	2.88	$1.063 \cdot 10^6$	$1.064 \cdot 10^6$	185
450	75	45	32.17	14.69	2.88	$1.198 \cdot 10^6$	$1.198 \cdot 10^6$	208
450	75	45	32.17	14.69	2.88	$1.187 \cdot 10^6$	$1.187 \cdot 10^6$	206
400	75	30	8	7.5	1.82	$7.552 \cdot 10^5$	$7.568 \cdot 10^5$	208
500	75	30	8	7.5	2.27	$3.649 \cdot 10^5$	$3.658 \cdot 10^5$	80
750	75	30	8	7.5	3.41	$2.485 \cdot 10^5$	$2.491 \cdot 10^5$	37
1000	75	30	8	7.5	4.54	$1.409 \cdot 10^5$	$1.410 \cdot 10^5$	15
750	70	30	8	7.5	3.16	$2.141 \cdot 10^5$	$2.139 \cdot 10^5$	34
700	90	30	8	7.5	3.87	$4.324 \cdot 10^5$	$4.327 \cdot 10^5$	56
700	90	30	8	7.5	3.87	$4.156 \cdot 10^5$	$4.160 \cdot 10^5$	54

Table B.1 Resonance Frequency (air and vacuum) and Responsivity (air), calculated considering the mass of the empty resonator. The table is divided horizontally in two sections: the upper one is related to the SMR fabricated with the 20X objective and the lower part is referred to the SMR fabricated with the 50X objective. The samples that show the best responsivity are highlighted in red.

The resonance frequency related to the first flexural mode of each double clamped beam are reported in figure B.1. Three main groups have been created in order to display the experimental data as a function of the mechanical resonator

length: figure B.1a 400–450 μm , figure B.1b 500 μm and figure B.1c 700–750 μm , the only exception is represented by the beam long 1000 μm that was grouped in the last set of data.

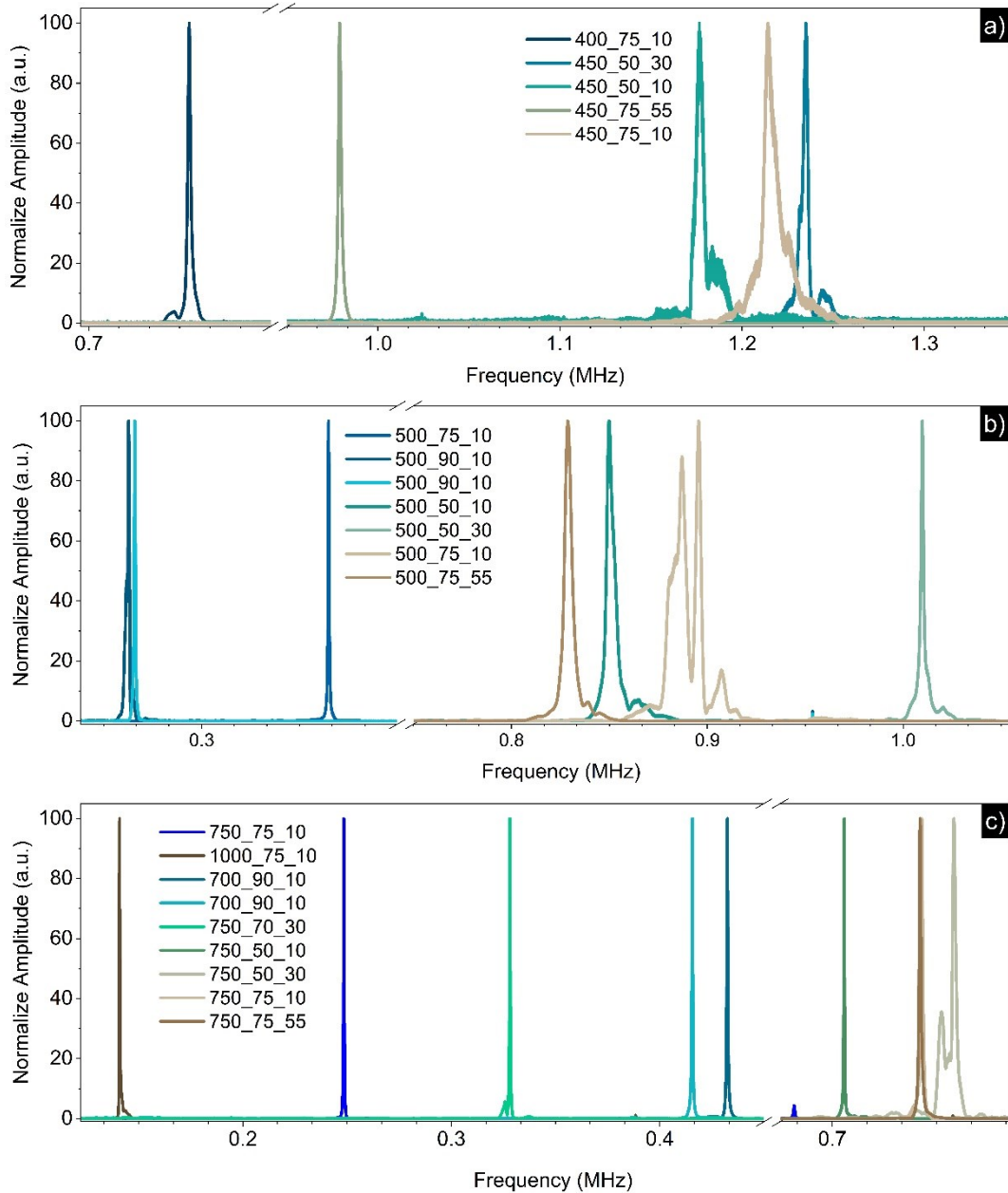


Figure B.1 First mode of resonance, for different micromechanical resonators characterized by variable length, width and thickness (a–b–c).

The Q factor estimation was obtained by two different methods: considering the ratio between the frequency and the width of the resonance peak at -3dB or by means of the ring down analysis. In the first case, the parameters needed for the Q factor computation were extrapolated using the Lorentzian fit of the resonance peak (as

shown in the Chapter 4). For the ring down analysis, the decay behaviour of the amplitude signal was evaluated using an exponential decay fit,

$$A(t) = A_0 e^{-\frac{t}{\tau_c}} \quad (\text{B1.1})$$

where the time constant τ_c is directly proportional to the Q factor. In fact, if the feedback loop is not applied to the system, the resonator generally relaxes from a perturbed state to a “natural” state in a frame time that is referred to the decay time $\tau_c = Q/\pi f_0$.

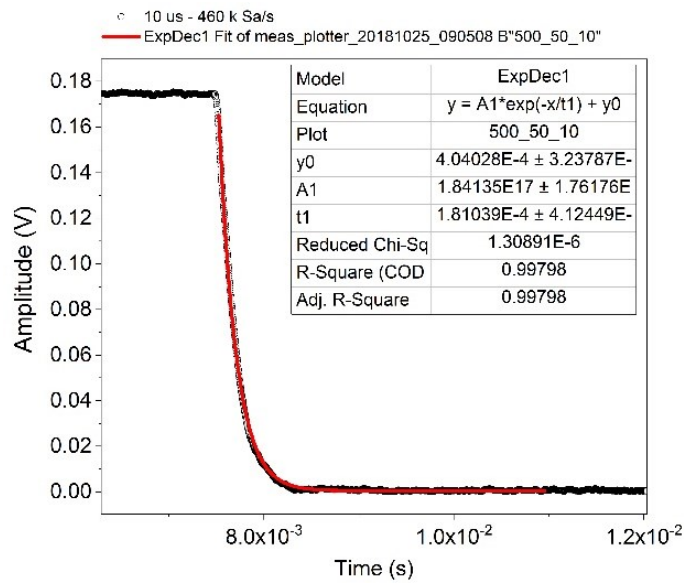


Figure B.2 Example of exponential decay fit used for the computation of the Q factor from the ring down analysis.

The averaged Q factor, computed with the two methods, have been compared and resumed in Table B.2. The data are displayed as function of the micromechanical resonator and channel dimensions. For most of the samples, both the Q factor computations seem to return comparable values.

L (μm)	W (μm)	h (μm)	channel (μm)	channel (μm)	Q factor (Lorentzian fit)	SD	Q factor (Ring down)	SD
450	50	45	31.28	34.96	362.26	8.21	399.34	5.48
450	50	45	32.17	14.69	224.68	37.67	293.78	25.97

450	50	45	32.17	14.69	285.34	17.60	293.78	25.97
450	50	45	32.17	14.69	329.64	19.25	380.26	2.65
450	50	45	32.17	14.69	254.23	45.88	209.40	5.48
450	75	45	30.55	59.04	529.39	1.68	378.11	0.00
450	75	45	32.17	14.69	161.75	40.35	190.83	16.19
450	75	45	32.17	14.69	199.14	18.75	365.66	11.81
450	75	45	32.17	14.69	373.98	13.07	462.57	5.32
450	75	45	32.17	14.69	298.69	5.88	426.62	23.71
500	50	45	32.17	14.69	194.43	0.34	409.88	1.89
500	50	45	31.28	34.96	612.10	92.53	556.46	2.24
500	75	45	32.17	14.69	149.20	1.69	366.26	9.85
750	50	45	32.17	14.69	1003.82	1.39	837.76	3.60
750	50	45	31.28	34.96	250.43	1.01	403.07	6.11
750	75	45	32.17	14.69	384.29	3.27	398.48	4.92
750	75	45	30.55	59.04	443.96	1.76	551.16	0.00

Table B.2 Comparison of the Q factors calculated using the Lorentz fit or the Exponential decay fit.

For what concerns the Allan's deviation analysis, two different approaches have been used to evaluate the impact of the measurement set-up used. For this reason, the SMRs fabricated with the 20X objective were analysed with an open and a close loop system to compute the frequency stability. As it is possible to observe from the Figure B.3 the two approaches return different frequency fluctuation. This phenomenon is directly correlated to the evaluation of the minimum detectable mass. In the worst case (beam length 450 μm) the Allan's deviation values show high variation between the close and open loop acquisition. The difference in the evaluation of the minimum σ_τ seems to less affect the values related to the beam with length equal to 750 μm (figure B.3e-f). The impact of the measurement set-up will require further in-depth analyses that are not been complete yet.

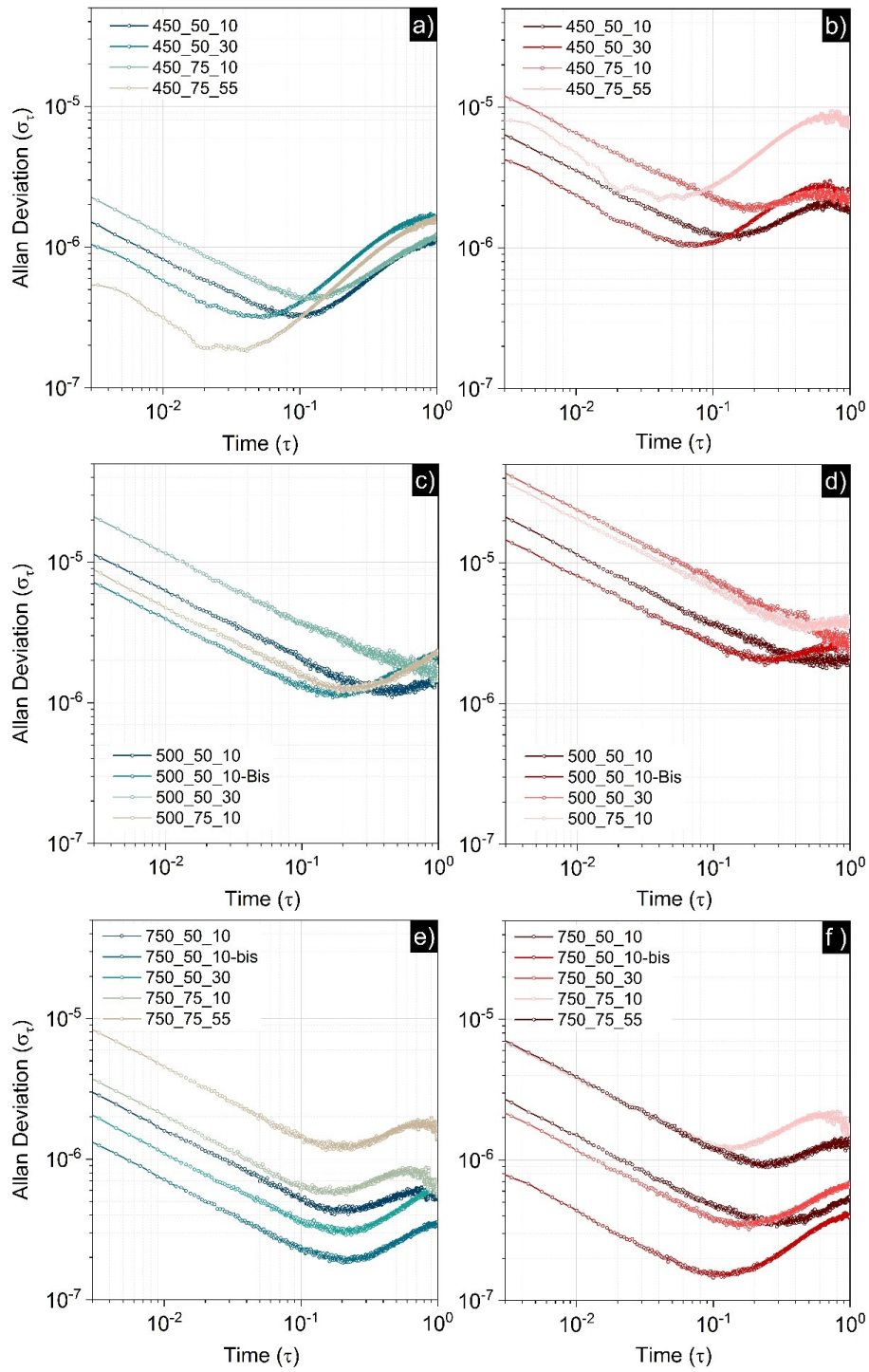


Figure B.3 Allan's deviation analysis. The Allan's deviation curves are reported in the graph and the close (blue line) and the open (red line) loop response was compared for different SMRs length, a-b) 450 μm , b-c) 500 μm and d-e) 750 μm .

Appendix C: Electrodes integration

The SMRs show great potentiality in the biological fields, such as the study of single cell growth, the analysis of the antibiotic susceptibility, membrane permeabilization and other related studies. In this context, the possibility to directly manipulate the cells flowing inside the SMRs seems to be an attractive prospective and require proper strategies in order to make it effective. The manipulation of the physical location and the organization of cells and other particles, such as those synthesized in this work for the beads-based bioassay, are a fundamental part in this attempt.

Many techniques have been widely investigated, including surface modification, acoustic forces, optical and electrical tweezers [179–182]. This last approach, and in particular the dielectrophoresis (DEP), is became more and more a common modality for the particles/cells manipulation and trapping [183] for in flow analysis. Considering our SMR design and the fabrication approach used, the DEP seems to be an attractive solution for the controlled and spatially resolved confinement of particles, taking into account the destabilizing force of the surrounding environment (the liquid in which the particles are suspended and spread along the channel).

In order to understand the feasibility of an integrated SMR–DEP system, a preliminary approach for the electrodes deposition on top of the suspended resonator has been investigated. First of all, the SMR fabrication, based on the femtosecond direct writing was deeply analysed, step by step, in order to identify at which stage of the process the electrodes deposition could be integrated. Fortunately, the deposition of metal electrodes on glass is a well-known process and in literature there are many different approaches. Regarding the direct integration of the electrodes on top of the SMR, three main strategies were taken into account and their compatibility with SMR fabrication was evaluated:

- I. A preliminary deposition of the electrodes followed by the two step process for the SMR fabrication;
- II. Deposition of the electrodes after the SMR laser writing and release in KOH;
- III. An intermediate electrodes deposition, immediately after the laser writing process, but before the SMR release in KOH.

Each of these strategies shows some significant constraints. The first approach suffered of two main problems: depositing the electrodes before the SMR laser patterning makes the channel path definition not possible. In fact, the electrodes material would

block the bulk penetration of the laser that should be focalized in the central plane of the SMR to create the embedded channel path. The second problem is represented by the electrodes material resistance against the aggressive KOH etching, at 80°C.

The second strategy, regarding the electrode deposition as last step, could overcome the compatibility problems between the electrodes material and the aggressive etching procedures needed for the SMR release. Unfortunately, the presence of a suspended structure, characterized by a variable under-gap high, makes the standard techniques of photoresist coating (i.e. spinning) not effective. In particular the presence of discontinues surfaces, like the under-gap and the inlet for the fluidic integration, creates a non-homogeneous coating at the edges of these discontinuity that during the metal deposition can cause the formation of a short circuit between the two electrodes.

Finally, the third approach minimizes the constraints. In particular, when depositing the electrodes after the laser writing, the problem to overcome resulted the compatibility between the electrodes material (considering also the deposition process chosen for this purpose) and the aggressive KOH etching. Considering the possibility to preserve the characteristic transparency of the glass SMR, the ITO (Indium-Tin-Oxide) was proposed as possible electrode material. This material has been widely used for the creation of transparent conductive electrodes in organic solar cells application [184], thanks to its high transmittance in the visible range [185]. Compared to other typical electrode materials, like Platinum (Pt) and Gold (Au), the ITO shows a higher resistivity that can vary from 2.6 to $3.4 \cdot 10^{-6} \Omega\text{m}$, depending on the deposition temperature and the O_2/Ar flow ratio.

In this work, two different ITO-deposition strategies were tested, in particular the deposition was carried out using a Radio Frequency (RF) sputtering system (Spider 600) and two fused silica wafers were respectively coated with 200 nm of ITO, deposited with and without O_2 (O_2/Ar ratio of 1:7.5), at room temperature (RT). For the ITO(O_2)-sample the magnetron power was settled at 500 W and the rate of deposition was 22.1 nm/min. The same power was also used for the ITO-sample, but the deposition rate was increase up to 176.0 nm/min. Subsequently, the ITO thin film was patterned to obtain the final electrodes design to be tested in the KOH etching bath (80 °C). As it is possible to observe from the optical microscope images (Figure C.1), both the ITO thin films were damaged by the KOH etching. In

particular for the ITO(O₂)-sample the thickness of the deposited film was drastically reduced, as it is possible to deduce from the colour variation before and after the KOH etching. On the contrary, the ITO-samples seems to be more resistant to the effect of the etching bath, even if the prolonged exposure to high KOH concentration at 80 °C caused the formation of a pinhole structure along the ITO-film.

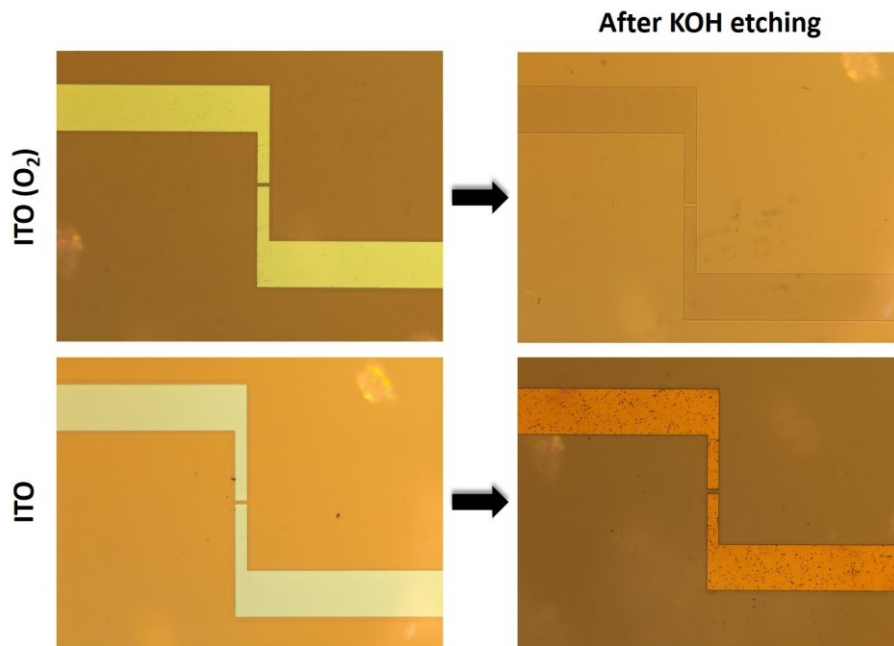


Figure C.1 Optical microscope images relative to the ITO resistance test. In the images are reported the morphological aspect of the ITO(O₂) and ITO samples before and after the KOH etching.

The poor resistance of the ITO and ITO-(O₂) substrates to the KOH etching is further confirmed by the transmittance spectra recorded before and after the exposure to the etchant solution (Figure C.2). The almost total removal of the thin film is evident comparing the transmittance curves of the ITO-(O₂) after the KOH with that of the pristine fused silica. As expected, from the optical microscope images, the 100% transmittance result to be almost restored to the pristine value, confirming the removal of the ITO-(O₂) deposited. For the ITO substrate, the transmittance curves show a similar behaviour before and after the KOH, even if slightly modified after the KOH.

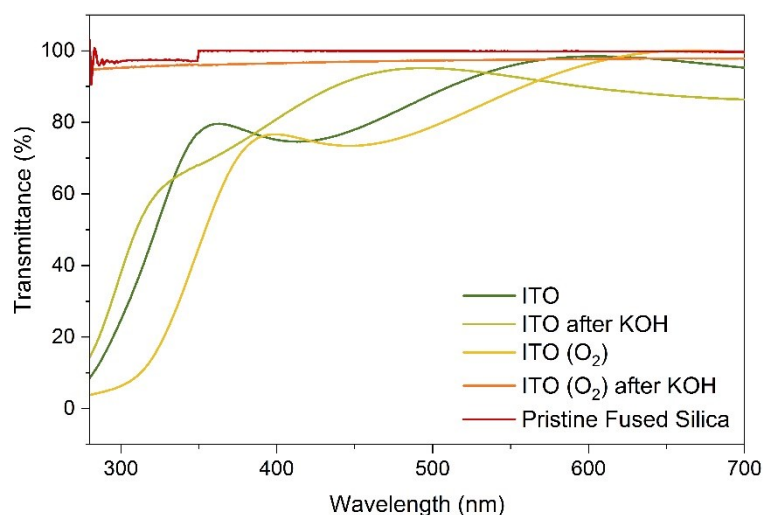


Figure C.2 Transmittance spectra for the ITO and ITO-(O₂) samples. In the graph are reported the transmittance curves before and after the KOH treatment. As reference is reported (red curve), the transmittance associated to the pristine fused silica.

Considering the results obtained from the KOH-test for the ITO and ITO-(O₂) films, the possibility to use them as transparent electrodes material was discarded and the test of standard electrodes materials, like Au and Pt, was considered. Two different deposition protocols have been settled. For the Pt electrodes, a RT deposition was performed using a Direct Current (DC) sputtering method (Spider 600). Firstly, an adhesion layer of 20 nm of Titanium (Ti) were deposited on the fused silica surface with the following recipe: magnetron power 1000 W, Ar 2 sccm and deposition rate equal to 120 nm/min. With the same power setting, 200 nm of Pt were deposited with a rate of 230 nm/min and an Ar flow of 15 sccm.

For the deposition of the Au electrodes, an adhesion layer is needed to improve the stability of the thin film on the fused silica surface. One of the most common adhesion layer used for this purpose is the Chromium (Cr), which unfortunately shows a poor resistance against aggressive etchant solutions. In order to increase the overall stability of the Cr/Au layers, an evaporation approach (Alliance-Concept EVA 760 evaporator e-gun) at high temperature (300 °C) was preferred to the sputtering method used for the ITO and Pt electrodes. Furthermore, a double Cr-Au/Cr-Au layer was deposited increasing the resistance to aggressive etchant and avoiding the pin-hole formation thanks to the double layer. From the optical images reported in Figure C.3, the higher stability of the Cr-Au/Cr-Au deposition was confirmed observing the thin film condition before and after the KOH etching. On the contrary,

the Ti/Pt electrodes have been considered incompatible with the prolonged KOH bath that caused the almost complete removal of the Pt layer (Figure C.3).

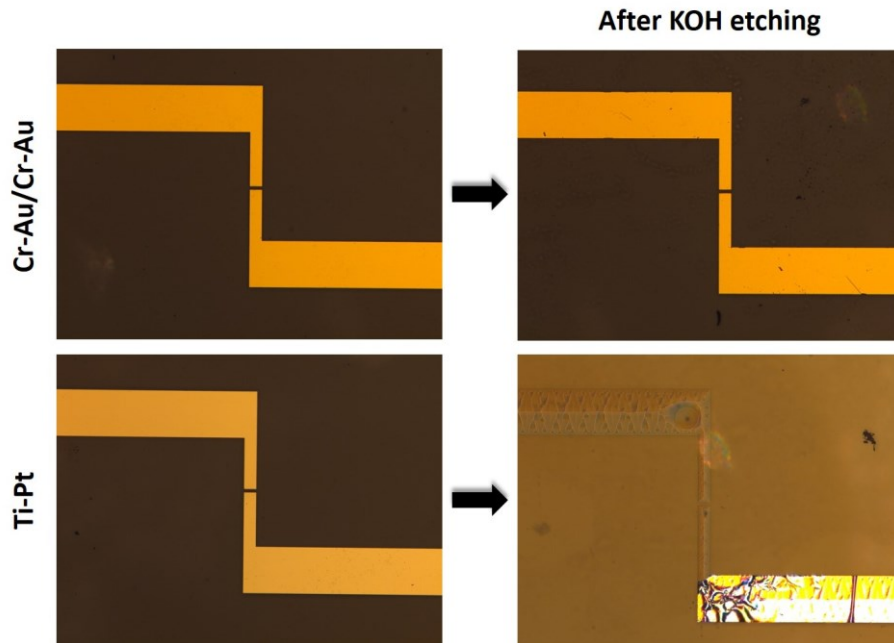


Figure C.3 Optical microscope images relative to the Cr-Au/Cr-Au and Ti/Pt resistance test. In the images are reported the morphological aspect of the Cr-Au/Cr-Au and Ti/Pt samples before and after the KOH etching.

After the preliminary tests focused on the evaluation of the ITO, Au and Pt resistance in highly concentrated KOH solution, the electrodes deposition and patterning protocol were optimized (Figure C.4). First, the SMR structure was patterned with the optimized femtosecond laser writing process (Chapter 3), then the fused silica wafer was coated with a double Cr-Au/Cr-Au layer (evaporated at high temperature). In order to transfer the electrode pattern, which is characterized by a small gap of 20 μm centred along the SMRs, the metal layers were coated with 2 μm of a negative photoresist (AZ1512) and then patterned with a direct writing process (MLA150 direct writer) with 110 mJ/cm^2 dose and a defocus of -2. The not exposed parts have been subsequently removed with the AZ1512 developer solution.

The electrodes shape was subsequently defined by Ion Beam Etching (Veeco Nexus IBE350), with an exposure time between 7 min and 8 min. Finally, the photoresist left was removed with an oxygen plasma for 10 minutes. As it is possible to observe from the pictures in Figure C.5a, the electrodes were well aligned with the suspended structure and the gap is centred along the beam.

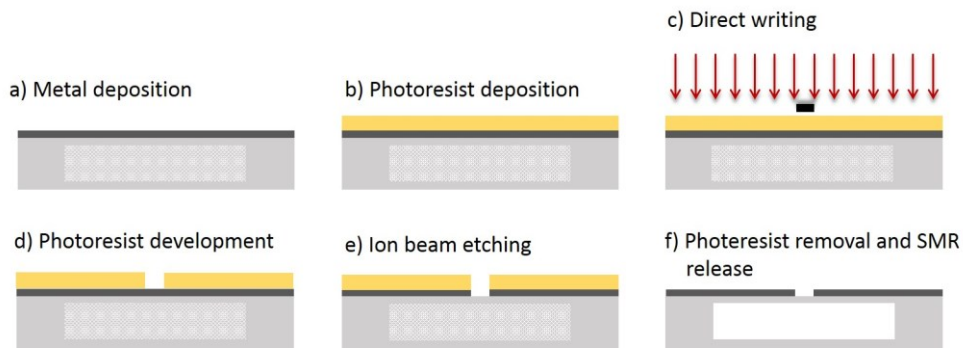


Figure C.4 Schematic representation of the process flow for the electrodes integration. The electrodes deposition and patterning were obtained following the depicted step by step process, which involves the metal deposition followed by the photoresist coating. The electrodes geometries were patterned by the means of a laser direct writing followed by the removal of the un-exposed resist. The geometry was finally obtained using an ion beam etching followed by the photoresist removal and the SMR release by KOH etching.

Unfortunately, the preliminary femtosecond laser writing leaved some residues along the SMR edges, due to a collateral re-deposition of fused silica. This caused some discontinuities of the Cr-Au/Cr-Au layer and the subsequent detachment of the thin film during the KOH etching (Figure C.5b). This problem can be easily solved adjusting the exposure parameter of the femtosecond laser, in order to avoid the fused silica re-deposition along the laser path. Considering the good results of the electrodes deposition on top of the SMR, the design of the electrodes should be now optimized in order to evaluate the effective possibility to integrate the DEP system for the particles trapping in the middle of the suspended resonator.

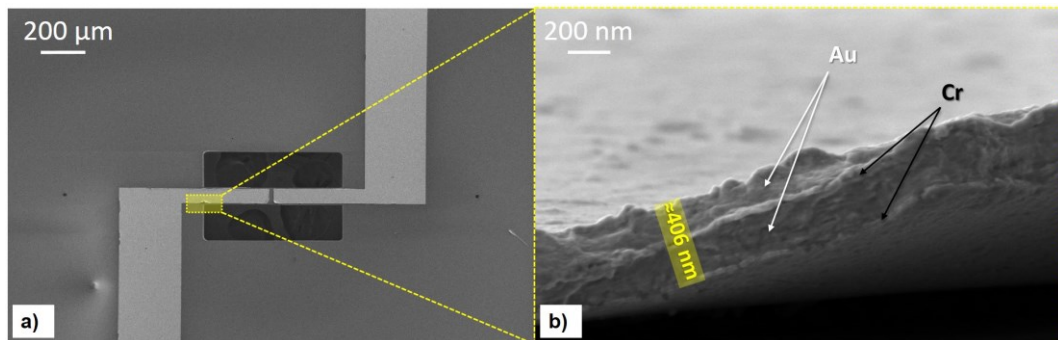


Figure C.5 SEM images of the electrodes deposited on the SMR structures. a) Top-view of the electrodes, the alignment was successfully obtained and the gap between the electrodes was perfectly centered along the SMR structure. b) detail of an adhesion defect of the Cr-Au/Cr-Au layer, probably due to the fused silica redeposition, along the SMR edges, during the femtosecond laser writing.

Appendix D: Reagents

Water used during each step was Ultra-Pure Water dispensed from a DirectQ-3UV Merck-Millipore (Milan, Italy).

Beads synthesis. Toluene (99.8%), , tetraethylorthosilicate (TEOS), (3-aminopropyl)triethoxysilane (APTES, 98%), (3-mercaptopropyl)trimethoxysilane (MPTMS 98%), tetrahydrofuran (THF, 99.9%), trimethylamine (TEA), succinic anhydride (SA, 99%), 1,3,5-trimethylbenzene (TMB), hydrochloric acid (HCl, 37%), Pluronic® F127, were purchased from Sigma Aldrich/Merk (Milan, Italy).

Ellaman's test. 5-5'-dithiobis(2-nitrobenzoic acid) \geq 98% (DTNB), L-cysteine, sodium acetate salt (>99%), Tris(hydroxymethyl)aminomethane (TRIS base), hydrochloric acid (HCl, 37%), were purchased from Sigma Aldrich/Merk (Milan, Italy).

Bead-based assay: pores availability. Fluorescein isothiocyanate (FITC), Monobasic sodium phosphate (NaH_2PO_4), Dibasic sodium phosphate (Na_2HPO_4), were purchased from Sigma Aldrich/Merk (Milan, Italy).

Bead-based assay: passivation, immobilization and hybridization. Ethylenediaminetetraacetic acid (EDTA), Sodium hydroxide (NaOH), polyoxyethyleneglycol-sorbitan monolaurate (Tween-20TM), bovine serum albumin (BSA), L-cysteine, streptavidin HRP conjugated (Str-HRP), 3-3'-5-5' tetramethylbenzidine (TMB substrate for ELISA), saline sodium citrate (SSC, 20X) were purchased from Sigma-Aldrich/Merck (Milan, Italy).

The synthetic DNA-sequences were purchased from IDT (Integrated DNA Technologies, Iowa USA), three different sequences were used:

Probe: 5'-ThioMC6-AGC CCA ACT TTC TCC GGT CC-3'

Probe_(Label): 5'-ThioMC6-TTT CTC CGG TCC CAT CTT TC-BiotinTEG-3'

Target_(Label): 5'-BiotinTEG-GGA CCG GAG AAA GTT GGG CT-3'